Measurement of Parity-Violating Asymmetry in Electron-Deuteron Inelastic Scattering - v0.3, to be submitted to Phys. Rev. C

Abstract

The parity-violating asymmetries between a longitudinally-polarized electron beam and a unpolarized deuterium target have been measured recently. The measurement covered two points in the deep inelastic scattering region and five kinematic points in the nucleon resonance region. We provide here details of the experimental setup, the data analysis, results on all asymmetry measurement including parity-violating electron asymmetries and those of inclusive pion production and beam-normal asymmetries. The deep inelastic asymmetries were used to extract the electron-quark weak effective couplings, and the resonance asymmetries provided the first evidence for quark-hadron duality in electroweak observables. These electron asymmetries and their interpretation were published earlier, but are presented here in more detail.

Keywords:
PACS: 13.60.Hb, 24.85.+p, 25.30.-c

Contents

1. Physics Motivation

Parity symmetry implies that the physics laws behind a system remain the same when the system undergoes a space-reversal (parity) transformation. A simplified version of such transformation, in which only one dimension is reversed, mimics a mirror reflection, and thus parity symmetry is often called mirror symmetry. Among all known interactions of nature, electromagnetic, strong, and gravitational forces respect parity symmetry, but the weak force does not, as first postulated by Lee and Yang [1], and verified experimentally in nuclear β-decay by Wu [2], in 1957. The fact that elementary particles violate parity symmetry implies that the charges that determine their weak-interaction strength are different from, for example, the electric charge for the electromagnetic interaction, the color charge for the strong nuclear force, and the mass for gravity.

The standard scheme to describe how particles violate parity symmetry is to use their chirality, approximated by the experimentally-accessible helicity in the ultra-relativisitic limit. A particle is defined to be in the right(left)-handed helicity state, when it is spinning in the same (opposite) direction as its linear momentum. Since a parity transformation changes a right-handed particle to left-handed, and vice versa, parity violation implies that the weak charge must depend on the particle's chiral state.

In the decade that followed the first observation of parity violation, many theories were proposed to explain this phenomenon. Among them is the Glashow-Weinberg-Salam (GWS) theory [3, 4, 5] of electroweak unification. In this theory, the charged-weak force behind β-decays only act on left-handed spin-1/2 elementary particles (elementary fermions) and right-handed anti-fermions, thus violate parity to the maximal degree. The theory also predicted the existence of a new, neutral weak force carried by an electrically-neutral boson, the Z^0. Unlike the $W^{\pm}$ bosons that carry the charged-weak force, the Z^0 does interact with both chiral states of all fermions and anti-fermiions. For neutral weak interactions, the difference in the fermion's weak-interaction strengths between its left- and right-handed chiral states is described by the weak axial charge g_A, while the average of the two is called the weak vector charge g_V. In the GWS theory, g_A equals the particle's weak isospin T_3: $g_A = T_3 = 1/2$ for up, charm and top quarks and $-1/2$ for down, strange and bottom quarks and electrons; and g_V is related to the particle's T_3 and electric charge Q: $g_V = T_3 - 2Q\sin^2\theta_W$, with θ_W the weak mixing angle, a parameter that describes how the electromagnetic interaction is unified with the weak force. Antiparticles have opposite weak isospin and electric charge, and thus opposite g_A and g_V as their particle counterparts. The fact that $g_A = \pm 1/2$ for elementary fermions implies that they all have a chirality preference in neutral weak interactions.

The Z^0 was soon observed in the 1970's in both neutrino [6, 7] and electron scattering experiments [8, 9]. In electron scattering, parity violation is observed by a difference (an asymmetry) in the scattering cross sections between left- and right-handed electrons from an unpolarized target:

$$A_{PV} \equiv \frac{\sigma_R - \sigma_L}{\sigma_R + \sigma_L} . \quad (1)$$

In the most recent decade, parity-violating electron scattering (PVES) has been used primarily in the elastic scattering region. In elastic kinematic settings, the target nucleus remains as a whole and the internal bonds that bind quarks together to form the nucleon (or bind nucleons together to form the nucleus) are not disturbed. Elastic PVES asymmetry has been used to study the internal structure of the target that cannot be revealed through electromagnetic interactions. For example, elastic scattering from the proton and light nuclei has been used to study whether sea quarks contribute to the nucleon's structure, that is, whether the strange and the anti-strange quarks are distributed differently after their creation. Such nucleon stange form factor experiments have been carried out at many different facilities worldwide, such as the SAMPLE experiment [10, 11, 12, 13, 14] at MIT Bates, the A4 experiment at MAMI/Mainz [15, 16, 17], the HAPPEX experiments [18, 19, 20, 21, 22, 23] in JLab Hall A, and the $G0$ experiment [24, 25, 26] in JLab Hall C. In the recent PREX experiment [27, 28], elastic scattering from ^{208}Pb has confirmed a difference in the spatial distributions between protons and neutrons inside this heavy nucleus.

However, of particular value to testing the Standard Model is the so-called deep inelastic scattering (DIS), where electrons scatter directly from quasi-free quarks and the parity-violating deep inelastic scattering (PVDIS) asymmetry is determined by the effective electron-quark couplings C_{1q} and C_{2q}, weighted by kinematic factors and the well-determined DIS structure functions. In the Standard Model tree level, the C_{1q}, C_{2q} couplings are the product of the electron and quark weak charges: $C_{1q} = 2g_A^e g_V^q$ (the effective electron-quark AV coupling), and $C_{2q} = 2g_V^e g_A^q$ (the effective electron-quark VA coupling).

The first PVES experiment [8, 9], E122 at the Stanford Linear Accelerator Center, was performed in the DIS region and provided the first measurement of the weak mixing angle $\sin^2\theta_W$. The E122 results were in good agreement with predictions from the GWS-theory, establishing it as a cornerstone of the now Standard Model of particle physics. The thirty years that followed witnessed a vast amount of Standard-Model-test experiments. Among those that determine the weak charges of elementary particles, the most precise measurement of the electron weak charges came from PVES on an electron target [29, 30] that provided $C_{2e} = 2g_V^e g_A^e$. The best result on the effective electron-quark AV couplings C_{1q} is from a combination [31] of elastic PVES [18, 19, 20, 21, 22, 23, 24, 25, 26] and atomic parity violation experiments [32, 33, 34, 35].

On the other hand, determination of the C_{2q} couplings from PVES is difficult: For elastic scattering, the asymmetry component sensitive to the quark chirality (spin) is not directly determined by the C_{2q}, but by the nucleon's axial form factor G_A. Extracting C_{2q} from G_A [11, 12, 13, 14], depends on hadronic models and is subject to large uncertainties in the radiative corrections. For DIS, similar to the fact that the quark-spin-dependent contribution to the unpolarized cross section is suppressed at forward angles, the quark-chirality-dependent C_{2q} contribution to PVDIS asymmetry is kinematically suppressed because of angular momentum conservation. The small value of g_V^e further reduces the C_{2q} contribution to the PVDIS asymmetry. Until the experiment reported here was carried out, the only direct data on C_{2q} were from SLAC E122.

In addition to DIS and elastic scattering, another kinematic region accessible in electron scattering is the nucleon resonance region. In this region, bonds between quarks inside the nucleon are excited, but are not fully un-seen (as in DIS). The nucleon resonance region therefore provides a transition between the quark and gluon degrees of freedom of DIS to hadron degree of freedom of elastic scattering. Inclusive measurements in the nucleon resonance region have demonstrated a remarkable feature called "quark-hadron duality", first pointed out by Bloom and Gilman [36], in which the low-energy (few GeV) cross sections averaged over the energy intervals of the resonance structures resemble the asymptotically high energies of DIS. Over the past decade, duality has been verified in the unpolarized structure functions F_2 and F_L at four-momentum-transfer-squared Q^2 values below 1 (GeV/c)^2 [37, 38, 39, 40, 41], in the proton spin asymmetry A_1^p down to $Q^2 = 1.6$ (GeV/c)^2 [42], in the spin structure function g_1 down to $Q^2 = 1.7$-1.8 (GeV/c)^2 [43, 44], in the helicity-dependent structure functions $H_{1/2,3/2}$ [45], and for charged pion electroproduction in semi-inclusive scattering [46]. It was speculated that duality is a universal feature of the quark-hadron transition that should be exhibited not only in electromagnetic interactions, but also in charged lepton scattering via the weak interactions [47], and perhaps other processes as well.

We report here details on a PVDIS experiment that was carried out at the Thomas Jefferson National Accelerator Facility (Jefferson Lab, or JLab) in 2009. During this experiment, PVES asymmetries on a deuterium target were measured at two DIS kinematics and five nucleon resonance settings. The precision of the DIS measurement was higher than E122, and the kinematics were optimized for the extraction of the C_{2q} couplings. The DIS asymmetry and the C_{2q} couplings were published in Ref. [48], which improved over previous data by a factor of five. Data taken at resonance settings had larger uncertainties, but nevertheless provided the first PVES data covering the whole nucleon resonance region. The resonance asymmetry results were published in Ref. [49] which provided the first observation on quark-hadron duality on parity-violating observables. In this archival paper we first review the formalism for PVDIS,

the SLAC E122 experiment, then report the new JLab experiment E08-011 including its apparatus, data analysis, and all systematic uncertainties. In addition to PVES asymmetries, we report asymmetry results on inclusive pion production, pair-production, and beam-normal asymmetries. We provide interpretation of the electron asymmetries in DIS and the nucleon resonance regions in the end.

1.1. Formalism for Parity-Violation in Electron Inelastic Scattering

For inelastic electron scattering off a nucleon or nuclear target, the parity-violating asymmetry between right- and left-handed electrons originates from interference between photon- and Z^0-exchange between the electron and the target (Fig. 1). This asymmetry can be written as [50]

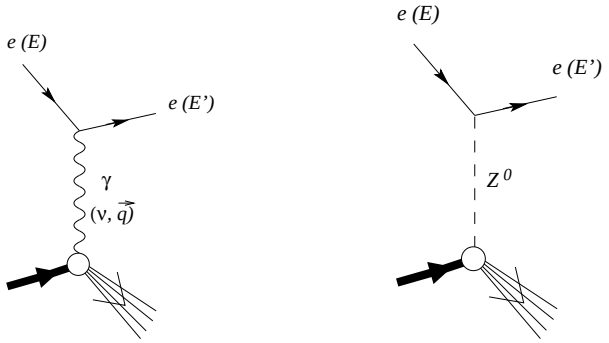

Figure 1: One-photon-(left) and Z^0-exchange (right) between the electron and the target. The interference between these two processes leads to a parity-violating asymmetry between left- and right-handed electrons.

$$A_{PV} = -\frac{G_F Q^2}{4\sqrt{2}\pi\alpha}\left[a_1(x)Y_1(y) + a_3(x)Y_3(y)\right] , \tag{2}$$

where G_F is the Fermi constant, α is the fine structure constant, and $Q^2 \equiv -q^2$ is the negative of the four-momentum transferred from the electron to the target q, squared. For scatterings from a fixed target, when the recoil to the target nucleus can be neglected,

$$Q^2 = 2EE'(1-\cos\theta) , \tag{3}$$

where θ is the electron scattering angle, E and E' the incident and the scattered electron's energy, respectively. Another important variable is the invariant mass of the γ-nucleon (or Z^0-nucleon) system:

$$W^2 = M^2 + 2M\nu - Q^2. \tag{4}$$

Typically, the region $M < W < 2$ GeV is the nucleon resonance region and $W > 2$ GeV corresponds to the DIS region.

The kinematic factors $Y_{1,3}$ are defined as

$$Y_1 = \left[\frac{1+R^{\gamma Z}}{1+R^{\gamma}}\right]\frac{1+(1-y)^2-y^2\left[1-\frac{r^2}{1+R^{\gamma Z}}\right]-xy\frac{M}{E}}{1+(1-y)^2-y^2\left[1-\frac{r^2}{1+R^{\gamma}}\right]-xy\frac{M}{E}} \tag{5}$$

and

$$Y_3 = \left[\frac{r^2}{1+R^{\gamma}}\right]\frac{1-(1-y)^2}{1+(1-y)^2-y^2\left[1-\frac{r^2}{1+R^{\gamma}}\right]-xy\frac{M}{E}} . \tag{6}$$

Here x is the Bjorken scaling variable

$$x \equiv Q^2/(2M\nu) \tag{7}$$

with M the proton mass and $\nu = E - E'$ the energy transfer from the electron to the target; $y = \nu/E = (E - E')/E$ is the fractional energy loss of the electron, $r^2 = 1 + \frac{Q^2}{\nu^2}$, and $R^{\gamma(\gamma Z)}$ is the ratio of the longitudinal to transverse virtual photon electromagnetic absorption cross sections ($\gamma - Z^0$ interference cross sections).

To a good approximation $R^{\gamma Z}$ can be assumed to be equal to R^{γ}, resulting in $Y_1(y) = 1$. The $a_{1,3}$ terms are

$$a_1(x) = 2g_A^e \frac{F_1^{\gamma Z}}{F_1^{\gamma}} , \tag{8}$$

$$a_3(x) = g_V^e \frac{F_3^{\gamma Z}}{F_1^{\gamma}} , \tag{9}$$

where the structure functions, $F_{1,3}^{\gamma,\gamma Z}$, can be interpreted in the quark-parton model (QPM) to be related to the parton distribution functions (PDF) $q_i(x)$ and $\bar{q}_i(x)$ of the target:

$$F_1^{\gamma}(x) = \frac{1}{2} \sum Q_i^2 \left[q_i(x) + \bar{q}_i(x) \right] , \tag{10}$$

$$F_1^{\gamma Z}(x) = \sum Q_i g_V^i \left[q(x) + \bar{q}_i(x) \right] , \tag{11}$$

$$F_3^{\gamma Z}(x) = 2 \sum Q_i g_A^i \left[q_i(x) - \bar{q}_i(x) \right] . \tag{12}$$

$$\tag{13}$$

Here, Q_i denotes the quark's electric charge and the summation is over the quark flavors $i = u, d, s \cdots$. Equations (9,12) show that the $a_3(x)$ term involves the chirality of the quark (g_A^i) and therefore is suppressed by the kinematic factor Y_3 due to angular momentum conservation. It vanishes at the forward angle $\theta = 0$ or $y = 0$, and increases with θ or y at fixed x.

In most world parameterizations, it is common to fit the structure functions F_2 and R simultaneously to cross-section data. They are related through

$$F_2^{\gamma(\gamma Z)} = \frac{2x F_1^{\gamma(\gamma Z)}(1 + R^{\gamma(\gamma Z)})}{r^2} , \tag{14}$$

or equivalently:

$$F_1^{\gamma(\gamma Z)} = \frac{r^2 F_2^{\gamma(\gamma Z)}}{2x(1 + R^{\gamma(\gamma Z)})} . \tag{15}$$

In the QPM the ratios $R^{\gamma(\gamma Z)}$ are assumed to be zero (and $r = 1$). Hence one can construct the $F_{1,2}$ structure functions from PDFs as

$$F_2^{\gamma}(x) = 2x F_1^{\gamma}(x) = x \sum Q_i^2 \left[q_i(x) + \bar{q}_i(x) \right] , \tag{16}$$

$$F_2^{\gamma Z}(x) = 2x F_1^{\gamma Z}(x) = 2x \sum Q_i g_V^i \left[q_i(x) + \bar{q}_i(x) \right] . \tag{17}$$

For electron scattering, one defines the product of the electron and the quark weak couplings as the effective weak coupling constants $C_{1q,2q}$. In leading order of one-photon and one-Z^0 exchanges between the electron and the target (Fig. 1),

$$C_{1u} = 2g_A^e g_V^u , \qquad C_{2u} = 2g_V^e g_A^u , \tag{18}$$

$$C_{1d} = 2g_A^e g_V^d, \qquad C_{2d} = 2g_V^e g_A^d. \tag{19}$$

Using the appropriate electric charge and the weak isospin of quarks, they are related to the weak mixing angle θ_w as

$$C_{1u} = 2g_A^e g_V^u = 2(-\frac{1}{2})(\frac{1}{2} - \frac{4}{3}\sin^2\theta_W) = -\frac{1}{2} + \frac{4}{3}\sin^2\theta_W , \tag{20}$$

$$C_{2u} = 2g_V^e g_A^u = 2(-\frac{1}{2} + 2\sin^2\theta_W)(\frac{1}{2}) = -\frac{1}{2} + 2\sin^2\theta_W , \tag{21}$$

$$C_{1d} = 2g_A^e g_V^d = 2(-\frac{1}{2})(-\frac{1}{2} + \frac{2}{3}\sin^2\theta_W) = \frac{1}{2} - \frac{2}{3}\sin^2\theta_W , \tag{22}$$

$$C_{2d} = 2g_V^e g_A^d = 2(-\frac{1}{2} + 2\sin^2\theta_W)(-\frac{1}{2}) = \frac{1}{2} - 2\sin^2\theta_W . \tag{23}$$

$$\tag{24}$$

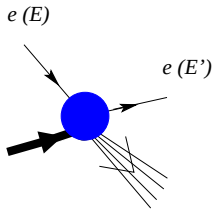

Figure 2: Feynman diagram for contact interactions, used commonly to describe beyond-Standard-Model interactions.

In Standard-Model-test experiments, new physics that can be accessed by PVES asymmetries typically cannot be described by the one-boson exchange of Fig. 1 and Eq. (18-19) are no longer valid. In this case, one writes [89]

$$C_{1u} = g_{AV}^{eu} \ , \qquad C_{2u} = g_{VA}^{eu} \ , \tag{25}$$

$$C_{1d} = g_{AV}^{ed}, \qquad C_{2d} = g_{VA}^{ed}, \tag{26}$$

and the corresponding Feynman diagrams change from Fig. 1 to Fig. 2. The C_{1q}, C_{2q} couplings therefore provide information on new contact interactions beyond the Standard Model. Note that even though $C_{1,2}$ cannot be factorized into an electron and a target vertex, their chiral property remains the same.

The formalism of inelastic PV asymmetries, Eq. (2), can be simplified as follows: Defining $q_i^{\pm}(x) \equiv q_i(x) \pm \bar{q}_i(x)$, one has in the QPM

$$a_1(x) \ = \ 2\frac{\sum C_{1i} Q_i q_i^+(x)}{\sum Q_i^2 q_i^+(x)} \ , \tag{27}$$

$$a_3(x) \ = \ 2\frac{\sum C_{2i} Q_i q_i^-(x)}{\sum Q_i^2 q_i^+(x)} \ . \tag{28}$$

For an isoscalar target such as the deuteron, neglecting effects from heavier quark flavors and assuming the isospin symmetry that $u^p = d^n$, $d^p = u^n$ [$u, d^{p(n)}$ are the up and down quark PDF in the proton (neutron)], $s = \bar{s}$, and $c = \bar{c}$, the functions $a_{1,3}(x)$ simplify to

$$a_1(x) \ = \ \frac{6\left[2C_{1u}(1+R_C) - C_{1d}(1+R_S)\right]}{5 + R_S + 4R_C} \ , \tag{29}$$

$$a_3(x) \ = \ \frac{6\left(2C_{2u} - C_{2d}\right) R_V}{5 + R_S + 4R_C} \ , \tag{30}$$

where

$$R_C \equiv \frac{2(c+\bar{c})}{u+\bar{u}+d+\bar{d}}, \ \ R_S \equiv \frac{2(s+\bar{s})}{u+\bar{u}+d+\bar{d}}, \ \text{ and } \ R_V \equiv \frac{u-\bar{u}+d-\bar{d}}{u+\bar{u}+d+\bar{d}} \ . \tag{31}$$

The asymmetry then becomes

$$A_{PV} \ = \ \left(\frac{3G_F Q^2}{2\sqrt{2}\pi\alpha}\right) \frac{2C_{1u}[1+R_C(x)] - C_{1d}[1+R_S(x)] + Y_3(2C_{2u} - C_{2d})R_V(x)}{5 + R_S(x) + 4R_C(x)} \ . \tag{32}$$

The factor $Y_3 R_V$ is therefore crucial in accessing the C_{2q}.

If one neglects sea quarks completely, $R_C = R_S = 0$, $R_V = 1$, no PDF is involved (i.e. neglecting nucleon structure) and

$$a_1(x) = \frac{6}{5}\left(2C_{1u} - C_{1d}\right) \ , \qquad a_3(x) = \frac{6}{5}\left(2C_{2u} - C_{2d}\right) \ , \tag{33}$$

which lead to [51]

$$A_{PV} \ = \ \left(\frac{3G_F Q^2}{10\sqrt{2}\pi\alpha}\right) \left[(2C_{1u} - C_{1d}) + Y_3(2C_{2u} - C_{2d})\right] \ . \tag{34}$$

This expression can be used to estimate how the uncertainty in the PDFs affects the interpretation of the asymmetry measurement.

1.2. Previous Data on Electron-Quark VA Coupling

The SLAC E122 experiment [8, 9] was the only PVDIS measurement before the present experiment. During the E122 experiment, a longitudinally polarized electron beam was scattered from 30-cm long unpolarized proton and deuteron targets at Q^2 values ranging from 1.05 to 1.91 (GeV/c)^2. Four beam energies: 16.2, 17.8, 19.4 and 22.2 GeV were used. Scattered electrons were collected in a magnetic spectrometer at 4° by integrating signals from a gas Cherenkov detector. Data from the two highest beam energies were published as [8] $A/Q^2 = (-9.5 \pm 1.6) \times 10^{-5}$ (GeV/c)$^{-2}$. The average y value was 0.21 and the average Q^2 was 1.6 (GeV/c)^2. The y-dependence of the asymmetry was used to determine the value of $\sin^2\theta_W$.

Asymmetry results for 11 individual kinematic settings were published in Ref. [9]. To study the sensitivity of the E122 results to C_{2q} couplings, we show these kinematics in Table 1 including the values for Y_3 and R_V. Calculations of R_V were based on the MSTW2008 parameterization [52] of the parton distribution functions. Equation (32) illustrates that the product $Y_3 R_V$ provides the lever arm to isolate the C_{2q} contribution to the asymmetry. The relatively small values and coverage of $Y_3 R_V$ in E122 were largely due to the small and fixed scattering angle (4°). Hence, the kinematics used were not ideal for isolating the C_{2q} term.

E_b (GeV)	Q^2 (GeV/c)^2	x	y	Y_3	R_S	R_V	$Y_3 R_V$
16.2	0.92	0.14	0.22	0.19	0.071 ± 0.014	0.623 ± 0.014	0.12
19.4	1.53	0.28	0.15	0.15	0.022 ± 0.005	0.859 ± 0.012	0.13
19.4	1.52	0.26	0.16	0.16	0.027 ± 0.006	0.836 ± 0.012	0.13
19.4	1.33	0.16	0.23	0.21	0.068 ± 0.012	0.671 ± 0.014	0.14
19.4	1.28	0.14	0.25	0.23	0.082 ± 0.013	0.630 ± 0.014	0.14
19.4	1.25	0.13	0.26	0.24	0.090 ± 0.013	0.608 ± 0.013	0.14
19.4	1.16	0.11	0.29	0.26	0.107 ± 0.013	0.563 ± 0.013	0.15
19.4	1.07	0.09	0.32	0.29	0.127 ± 0.014	0.518 ± 0.012	0.15
19.4	0.93	0.07	0.36	0.33	0.148 ± 0.017	0.471 ± 0.011	0.15
22.2	1.96	0.28	0.17	0.17	0.027 ± 0.005	0.860 ± 0.011	0.14
22.2	1.66	0.15	0.26	0.24	0.081 ± 0.012	0.654 ± 0.014	0.16

Table 1: Kinematics for the SLAC E122 experiment. Values for R_S and R_V are calculated using the MSTW2008 [52] leading-order parameterization. The product $Y_3 R_V$ provides the lever arm for isolating the C_{2q} contribution to the asymmetry.

Figure 3 shows previous data on $2C_{2u} - C_{2d}$ vs. $2C_{1u} - C_{1d}$. The vertical band shows the most recent fit [31] to C_{1q} data from all elastic PVES and Cs atomic parity violation [32, 33, 34, 35] experiments. The yellow ellipse represents the constraint from the E122 asymmetries (using the kinematical sensitivity listed in Table 1). One can see that the constraint on the $2C_{2u} - C_{2d}$ is nearly two orders of magnitude larger than $2C_{1u} - C_{1d}$.

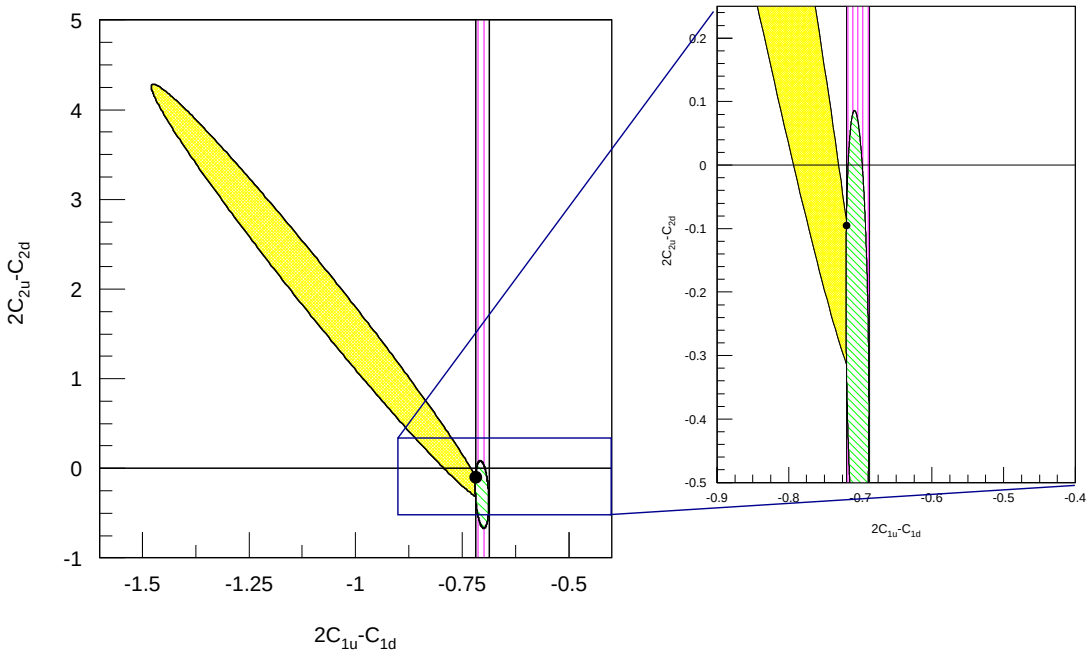

Figure 3: Previous data on C_{2q}. The yellow ellipse represents a simutaneous fit to C_{1q} and C_{2q} using only the SLAC E122 asymmetries [9]. The magenta vertical band represents the best C_{1q} data [31], and the green ellipse the combined fit of the E122 asymmetries and the best C_{1q}. The right panel shows an enlarged view with the vertical and the horizontal axis at the same scale.

2. Apparatus

The experiment was performed in experimental Hall A at the Thomas Jefferson National Accelerator Facility (TJNAF, or JLab). The floor plan for Hall A is shown schematically in Fig. 4. A 105 μA longitudinally polarized electron beam was incident on a 20-cm long liquid deuterium target, and scattered electrons were detected by the two High Resolution Spectrometers (HRS) [53] in inclusive mode. A series of beam diagnostic devices was used to measure the beam energy, position, and the current. A Luminosity Monitor was located downstream from the target to monitor target density fluctuation and possible false asymmetries. For DIS measurements the beam energy used was 6 GeV, the highest achievable with the countinuous electron beam accelerator facility (CEBAF) of JLab before its 12 GeV Upgrade.

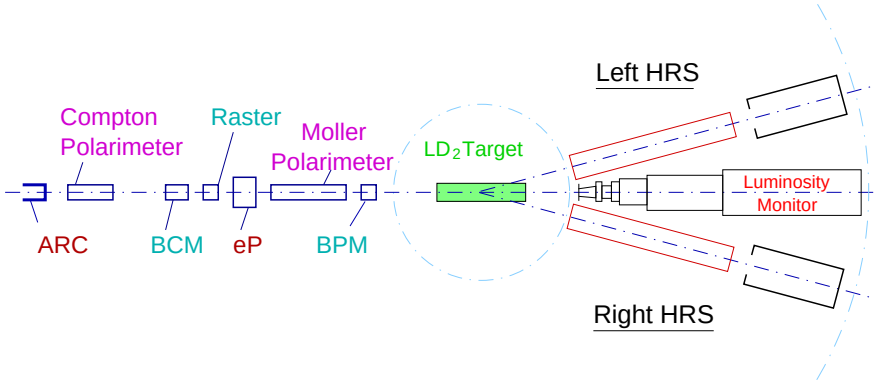

Figure 4: Schematic floor plan of the 6 GeV PVDIS experiment in Hall A at JLab. The electron beam enters from the left and scattered from a liquid D_2 target in the middle of the hall. The scattered electrons were detected in the HRS pair in inclusive mode.

The experimental techniques for measuring small asymmetries of order 1 part per million (ppm) or less have been successfully deployed in the HAPPEx experiments [18, 19, 20, 21, 22, 23] and the PREx [27] experiment in JLab Hall A. These two experiments had maintained systematic uncertainties associated with beam helicity reversal at the 10^{-8} level. The asymmetries sought for in this experiment were of order 10^2 ppm with required statistical accuracies at the $(3-4)\%$ level, which were two orders-of-magnitude larger than the systematic uncertainty established in the recent PVES experiments. The main challenge of the experiment was a reliable rejection of the large pion electro- and photo-production (that is only present in inelastic scattering) background while identifying electrons at high rates. While the standard HRS detector package and data acquisition (DAQ) system routinely provide high particle identification (PID) performance, they are based on full recording of the detector signals and are limited to event rates of 4 kHz. This is not sufficient for the few-hundred kHz rates expected for the present experiment. A new DAQ electronic system was built to count event rates up to 600 kHz with hardware-based particle identification, see Ref. [54] for a complete report on the DAQ design, its PID performance, deadtime effects, and the quality of the asymmetry measurement. The standard DAQ of the HRS will be referred to as the HRS DAQ hereafter.

The apparatus and its effect on the measured asymmetry are presented in this section. The polarized electron beam will be described first (section 2.1), followed by descriptions of the beam monitors (section 2.2), the beam polarimetry (section 2.3), the target system (section 2.4), and the spectrometers and detectors (section 2.5).

2.1. Polarized Electron Beam

The electron beam was produced from a strained superlattice GaAs/GaAsP photocathode illuminated by circularly polarized laser light [55]. The laser polarization is controled by a Pockels cell. By reversing the high voltage on the Pockels cell, the sign of the laser circular polarization flips and the direction of the electron spin at the target is reversed every 33 ms [56]. These 33-ms periods are called "beam helicity windows" or simply "windows". Data collected in the first 0.5 ms of each window is rejected to allow the Pockels cell to settle. During this experiment, the helicity of the electron beam was controlled by a helicity signal, and followed a quartet structure of either "RLLR" or "LRRL", with each state lasting 33 ms and the first state of each quartet selected from a pseudorandom sequence [19, 20, 21, 22]. The helicity signal was sent to the data acquisition system after being delayed by eight helicity states (two quartets). This delayed helicity sequence controlled the data collection. The helicity signal was line-locked to the 60 Hz line, thus ensuring a good cancellation of the power-line noise.

To reduce possible systematic errors, a half-wave plate (HWP) was inserted intermittently into the path of the polarized laser, which resulted in a reversal of the actual beam helicity while keeping the helicity signal sequence unchanged. Roughly equal statistics were accumulated with opposite HWP states for the measured asymmetry, which suppressed many systematic effects. The expected sign flips in the measured asymmetries between the two beam HWP configurations were observed.

The direction of the beam polarization could also be controlled by a Wien filter and solenoidal lenses near the injector [57]. After accelerating, the beam was directed into Hall A, where its intensity, energy and trajectory on target were inferred from the response of several monitoring devices. The beam monitors and the scattered electron trigger signals from the DAQ were integrated over the helicity window and digitized, from which raw cross-sectional asymmetries $A^{\rm raw}$ were formed, see section 3.1. To keep spurious beam-induced asymmetries under control at well below the ppm level, careful attention was given to the design and configuration of the laser optics leading to the photocathode. A specialized DAQ system (called the HAPPEx DAQ) [18, 19, 20, 21, 22, 23] was used to provide feedback at the photocathode to minimize these beam asymmetries [56]. Measurement of the polarization of the beam will be described in section 2.3 and the polarization results in section 3.4.

2.2. Beam Monitoring and Rastering

As a direct input to the asymmetry extraction, the beam intensity was measured by two microwave cavity Beam Current Monitors (BCMs) and an Unser monitor located 25 m upstream of the target [53]. In addition, helicity-correlations in the beam properties such as energy and position could add systematic uncertainties and widen the uncertainty of $A^{\rm raw}$, thus are a primary concern for parity-violation experiments. At JLab, the beam position is measured by "stripline" monitors [58], each of which consists of a set of four thin wires placed symmetrically around the beam pipe. The wires act as antennae that provide a signal, modulated by the microwave structure of the electron beam, that is proportional to the beam position as well as intensity. Two such Beam Position Monitors (BPMs) are available in Hall A, located 7.524 m (BPMA) and 1.286 m (BPMB) upstream of the target center. Beam positions measured at BPMA and BPMB were extrapolated to provide the position and the incident angle at the target. An additional BPM

(BPM12x) is available in the arc section of the beamline just before it enters the hall to monitor changes in the beam energy.

The electron beam at JLab has a nominal spot size of 100-200 μm (root-mean-square or rms value). To avoid overheating the target, the beam is routinely defocussed at 20 kHz by a rastering system consists of two sets of steering magnets located 23 m upstream of the target. This fast rastering system can deliver beam with a uniform elliptical or rectangular distribution of size between 100 μm and several mm at the target. A square distribution of approximately 4×4 mm^2 was used for this experiment. The exact correspondence between BPM signals and the actual beam position at the target varies with beam energy and must be calibrated. In addition, the BPM information is not fast enough to provide the event-by-event information and the raster currents must be used to calculate real-time beam position on the target. Establishing the relation between BPM signals and beam positions, and between raster currents and the beam positions, is part of the BPM calibration described in section 3.5.1.

2.3. Beam Polarimetry

Three beam polarimetry techniques were available at JLab: a Mott polarimeter in the injector of the Linac, and a Møller and a Compton polarimeter in Hall A. The Mott and the Møller measurements must be done separately from production data taking, while Compton measurements are non-intrusive. The Mott polarimeter [59, 60, 61, 62] is located near the injector to the first linac where the electrons have reached 5 MeV in energy. During the beam normal asymmetry A_n measurement, it was used for setting up the transversely-polarized beam and verifying that the beam polarization was fully in the vertical direction. In the following we will describe the principle of only Møller and Compton polarimeters. For production runs, since the Mott polarimeter measures only the polarization at the injector and it can differ from the beam polarization in the experimental hall, its results were not used directly in our analysis.

2.3.1. Møller Polarimeter

A Møller polarimeter [53] measures the beam polarization via a measurement of the asymmetry in $\vec{e} - \vec{e}$ (Møller) scattering, which depends on the beam and target polarizations $P^{\rm beam}$ and $P^{\rm targ}_{\rm Møller}$, as well as on the Møller scattering analyzing power $A^{\rm th}_m$:

$$A_M = \sum_{i=X,Y,Z} (A^{\rm th}_{Mi} \cdot P^{\rm targ}_{i,\rm Møller} \cdot P^{\rm beam}_i) \, . \tag{35}$$

Here, $i = X, Y, Z$ defines the projections of the polarizations with Z parallel to the beam and OXZ the Møller scattering plane. The analyzing powers $A^{\rm th}_{Mi}$ depend on the scattering angle in the $\vec{e} - \vec{e}$ center-of-mass (CM) frame, $\theta_{\rm CM}$, and are calculable in QED. The longitudinal analyzing power is

$$A^{\rm th}_{MZ} = -\frac{\sin^2\theta_{\rm CM}(7 + \cos^2\theta_{\rm CM})}{(3 + \cos^2\theta_{\rm CM})^2}. \tag{36}$$

The absolute value of $A^{\rm th}_{MZ}$ reach a maximum of 7/9 at $\theta_{\rm CM} = 90^\circ$. At this angle the transverse analyzing powers are $A^{\rm th}_{MX} = -A^{\rm th}_{MY} = A^{\rm th}_{MZ}/7$.

The Møller polarimeter target was a ferromagnetic foil magnetized in a magnetic field of 24 mT along its plane. The target foil can be oriented at various angles in the horizontal plane, providing both longitudinal and transverse polarization measurements. The asymmetry was measured at two target angles ($\pm 20^\circ$) and the average taken, which cancels contributions from transverse components of the beam spin and thus reduces the uncertainties from target angle measurements. At a given target angle, two sets of measurements with oppositely signed target polarizations were made which cancels some systematic effects such as that from beam current asymmetries. The Møller target polarization was approximately 8%.

The Møller-scattered electrons were detected in a magnetic spectrometer consisting of three quadrupoles and a dipole [53]. The spectrometer selects electrons in a range of $75^\circ \leqslant \theta_{\rm CM} \leqslant 105^\circ$ and $-5^\circ \leqslant \phi_{\rm CM} \leqslant 5^\circ$ where $\phi_{\rm CM}$ is the azimuthal angle in the CM frame. The detector consisted of lead-glass calorimeter modules in two arms to detect the electrons in coincidence. The Møller measurements must be performed separately from production runs, and each measurement takes approximately 4 hours including setting up the magnets to direct the electron beam to the Møller target. The statistical uncertainty of the Møller measurements is negligible, compared to the approximately 2% systematic error which is dominated by the uncertainty in the foil polarization.

2.3.2. Compton Polarimeter

The Compton polarimeter [63, 64, 65] is based on scattering of the polarized electron beam from a polarized laser beam in a beam chicane. For this experiment, the beam polarization was extracted from the backscattered photon signals detected in a GsO crystal in the integrated mode [65]. Scattered electrons can be detected either in the inclusive mode or in coincidence with the backscattered photons, but electron detection was not used in this experiment.

The Compton asymmetry $A_C = (n_C^R - n_C^L)/(n_C^R + n_C^L)$ was measured, where $n_C^R, (n_C^L)$ refers to the scattered photon counting rate for right (left) electron helicity normalized to the beam intensity. This asymmetry is related to the electron beam polarization via

$$P_e = \frac{A_C}{P_\gamma A_C^{\rm th}} \, , \tag{37}$$

where P_γ is the photon polarization and $A_C^{\rm th}$ the Compton analyzing power. At typical JLab energies (a few GeV), the Compton cross-section asymmetry is only a few percent. To compensate for the small asymmetry, a Fabry-Perot cavity [66] was used to amplify the photon density from a standard low-power laser such that high statistics can be obtained within one to a few hours. An average power of 1200 W was accumulated inside the cavity with a photon beam waist of the order of 150 μm and a photon polarization above 99%, monitored online at the exit of the cavity [67]. When extracting the beam polarization from Compton data, a GEANT4-based simulation was performed to reproduce the measured photon energy distribution and to extract the analyzing power. For the present experiment the systematic uncertainty of Compton measurement was approximately 1.92% relative and was dominated by the understanding of the analyzing power (1.75% relative) and the laser polarization (0.8% relative).

2.4. Target System

The Hall A cryogenic target system [53] was used for this experiment. We used a 20-cm long deuterium target cell for the main production data-taking. Solid targets were used for evaluating backgrounds, studying the spectrometer optics, and checking beam centering. The target cell and a solid target ladder sit in an evacuated cylindrical scattering chamber of 104 cm diameter, centered on the pivot for the spectrometers. Also located inside the scattering chamber were subsystems for cooling, temperature and pressure monitoring, target motion, gas-handling and controls. The scattering chamber was maintained under a 10^{-6} Torr vacuum. The exit windows on the scattering chamber allowed scattered particles to reach the spectrometers. These windows were made of 0.406-mm thick Al foil.

Figure 5 shows a schematic diagram of the target ladder arrangement used during this experiment. Of the three cryogenic loops, only loop 1 was used. The liquid deuterium loop was operated at a temperature of 22 K and a pressure

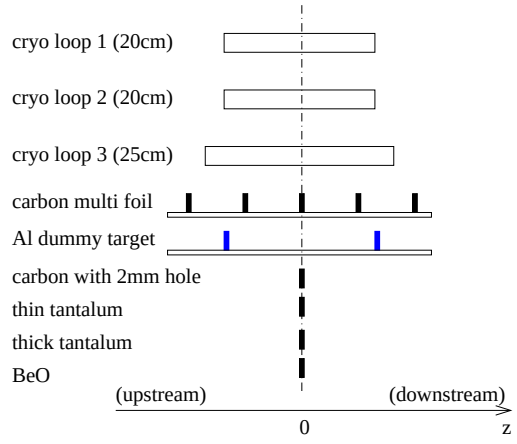

Figure 5: Schematic diagram of the target ladder arrangement used during the experiment. The electron beam is along the horizontal direction (the z-axis) and is incident from the left on the target. The carbon multi foils were located at $z = (-15, -7.5, 0, 7.5, 15)$ cm and the Al dummy foils were located at $z = (-10, 10)$ cm. All other solid targets were located at $z = 0$ cm and were about 1 inch apart in the vertical direction.

of 25 psia, leading to a density of about 0.1676 g/cm^3. The diameter of the cell was 2.0 cm. The thickness of its walls and the solid targets are summarized in Table 2.

Target	Position along z	Purity	Thickness
cryo-loop 1[a]	Entrance window,-10 cm		$0.126 \pm 0.011 \pm 0.003$ mm[c]
	Exit window, +10 cm		$0.100 \pm 0.008 \pm 0.003$ mm
	Wall, beam left upstream		$0.313 \pm 0.008 \pm 0.003$ mm
	Wall, beam left middle		$0.317 \pm 0.002 \pm 0.003$ mm
	Wall, beam left downstream		$0.323 \pm 0.003 \pm 0.003$ mm
	Wall, beam right upstream		$0.340 \pm 0.002 \pm 0.003$ mm
	Wall, beam right middle		$0.336 \pm 0.007 \pm 0.003$ mm
	Wall, beam right downstream		$0.313 \pm 0.008 \pm 0.003$ mm
Carbon multi foil	(-15, -7.5, 0, 7.5, 15) cm	99.5%	0.042 ± 0.001 g/cm^2 (all foils)
Al Dummy[a,b]	-10 cm		0.359 ± 0.0003 g/cm^2
	+10 cm		0.367 ± 0.0003 g/cm^2
Carbon hole[b]	0 cm	99.95%	0.08388 ± 0.00012 g/cm^2
Tantalum Thin	0 cm	99.9%	0.021487 ± 0.000078 g/cm^2
Tantalum Thick	0 cm	99.9%	0.12237 ± 0.000341 g/cm^2
BeO	0 cm	99.0%	0.149 ± 0.001 g/cm^2

[a] All aluminum used for the cryo-target and the Al Dummy are made from Al 7075 T-6 plates.
[b] Both Al Dummy and Carbon Hole targets had a 2-mm hole to calibrate the target motion relative to the beam position.
[c] The first error bar comes from the standard deviation of multiple measurements at different positions on the target, and the second error is from calibration of the instrument.

Table 2: Position, material, and thickness of the target system used in this experiment. The position is defined along the beam direction with respect to the hall center, see Fig. 5.

When using a fluid target for electron scattering, the energy deposit of the electron beam in the target can cause local density fluctuations. This will add noise to the measurement that cannot be improved by increasing statistics. This systematic effect, often called "target boiling effect" although it is not related to an actual phase change of the target, was measured at the beginning of the experiment for different beam transverse sizes and target cooling conditions, see section 3.3. During production data taking, the transverse size of the beam was controlled such that the boiling effect did not visibly widen the statistical uncertainty of the asymmetry measurement.

2.5. Spectrometers, Detectors, and DAQ

The Hall A high resolution spectrometers (HRS) are a pair of identical spectrometers whose magnet system each consists of one dipole and three focusing quadruples in a $Q_1Q_2DQ_3$ sequence [53]. The spectrometer and their standard detector package served to select for and to measure the kinematics quantities (E', θ) while suppressing backgrounds originating from the target. The spectrometers were designed to have a reasonable acceptance with excellent angle and momentum resolutions, high accuracy in the reconstructed kinematic variables of the events and precise normalization of the cross section.

Figure 6 shows a sideview of the HRS and its detector package. In each HRS, two layers of scintillators provide fast timing information of the scattered particles, vertical drift chambers (VDCs) provide tracking information, and a gas Cherenkov and a double-layered lead-glass detector provides the particle identification (PID).

To achieve the high resolution and accuracy in determining the event position, scattering angle and momentum, the HRS features an optics focusing system that can be described as a simple matrix operation between the original interaction point at the target $(x_{tg}, y_{tg}, \theta_{tg}, \phi_{tg})$ (in the target coordinate system [53, 68]) and the positions and angles of the particle detected at the focal plane (x, θ, y, ϕ) [53, 68], where the focal plane refers to the first of the four high voltage wire planes of the VDC. This optics matrix varies with the beam energy and the spectrometer angle and momentum settings, and must be calibrated every time when these conditions are changed. The optics calibration directly affects the determination of the Q^2-values of the present experiment and will be described in Sec. 3.5.

The DAQ [54] of this experiment utilized signals from the two scintillator planes, the CO_2 gas Cherenkov counter and the double-layered lead glass detector. Both electron and pion triggers were formed. To better understand the counting deadtime of the DAQ, two sets of electronics were formed for each trigger, which were expected to differ only in the deadtime. These two sets of triggers will be referred to as the "narrow" and the "wide" paths, with the

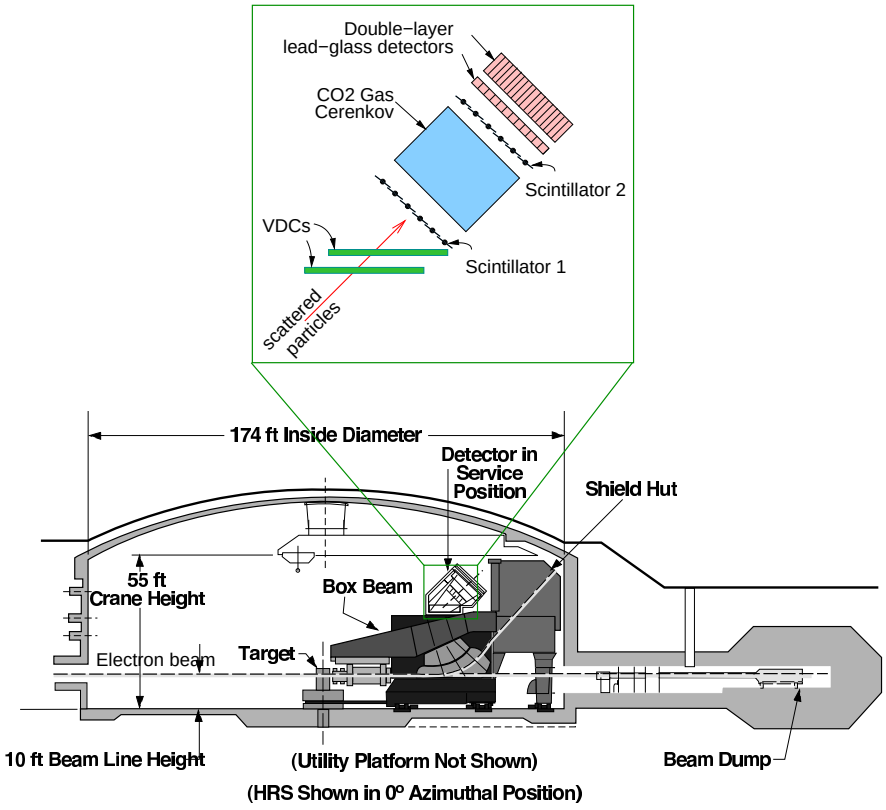

Figure 6: Bottom: Schematic diagram for the HRS in Hall A of JLab, figure taken from Ref. [53]. Top: Zoom-in view of the detector package in the HRS.

narrow path exhibiting less deadtime loss. The electron and pion triggers were sent to digital scalers where they were integrated over each helicity window of the electron beam. The standard tracking detector (the VDCs) was turned off during production data taking because it might not endure the expected high event rates. During low-rate calibration runs, the VDCs were turned on to study the efficiencies of the triggering detectors. Detailed results on the efficiencies of the electron and pion triggers, the background contamination in each trigger, and the counting loss due to deadtime were analyzed in detail and reported in Ref. [54].

3. Data Analysis

The experiment ran between October 26th and December 22nd, 2009. Data were taken first with a 6-GeV beam at two DIS settings at $Q^2 = 1.085$ and 1.901 (GeV/c)^2. These were the main production kinematics and will be referred to as DIS#1 and DIS#2, respectively. Due to limitations in the spectrometer magnets, DIS#1 was taken only on the Left HRS, while DIS#2 was taken on both Left and Right HRSs. A total of 1.02×10^7 beam helicity pairs were selected to formed the final electron sample for $Q^2 = 1.085$ (GeV/c)^2, and 2.5×10^7 pairs for the $Q^2 = 1.901$ (GeV/c)^2 measurement. The statistical precision achieved was 3% at $Q^2 = 1.1$ (GeV/c)^2 and 4% at $Q^2 = 1.9$ (GeV/c)^2. The systematic uncertainty achieved was smaller than 3%.

Data were taken at five additional nucleon resonance settings to provide input for electromagnetic radiative corrections. Two of the resonance settings (RES IV and V) were taken with the 6 GeV beam on the Left HRS, between DIS#1 and #2, and three other resonance settings (RES I, II and III) were taken with a 4.8 GeV beam at the end of the experiment, on either Left or Right HRS. For RES#I which was taken on the left HRS only, the Q_1 and the dipole magnets were set at 4.00 GeV/c, but its Q_2 and Q_3 were limited to 3.66 GeV/c due to a power supply malfunction. Dedicated measurements for the beam transverse asymmetry – also called normal asymmetry A_n – were carried out at DIS #1 and #2 in which the beam spin was directed fully perpendicular to the scattering plane. An overview of the beam energy and spectrometer settings for each kinematics, the observed scattered electron rate and the ratio in π^-/e rates are shown in Table 3 in chronological order.

HRS	Date	Kine#	E_b (GeV)	θ_0	E'_0 (GeV)	R_e(kHz)	R_π/R_e
Left	11/04-12/01/2009	DIS#1	6.0674	12.9°	3.66	≈ 210	≈ 0.5
	12/01-12/02/2009	A_n	6.0674	12.9°	3.66	≈ 210	≈ 0.5
	12/02/2009	RES V	6.0674	14°	3.66	≈ 130	< 0.7
	12/03/2009	RES IV	6.0674	15°	3.66	≈ 80	< 0.6
	12/04-12/17/2009	DIS#2	6.0674	20.0°	2.63	≈ 18	≈ 3.3
	12/17-12/19/2009	RES I	4.8674	12.9°	4.0	≈ 300	< 0.25
	12/19-12/22/2009	RES II	4.8674	12.9°	3.55	≈ 600	< 0.25
Right	11/04-12/01/2009	DIS#2	6.0674	20.0°	2.63	≈ 18	≈ 3.3
	12/01-12/02/2009	A_n	6.0674	20.0°	2.63	≈ 18	≈ 3.3
	12/02-12/17/2009	DIS#2	6.0674	20.0°	2.63	≈ 18	≈ 3.3
	12/17-12/22/2009	RES III	4.8674	12.9°	3.1	≈ 400	< 0.4

Table 3: Overview of kinematics settings of this experiment and the observed scattered electron rate R_e and the charged pion to electron rate ratio R_π/R_e. The kinematics include the beam energy E_b, and the spectrometer central angle θ_0 and central momentum E'_0. Measurement of the transverse asymmetry A_n was performed at the production DIS settings on December 1-2. For RES#I which was taken on the left HRS only, the Q_1 and the dipole magnets were set at 4.00 GeV/c, but its Q_2 and Q_3 were limited to 3.66 GeV/c due to a power supply malfunction. The electron rate R_e was obtained directly from the DAQ, while the pion rate was the rate recorded by the DAQ corrected for trigger efficiencies and signal contaminations.

In this section the procedure for the data analysis will be described. The extraction of the raw asymmetries $A^{\rm raw}$ from the DAQ count rates will be described first, followed by beam charge (intensity) normalization and its effect on the measured asymmetry. Then, corrections due to fluctuations in the beam position, angle and energy (section 3.2) are applied to extract the beam-corrected raw asymmetries $A^{\rm bc,raw}$. Results on the target boiling effect are presented next (section 3.3). Results on beam polarization are presented in section 3.4 which constitute a major normalization to the asymmetry, leading to the preliminary physics asymmetry $A^{\rm phys}_{\rm prel.}$. Calibrations of the beam position and HRS optics are crucial for evaluation of the event kinematics (section 3.5), and a full scale simulation of the HRS transport functions was carried out to confirm our understanding of the kinematics resulting from these calibrations (section 3.6). Next, corrections to the preliminary physics asymmetries due to various backgrounds will be presented in detail (section 3.7).

Radiative corrections due to energy losses of the incident and the scattered electrons will be presented (section 3.8), followed by corrections due to the higher-order $\gamma\gamma$ box diagrams (section 3.9). After all corrections are applied, the preliminary physics asymmetries become the final physics asymmetry results presented in section 4.1.

3.1. Forming Raw Asymmetries

The scattered electrons and pions were counted by the DAQ for each 33 ms helicity window. The response of each beam monitor, including BCM and all BPMs, were digitized and integrated over the same helicity windows and recorded. For each window pair i, the pair-wise raw electron cross-section asymmetry $A_i^{\rm raw}$ in each HRS was computed from the the DAQ counts $c_i^{+(-)}$ normalized to the integrated beam intensity $I_i^{+(-)}$ in the positive (negative) helicity window:

$$A_i^{\rm raw} \quad = \quad \left(\frac{\frac{c_i^+}{I_i^+} - \frac{c_i^-}{I_i^-}}{\frac{c_i^+}{I_i^+} + \frac{c_i^-}{I_i^-}} \right) \, . \tag{38}$$

If the noise from beam fluctuation and target boiling effect is negligible, the uncertainty is given by the purely statistical value:

$$\delta A_{i,\rm stat}^{\rm raw} \quad = \quad \sqrt{\frac{1}{c_i^+ + c_i^-}} \, . \tag{39}$$

If a total of n window pairs have been collected, the average raw asymmetry $A^{\rm raw}$ was formed by

$$A^{\rm raw} = \langle A_i^{\rm raw} \rangle \equiv \frac{\sum_{i=1}^n A_i^{\rm raw}/(\delta A_{i,\rm stat}^{\rm raw})^2}{\sum_{i=1}^n 1/(\delta A_{i,\rm stat}^{\rm raw})^2} \, , \tag{40}$$

and its statistical uncertainty is

$$\delta A_{\rm stat}^{\rm raw} \quad = \quad \sqrt{\frac{1}{N^+ + N^-}} \approx \frac{\delta A_{i,\rm stat}^{\rm raw}}{\sqrt{n}} \, , \tag{41}$$

where $N^{\pm} = \sum_{i=1}^n c_i^{\pm}$ refer to the total electron counts from the n window pairs and the approximation is valid if the beam current remains constant between its two helicity states.

When forming raw asymmetries, loose requirements were imposed on the beam quality: periods with low beam current or with the energy measured in BPM12x differing by more than 10σ from its nominal value were rejected, removing about 10% of the total data sample. No beam-helicity-dependent cuts were applied. The uncertainty in $A^{\rm raw}$ might be enlarged by helicity-dependent fluctuations in the beam intensity, position, angle, energy, and target boiling, causing a non-statistical contribution to the measurement. Therefore, an important criterium for a successful asymmetry measurement is to control non-statistical noise to a negligible level, which ensures that the main source of the uncertainty is the well-understood statistical fluctuation, and minimizes the run time.

3.2. Beam Intensity Normalization, Beam Corrections, and Their Systematic Fluctuations

For all PVES experiments at JLab, the polarized beam and the target were designed such that the fluctuations in the helicity difference in the signal between a pair of successive windows were dominated by scattered electron counting statistics. An example of possible non-statistical contributions is a window-to-window relative beam intensity asymmetry $A_I \equiv (I^+ - I^-)/(I^+ + I^-)$ with an uncertainty $\delta(A_I)$. During the PVDIS experiment, A_I for a 30 ms beam window at a 100 μA current was measured to be below 4×10^{-5}, with δA_I between 2×10^{-4} and 2×10^{-3} depending on the quality of the laser and the beam tune. At a 1-MHz counting rate the counting statistics for each 66-ms beam helicity pair is $\delta(A_i^{\rm raw}) = 0.00387$ [Eq. (39)]. The actual value was larger because the rate was lower than 1 MHz (Table 3). Therefore, the small $\delta(A_I)$ of the polarized beam at JLab guaranteed $\delta(A_I) \ll \delta A_{i,\rm stat}^{\rm raw}$ [see Eq. (39)] for this experiment. Thanks to the feedback control to the laser at the polarized source, the cumulative average for A_I throughout the experiment was below 0.1 ppm.

Beam properties other than the intensity do not enter the direct asymmetry evaluation, but they might affect the asymmetry measurement. To study how such beam properties affect the measured asymmetry, we first re-write Eq. (38) as

$$A_i^{\rm raw} \approx \left(\frac{c^+ - c^-}{c^+ + c^-}\right)_i - \left(\frac{I^+ - I^-}{I^+ + I^-}\right)_i = A_{i,c}^{\rm raw} - \left(\frac{1}{I^+ + I^-}\right)_i \Delta I_i \ , \tag{42}$$

where $A_{i,c}^{\rm raw}$ is the raw count asymmetry and $\Delta I_i \equiv (I^+ - I^-)_i$. This approximation is valid for $A_I \ll 1$ which was true as stated in the previous section. Similarly, the raw asymmetry might be affected by fluctuations in beam energy, position and angle. These beam-related corrections (bc) can be parametrized as:

$$(A^{\rm bc,raw})_i = A_i^{\rm raw} - \sum_j [\alpha_j (\Delta X_j)_i]. \tag{43}$$

Here, X_j denote beam parameters such as energy, position and angle, $\Delta X_j \equiv X_j^+ - X_j^-$ their corresponding helicity fluctuation, and α_j coefficients that depend on the kinematics of the specific reaction being studied as well as the detailed spectrometer and detector geometry of the experiment.

The five BPMs equipped during this experiment: BPMA-X (horizontal), BPMA-Y (vertical), BPMB-X,Y, and BPM12x allowed measurements of the relative change in the beam energy, position and angle within one helicity window pair. One can then write

$$(A^{\rm bc,raw})_i = A_i^{\rm raw} - \sum_j [c_j (\Delta x_j)_i] \ , \tag{44}$$

where x_j is the beam position measured by the five BPMs (BPMAX,Y, BPMBX,Y, BPM12x) and $c_j \equiv \alpha_j \partial X_j / \partial x_j$. It is worth noting that this approach of making corrections window by window automatically accounts for occasional random instabilities in the accelerator.

If one corrects the pair-wise asymmetry for the beam fluctuations based on Eq. (44), the resulting asymmetry averaged over a certain number of helicity pairs can be written as

$$A^{\rm bc,raw} \equiv \langle A_i^{\rm bc,raw} \rangle = \langle A_i^{\rm raw} \rangle - \sum_j c_j \langle \Delta x_j \rangle = A^{\rm raw} - \sum_j \Delta A_{x_j} \tag{45}$$

where $\Delta A_{x_j} \equiv c_j \langle (x_j^+ - x_j^-)_i \rangle$ represents the correction needs to be applied to the raw asymmetry due to helicity-dependent fluctuation in x_j.

For this experiment, the values of c_j were obtained using two methods: The first one is called the "dithering" method [19], in which the beam position, angle, and energy were modulated periodically during data taking. The values of c_j were then calculated from the resulting variation in the measured asymmetry recorded for each of the five BPM variables. The energy of the beam was varied by applying a control voltage to a vernier input on a cavity in the accelerator's South Linac. The beam positions and angles were modulated using seven air-core corrector coils in the Hall A beamline upstream of the dispersive arc [19]. Because these modulation periods represent quality data, they were included in the production data sample with the appropriate corrections made. In the second method the values of c_j were evaluated utilizing only natural fluctuations of the beam position, angle, and energy. This is called the "regression" method. The difference in the corrected asymmetry between the dithering and the regression method was used as the uncertainty in the beam-corrected raw asymmetries $A_{\rm bc,raw}$.

To control the beam position differences at BPMA and BPMB, the feedback system controlled by the HAPPEx DAQ made adjustments of the circular polarization of the laser beam. The resulting beam position differences were in the range $0.01 - 0.1\mu$m at the target for the majority of the data taking period. Based on the measured c_j values this resulted in ΔA_{x_j} in the range $0.1 - 1$ ppm. The cumulative averages for ΔA_{x_j} were found to be below 0.1 ppm integrated over the whole experiment. The measured asymmetry was found to be much less sensitive to beam energy fluctuations than to those of the beam position. Table 4 shows the corrections due to fluctuations in the five measured beam positions using the dithering method. The narrow and the wide paths of the DAQ produced very similar results, although there were slight differences in their event collection due to DAQ deadtime and different timing alignment between electronic modules, resulting in a slightly better PID performance of the wide-paths [54]. Still, the narrow-path asymmetry results were used to produce the physics results of the present experiment because of their smaller deadtime.

Monitor	Left DIS#1 $\Delta A_{\rm dit}$ (ppm)		Left DIS#2 $\Delta A_{\rm dit}$ (ppm)		Right DIS# 2 $\Delta A_{\rm dit}$ (ppm)	
DAQ path	narrow	wide	narrow	wide	narrow	wide
BPM4AX	0.173	0.179	0.513	0.569	-0.172	-0.182
BPM4AY	0.001	-0.010	0.286	0.262	-0.021	-0.027
BPM4BX	-0.152	-0.159	-0.368	-0.430	0.226	0.237
BPM4BY	-0.028	-0.020	-0.262	-0.243	-0.008	-0.003
BPM12x	0.000	0.000	0.024	0.022	-0.003	-0.003
Total	-0.006	-0.010	0.193	0.180	0.022	0.022

Monitor	RES I $\Delta A_{\rm dit}$ (ppm)		RES II $\Delta A_{\rm dit}$ (ppm)		RES III $\Delta A_{\rm dit}$ (ppm)		RES IV $\Delta A_{\rm dit}$ (ppm)		RES V $\Delta A_{\rm dit}$ (ppm)	
DAQ path	narrow	wide	narrow	wide	narrow	wide	narrow	wide	narrow	wide
BPM4AX	-0.175	-0.178	0.313	0.320	-0.013	0.000	-1.004	-1.192	-3.708	-3.631
BPM4AY	0.230	0.224	0.096	0.107	0.047	0.046	0.328	0.328	0.400	0.317
BPM4BX	0.369	0.375	-0.568	-0.582	0.020	-0.005	1.398	1.596	4.754	4.603
BPM4BY	-0.139	-0.133	-0.132	-0.143	-0.038	-0.037	-0.235	-0.250	-0.265	-0.183
BPM12x	-0.010	-0.011	0.045	0.045	-0.005	-0.005	0.002	0.003	-0.035	-0.036
Total	0.275	0.277	-0.246	-0.253	0.011	-0.001	0.489	0.485	1.146	1.070

Table 4: Corrections to DIS (top) and resonance (bottom) asymmetries evaluated using the dithering method, $\Delta A_{\rm dit}$. The "narrow" and "wide" refer to the DAQ trigger type [54]. The corrections were applied as $A_{\rm dit}^{\rm bc,raw} = A^{\rm raw} - \Delta A_{\rm dit}$ [Eq. (45)].

	Left DIS#1	Left DIS#2	Right DIS#2
$A^{\rm raw}$, narrow (ppm)	-78.4 ± 2.7	-140.5 ± 10.4	-139.9 ± 6.6
$A_{\rm dit}^{\rm bc,raw}$, narrow (ppm)	-78.5 ± 2.7	-140.3 ± 10.4	-139.8 ± 6.6
$A_{\rm reg}^{\rm bc,raw}$, narrow (ppm)	-78.5 ± 2.7	-140.5 ± 10.4	-140.3 ± 6.6
$\lvert A_{\rm dit}^{\rm bc,raw} - A_{\rm reg}^{\rm bc,raw}\rvert$, narrow (ppm)	0.1	0.2	0.5
$A^{\rm raw}$, wide (ppm)	-78.2 ± 2.7	-140.3 ± 10.4	-140.9 ± 6.6
$A_{\rm dit}^{\rm bc,raw}$, wide (ppm)	-78.3 ± 2.7	-140.1 ± 10.4	-140.9 ± 6.6
$A_{\rm reg}^{\rm bc,raw}$, wide (ppm)	-78.3 ± 2.7	-140.3 ± 10.4	-141.4 ± 6.6
$\lvert A_{\rm dit}^{\rm bc,raw} - A_{\rm reg}^{\rm bc,raw}\rvert$, wide (ppm)	0.1	0.1	0.5

	Left RES I	Left RES II	Right RES III	Left RES IV	Left RES V
$A^{\rm raw}$, narrow (ppm)	-55.4 ± 6.8	-63.5 ± 5.9	-54.4 ± 4.5	-104.5 ± 15.3	-69.0 ± 21.3
$A_{\rm dit}^{\rm bc,raw}$, narrow (ppm)	-55.1 ± 6.8	-63.8 ± 5.9	-54.4 ± 4.5	-104.0 ± 15.3	-67.9 ± 21.3
$A_{\rm reg}^{\rm bc,raw}$, narrow (ppm)	-55.2 ± 6.8	-63.6 ± 5.9	-54.6 ± 4.5	-104.3 ± 15.3	-68.6 ± 21.2
$\lvert A_{\rm dit}^{\rm bc,raw} - A_{\rm reg}^{\rm bc,raw}\rvert$, narrow (ppm)	0.1	0.2	0.2	0.3	0.7
$A^{\rm raw}$, wide (ppm)	-54.9 ± 6.8	-63.6 ± 5.9	-54.0 ± 4.5	-105.0 ± 15.3	-69.0 ± 21.5
$A_{\rm dit}^{\rm bc,raw}$, wide (ppm)	-54.6 ± 6.8	-63.9 ± 5.9	-54.0 ± 4.5	-104.6 ± 15.3	-67.9 ± 21.5
$A_{\rm reg}^{\rm bc,raw}$, wide (ppm)	-54.6 ± 6.8	-63.7 ± 5.9	-54.2 ± 4.5	-104.9 ± 15.2	-68.7 ± 21.4
$\lvert A_{\rm dit}^{\rm bc,raw} - A_{\rm reg}^{\rm bc,raw}\rvert$, wide (ppm)	0.1	0.2	0.2	0.3	0.8

Table 5: Measured raw asymmetries from the narrow and the wide triggers after applying corrections from beam energy and position changes using the dithering and the regression methods. The asymmetry errors shown are statistical only. The differences between the two corrected asymmetries, $|A_{\rm dit}^{\rm bc,raw} - A_{\rm reg}^{\rm bc,raw}|$, were used as the uncertainty from beam corrections. The dithering-corrected asymmetries were used in further analysis, although dithering and regression methods are in principle equivalent. The narrow and the wide paths of the DAQ produced very similar results, with slight differences in their event collection due to DAQ deadtime and different timing alignment between electronic modules. The narrow-path asymmetry results ($|A_{\rm dit}^{\rm bc,raw}$, narrow) were used in further analysis to produce the physics results because of their smaller deadtime [54].

The measured raw asymmetries $A^{\rm raw}$ are shown in Table 5 along with the corrected asymmetries based on both the dithering and regression methods, $A_{\rm dit}^{\rm bc,raw}$ and $A_{\rm reg}^{\rm bc,raw}$.

Compared to the uncertainties from counting statistics, one can see that overall the corrections due to beam fluctuation were quite small, and their uncertainties are negligible. The asymmetry measurement was completely dominated by the counting statistics of the scattered electrons [54].

3.3. Target boiling effect on the measured asymmetry

As described in section 2.4, the electron beam deposited energy in the liquid deuterium target and caused additional noise to the measurement. This target boiling effect would manifest itself as an increase in the standard deviation of the measured pair-wise asymmetry $A^{\rm raw}$ above that expected from the counting statistics of Eq. (39,41). Rastering the beam to larger transverse sizes reduces the beam heating and thus the boiling effect.

Studies of the target boiling effect was performed. For each measurement a Gaussian was fitted to the distribution of the pair-wise asymmetries with δA given by the fitted width. Figure 7 shows the measured δA, taken at kinematics DIS #2 for various raster sizes at two beam currents 100 and 115 μA.

Results of δA in Fig. 7 were fitted with the functional form $p_0 x^{p_1} + p_2$ where x is the raster size in mm. The parameter p_2 represents the purely statistical fluctuation that depends only on the beam current, while the term $p_0 x^{p_1}$ is an empirical term that describes the size of target boiling. Using the approximate electron rate (Tabel 3), the purely statistical uncertainty for 66-ms wide beam helicity pairs is 0.029 at 100 μA and 0.027 at 115 μA. The fit results for p_2 agree with the expectation very well. The fit results for p_0 and p_1 show that the broadening due to boiling at a 4×4 mm^2 raster size, $p_0 x^{p_1}$ with $x = 4$, is at the level of 569 ppm for 100 μA and 1407 ppm for 115 μA. This is quite small compared to the value from purely statistical fluctuations ($p_0 \sim 10^4$ ppm), and thus the boiling effect did not contribute significantly to the uncertainty of the asymmetry measurement.

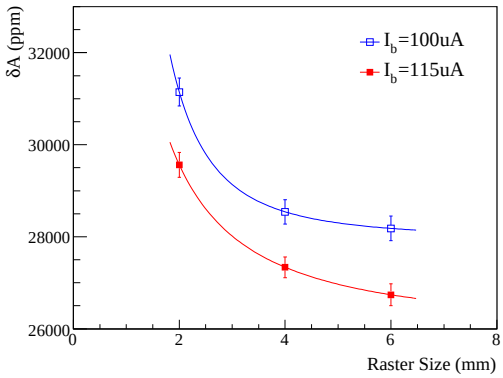

Figure 7: Measured standard deviation of the pair-wise asymmetries at kinematics DIS# 2, for various raster sizes and two beam currents 100 and 115 μA. The curves show the results of the fit $\delta A = p_0 x^{p_1} + p_2$ where x is the raster size in mm. The parameter p_2 represents the purely statistical fluctuation that depends only on the beam current and not the raster size, while the term $p_0 x^{p_1}$ is an emperical term that describes the size of target boiling. The fit results for 100 μA are $p_0 = (1.77 \pm 1.94) \times 10^4$, $p_1 = -2.48 \pm 1.85$, $p_2 = 27973.0 \pm 681.7$; and for 115 μA are $p_0 = (9.40 \pm 3.78) \times 10^3$, $p_1 = -1.37 \pm 1.09$, $p_2 = 25941.0 \pm 1433.4$. At a raster size of 4×4 mm^2 ($x = 4$), the boiling noise is at the level of 569 ppm for 100 μA and 1407 ppm for 115 μA, and is negligible compared to the value from purely statistical fluctuations.

Figure 8 shows the measured δA for various beam currents I performed with a 4×4 mm^2 square raster. If the measurement is dominated by statistical uncertainty, one expects $\delta A \propto \sqrt{I}$. Fit results of the measured δA indeed agree very well with this expectation, indicating that boiling effects at the running condition of this experiment was negligible.

3.4. Beam Polarization

As described in the previous section, the electron raw asymmetry was first corrected for the beam intensity and other beam-related properties such as position, angle and energy. The resulting asymmetry $A^{\rm bc,raw}$ is referred to as the measured asymmetry, $A^{\rm meas}$, and must then be corrected for the beam polarization P_e:

$$A^{\rm phys}_{\rm prel.} = A^{\rm meas} / P_e \ , \tag{46}$$

to obtain the preliminary physics asymmetry $A^{\rm phys}_{\rm prel.}$. Both Compton and Møller polarimeters described in section 2.3 were used.

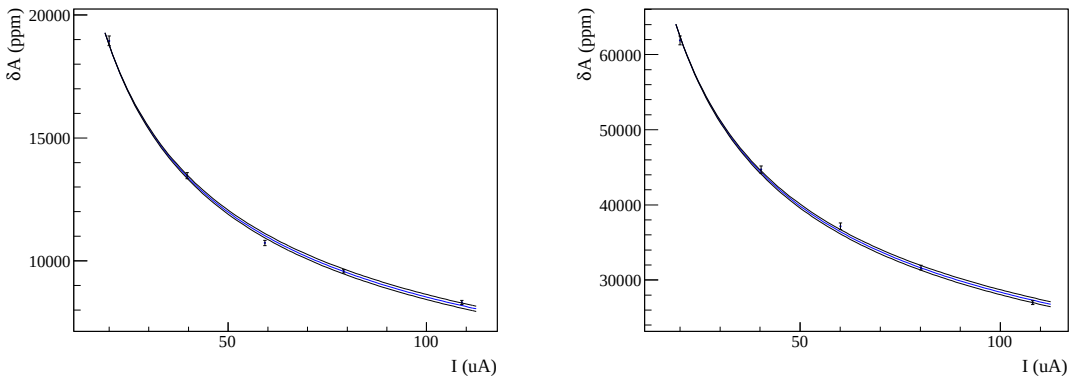

Figure 8: Measured standard deviation of the pair-wise asymmetries at various beam currents for DIS# 1 (left) and # 2 (right), with a $4\times4\,\mathrm{mm}^2$ square raster. The curves show the results of the fit $\delta A \propto I^{p_3}$ and its error band. The fit results are $p_3 = 0.4900 \pm 0.0076$ and $p_3 = 0.4897 \pm 0.0072$ for DIS# 1 and # 2 respectively. These results are in good agreement with pure counting statistics ($\delta A \propto \sqrt{I}$).

During our experiment, the Møller polarimeter was available the entire time, while the Compton polarimeter initially suffered from a high background and only produced results in the last three weeks of the 2-month 6-GeV run period. The Compton polarimeter was also not available during the 4.8-GeV run period. Figure 9 shows the Møller polarimetry measurements taken with the 6 GeV beam. During the three weeks when both polarimeters were functioning, the average beam polarization from constant fits is 88.74% for Møller and 89.45% for Compton. The results from the two polarimeters are compared in Fig. 10. Note that the beam polarization can fluctuate over time due to motion of the laser position on the photocathode and photocathode aging.

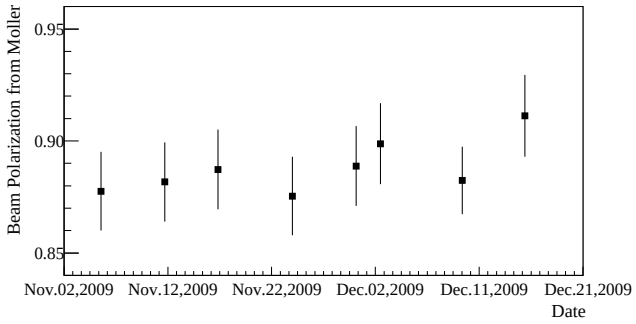

Figure 9: Polarization results from the Møller polarimeter measurements taken with a beam energy of 6.067 GeV. The error bars represent the quadratical sum of the statistical and systematic errors. However, for each measurement the statistical uncertainty was in the order of 0.1%, much smaller than the systematic error. An additional measurement was done with a beam energy of 4.867 GeV at the end of the run period, which gave a similar polarization.

The experimental asymmetries were corrected for the beam polarization as follows:

1. When the Compton polarimeter was not available (before Dec. 2nd and after Dec. 17th, 2009), only Møller results were used. Each Moller result was used until the next measurement was available.
2. When there were both Compton and Møller measurements (from Dec. 2nd to Dec. 17th, 2009), the Compton data were averaged first for the time interval between two Møller measurements, then was averaged with the corresponding Moller measurement from the beginning of the interval. The systematic uncertainty of the combined polarization was obtained from that of each method as

$$(\Delta P_b/P_b)_{syst,combined} = 1/\sqrt{(\Delta P_b/P_b)^{-2}_{syst,compton} + (\Delta P_b/P_b)^{-2}_{syst,moller}}, \tag{47}$$

   thus was smaller than the systematic uncertainty of either polarimetry. Each combined result was used until a next Moller measurement was available.
3. The beam polarization was corrected run by run for DIS#1 and #2. For resonance kinematics, the run period was short and a single correction was used for each kinematics.

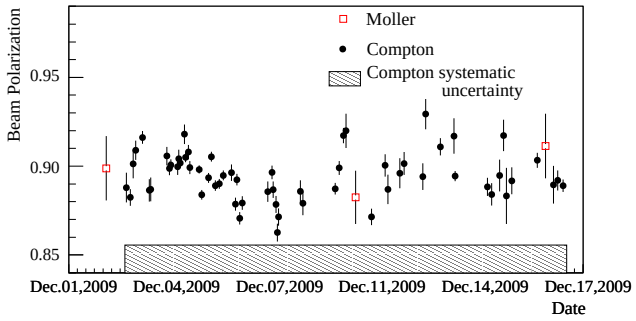

Figure 10: Comparison between Compton (black solid circles) and Møller (red open squares) measurements taken during the time period when both polarimeters were available. The beam energy was 6.067 GeV. The error bars for Moller represent the quadratical sum of the statistical and systematic errors, with the statistical error is smaller than the systematic by one order of magnitude. For Compton measurement, the statistical error are plotted with the data points and the systematic error (1.92% relative) are plotted along the horizontal axis. A constant fit to Compton measurements gave an average of 89.45% while the average of Moller results was 88.74%.

The beam polarization corrections are shown in Table 6 for all kinematics.

	Left DIS#2	Right DIS#2	RES IV and V
Combined P_e	$(89.29 \pm 1.19)\%$	$(88.73 \pm 1.50)\%$	$(89.65 \pm 1.24)\%$

	Left DIS#1	RES I, II and III
Moller P_e	$(88.18 \pm 1.76)\%$	$(90.40 \pm 1.54)\%$

Table 6: Average beam polarization P_e for each kinematics. These are either the combined results of Compton and Moller measurements (top), or results from Moller alone (bottom), depending on which polarimeter was available during the corresponding run period. For DIS#1 and #2 the corrections were applied run-by-run and the statistically-averaged value of P_e is shown. For all resonance kinematics which had short running period, a single value was used for each setting.

3.5. Calibration of the HRS Optics

To accurately determine the kinematics (Q^2, x, W) of each event, one must determine the absolute beam position on the target, and reconstruct the vertex position, the scattering angle and the scattered electron's momentum. These are provided by beam position calibration and the HRS optics calibration, as described below.

3.5.1. Beam Position Calibration

As described in Sec. 2.2, the beam position information for each event was obtained from the raster current rather than from the delayed BPM information. Calibrations between the raster current and the beam position thus became necessary. The BPM calibration can be described as:

$$\text{bpm } x = \langle \text{bpm offset } x \rangle + \langle \text{raster current } x \rangle \times \frac{\sigma_{\text{bpm},x}}{\sigma_{\text{raster current}}}, \quad (48)$$

$$\text{bpm } y = \langle \text{bpm offset } y \rangle + \langle \text{raster current } y \rangle \times \frac{\sigma_{\text{bpm},y}}{\sigma_{\text{raster current}}}. \quad (49)$$

Figure 11 shows the beam spot distributions projected to the target using the calibrated BPMA and BPMB information.

3.5.2. Optics Calibration Procedure and the Resulting Uncertainties in Q^2 Determination

The trajectory and momentum of each electron detected was determined by calibration of the transport functions (optics) of each HRS. During optics calibration runs, the VDCs were turned on to provide precise information on the particle trajectory, from which the hit position and angles at the focal plane (x, θ, y, ϕ) can be determined [53, 68]. The next step is to reconstruct the interaction position, angle, and momentum at the target from these focal plane variables, i.e., to determine the inverse of the HRS optical transport matrix. In practice, instead of a matrix operation, a set of tensors up to the 5th order were used to calculate the target variables from the focal plane values.

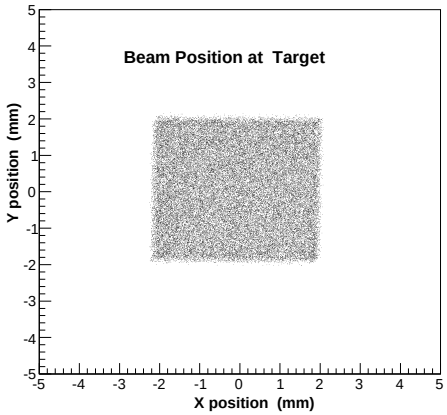

Figure 11: Calibrated beam spot distribution at the target.

The target coordinates of the scattering event, $(x_{tg}, y_{tg}, \theta_{tg}, \phi_{tg})$, are defined in the target coordinate system (TCS) [68] with respect to the spectrometer central ray direction, see Fig. 12. Here the angles θ_{tg} and ϕ_{tg} refer to the tangent of the vertical and horizontal angles relative to the HRS central ray. The spectrometer pointing D is the distance at which the spectrometer misses the Hall center in the direction perpendicular to the spectrometer central ray. The sieve plane corresponds to the entrance of the spectrometer which is located at $L = 1.12$ m from the TCS origin. The particle hit position and the angles at the sieve plane can be directly calculated from the focal plane variables.

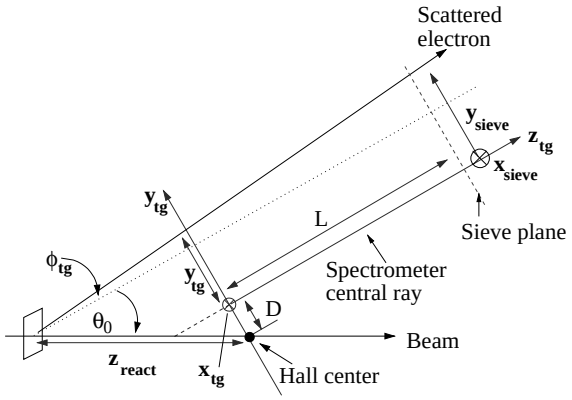

Figure 12: Topview of the target coordinate system (TCS) (x_{tg}, y_{tg}, z_{tg}) and the sieve plane coordinate system $(x_{\rm sieve}, y_{\rm sieve})$. The z_{tg} axis is along the HRS central ray, the y_{tg} axis is pointing to the left, the x_{tg} axis is pointing vertically down, and the origin of the TCS is the point along the HRS central ray that is the closest to the Hall center. The ϕ_{tg} is the tangent of the in-plane angle and θ_{tg} is the tangent of the out-of-plane angle (not shown) w.r.t. the spectrometer central ray. The sieve plane is located at a drift distance $L = 1.12$ m from the TCS origin, with the $y_{\rm sieve}$ axis pointing to the left of the spectrometer entrance and the $x_{\rm sieve}$ axis pointing vertically down. The pointing of the HRS, D, describes how much the HRS central ray misses the Hall center, and θ_0 is the angle of the HRS central ray w.r.t. the beamline. Figure reproduced from Refs. [53, 68]

The calibration procedure involves three separate steps:

1. The vertex position along the beam, $z_{\rm react}$, is related to y_{tg}, ϕ_{tg} in the TCS as well as the pointing D of the spectrometer. The vertex calibration was done by taking data on the multi-foil carbon target with known foil positions. The foil positions were determined from data using the HRS optics matrix, the focal plane variables, and D. The precision on $z_{\rm react}$ in the direction perpendicular to the spectrometer central ray is given by

$$\Delta(z_{\rm react}\sin\theta_0) = \sqrt{(\Delta D)^2 + (\Delta z_{\rm foil}\sin\theta_0)^2 + (\Delta z_{\rm foil\ data}\sin\theta_0)^2}\ . \tag{50}$$

Then, the uncertainty in the scattering angle due to the vertex calibration is

$$\Delta\phi_{tg} = \Delta(z_{\rm react}\sin\theta_0)/L\ . \tag{51}$$

Here $\Delta z_{\rm foil} = \pm 2.5$ mm is the uncertainty of the actual foil position caused by possible shifts of the target ladder during the target cool-down. The precision of D can be obtained from a spectrometer pointing survey with a typical precision of ± 0.5 mm. If a survey was not available, the value of D can be derived from surveys performed at a previous spectrometer angle setting. In this case, one compares the multi-carbon-foil data before and after the spectrometer rotation. If the observed shifts in z in all foil positions can be explained consistently by a global change in D, then the shift is added to the value of D from the previous survey and the uncertainty of D is taken as ± 0.5 mm. If neither carbon foil data nor a survey was available, ΔD is taken to be ± 5 mm which is the limit of how much the spectrometer can physically miss the Hall center. The quantity $\Delta z_{\rm foil\ data}$ is ± 0.1 mm or the observed discrepancy in the foil poisition between calibration data and the expected values, whichever is larger.

2. The scattering angles, θ_{tg}, ϕ_{tg}, were calibrated by inserting a so-called "sieve slit" plate – a 0.5-mm thick tungsten plate with an array of pinholes – at the entrance of the spectrometer. Reconstruction of hole positions depends on the angle elements of the optical matrix. The calibration precision is determined by the knowledge of the actual hole positions $x_{\rm hole}$, $y_{\rm hole}$ w.r.t. the center of the spectrometer, and the remaining differences between the reconstructed hole positions $x_{\rm hole\ data}$, $y_{\rm hole\ data}$ and the expected values.
   The most straightforward way to determine $x_{\rm hole}, y_{\rm hole}$ is by a survey of the sieve slit plate. The survey uncertainty is ± 0.5 mm for both directions. Past experience has shown that the horizontal position $y_{\rm hole}$ is highly reproducible, to ± 0.1 mm, and the vertical position $x_{\rm hole}$ is reproducible to ± 0.5 mm due to the fact that this is the direction in which the sieve plate is moved into or out of the HRS entrance. If no survey was available but the sieve slit had remained in its position, results from earlier surveys were used with these additional uncertainties added. The angle uncertainties from sieve slit calibrations are:

$$\Delta\theta_{tg} = \sqrt{(\Delta x_{\rm hole})^2 + (\Delta x_{\rm hole\ data})^2}/L\ , \tag{52}$$

$$\Delta\phi_{tg} = \sqrt{(\Delta y_{\rm hole})^2 + (\Delta y_{\rm hole\ data})^2}/L\ , \tag{53}$$

   where the in-plane angle ϕ_{tg} affects the scattering angle θ directly, while the out-of-plane angle θ_{tg} affects θ only in the second order and the effect is small.
   If no sieve slit data were taken, the angle calibration of a preceeding experiment can be used based on the high reliability of the HRS. In this case, an additional ± 0.5 mrad of uncertainty should be added to both $\Delta\theta_{tg}$, $\Delta\phi_{tg}$ to account for possible changes in the optics.

3. The most precise way to calibrate the momentum is to use elastic scattering from a carbon target or the proton inside a water target. With a water target, the relative momentum $\delta \equiv dp/p$ with p the HRS central momentum setting can be determined to $\pm 1 \times 10^{-4}$. Due to the high beam energy used, elastic measurement was not possible for the present experiment. However, water target calibration was performed during the preceding experiment (HAPPEx-III) [23]. The HAPPEx-III water calibration results were used for the present experiment and the uncertainty is $\delta = \pm 5 \times 10^{-4}$ thanks to the high stability of the HRS magnets and transport system.

The three calibration steps described above are assumed to be independent from each other, i.e., matrix elements related to position reconstruction have little dependence on those related to angle reconstruction, etc. For all calibration methods above, the optics tensor coefficients were determined from a χ^2 minimization procedure in which the events were reconstructed as close as possible to the known position of the corresponding foil target or the sieve-slit hole.

3.5.3. Optics Calibration Results

During the PVDIS experiment, there were seven kinematics settings in total with one of them carried out on both Left and Right HRS, thus there were a total of eight HRS+kinematics combinations: Left HRS DIS #1, Left and Right HRS DIS #2, Left HRS Resonance (RES) I, Left HRS RES II, Right HRS RES III, Left HRS RES IV, and Left HRS RES V. Either vertex or angle calibrations, or both, were carried out for all eight settings except RES IV and V. The vertex calibration for Left DIS#1 and the angle calibration results for Left RES II are shown in Fig. 13.

3.5.4. Q^2 Uncertainties

The Q^2 of each event was calculated using Eq. (3). The uncertainty in Q^2 is determined by the uncertainties in θ, E and E', but is dominated by the scattering angle uncertainty. The scattering angle is calculated as [53]:

$$\theta = \cos^{-1}\left(\frac{\cos\theta_0 - \phi_{tg}\sin\theta_0}{\sqrt{1+\theta_{tg}^2+\phi_{tg}^2}}\right)\ , \tag{54}$$

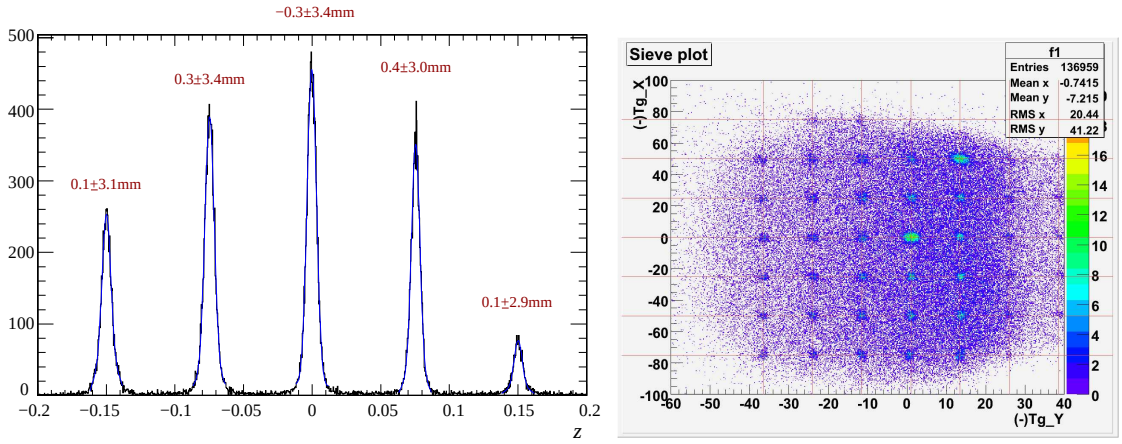

Figure 13: Left: vertex reconstruction for Left DIS#1 (left). The number above each foil is $\Delta z_{\text{foil data}}$, defined as how much the observed foil position misses the expected value. For all foils we have $\Delta z_{\text{foil data}} \leqslant 0.4$ mm. Right: reconstruction of the sieve hole positions (scattered points) compared to the expected positions (grids), for Left RES II. No obvious discrepancy is seen. The axes are oriented such that the sieve hole pattern is as if viewed when facing the spectrometer entrance. Two of the sieve holes are larger than others to allow identifying the center and the orientation of the sieve plate.

thus calibration of the horizontal angle ϕ_{tg} dominates the angle uncertainty. The total uncertainty on the scattering angle is the combination of the vertex calibration Eqs. (50-51) and $\Delta\phi_{tg}$ from the angle calibration:

$$\Delta\theta \approx \sqrt{(\Delta D/L)^2 + (\Delta z_{\text{foil}} \sin\theta_0/L)^2 + (\Delta z_{\text{foil data}} \sin\theta_0/L)^2 + (\Delta\phi_{tg})^2}\ . \tag{55}$$

where $\Delta\phi_{tg}$ is either from Eq. (53) if a sieve slit calibration was available, or from previous calibrations with a 0.5 mrad additional uncertainty added. Here the drift distance is $L = 1.12$ m as shown in Fig. 12.

For some settings during PVDIS, there were both angle and vertex calibrations (Left RES I and II), or only the vertex but not the angle calibration (Left DIS#1, Left DIS#2, Right DIS#2, Right RES III), or neither (Left RES IV and V). For both vertex and angle calibrations, the optics database and some survey results from the HAPPEx-III experiment that ran immediately before this experiment were used. For RES#I which was taken on the left HRS only, the Q_1 and the dipole magnets were set at 4.00 GeV/c, but its Q_2 and Q_3 were limited to 3.66 GeV/c due to a power supply malfunction. This added complexity to the optical calibration for RES#I but did not affect the HRS acceptance and the quality of the optical calibration results. Taking all uncertainties into account, the uncertainty in Q^2 due to HRS optics calibration is summarized in Table 7.

3.6. HRS Simulations

For the present experiment, a simulation package called "HAMC" (Hall A Monte Carlo) was used to simulate the transport function and the acceptance of HRS. The simulation was then used to calculate the effect of electromagnetic radiative corrections and HRS acceptance. To ensure that HAMC works correctly, we simulated the kinematics (Q^2, W, x) of the scattering, and it is expected that the simulated values should agree with the measured ones within the uncertainty of the optics calibration, Table 7.

In HAMC, events were generated with a uniform distribution along the beam direction and within a given raster size and the solid angle $d\Omega = \sin(\theta)\, d\theta\, d\phi$, then transported through the HRS magnets using a set of polynomials that model the electrons' trajectories through the magnetic fields. For RES #I, a separate set of polymonials were developed for the mismatching fields of Q_2 and Q_3. Events that passed all magnet entrance and exit apertures fall within the HRS acceptance and are recorded. Multiple scattering in the target material, energy loss due to external and internal Brehmstrahlung and ionization loss, and the 200 μm resolution of the VDC wires were also taken into account in HAMC. The physical differential cross section $d^2\sigma/(dE' d\Omega)$ and the parity violation asymmetry were calculated using the MSTW PDF parameterization for each simulated event. An average energy loss of of 3 MeV was used for the incident electron beam to account for the effect of transpassing all material along the beamline to the target center.

Because the DAQ used in the present experiment relied on hardware-based PID, PID calibration runs were carried out daily to monitor the detector and the DAQ performance. It was found that the electron efficiency varied with the particle's hit position in the vertical (dispersive) direction on the lead-glass detector. This variation could cause

HRS	Left HRS						Right HRS	
Kinematics	DIS#1	RES V	RES IV	DIS#2	Res I	Res II	DIS#2	Res III
$\theta_0(^\circ)$	12.9	14.0	15.0	20	12.9	12.9	20	12.9
E_b (GeV)	6.067	6.067	6.067	6.067	4.867	4.867	4.867	4.867
E'_0 (GeV)	3.66	3.66	3.66	2.63	4.0[a]	3.66	2.63	3.1
HRS pointing survey?	Y	N	N	Y	N	N	Y	N
δD (survey)(mm)	0.5			0.5			0.5	
Carbon multi foil data available?	Y	N	N	Y	Y	Y	Y	Y
δD (from data, no survey) (mm)					0.5	0.5	0.5	0.5
δD (no survey, no data)(mm)		5.0	5.0					
$\delta z_{\rm foil\ data}$ (mm)	0.4	N/A	N/A	0.4	2.0	0.3	0.7	1.1
$\delta z_{\rm foil}$	2.5	N/A	N/A	2.5	2.5	2.5	2.5	2.5
$\Delta\theta$ from vertex calibration (mrad), Eq. (51)	0.676	4.464	4.464	0.893	0.779	0.672	0.901	0.704
sieve survey	N	N	N	N	N	N	N	N
sieve data	N	N	N	N	Y	Y	N	N
$\Delta x_{\rm hole}$, from prior survey (mm)	0.51	0.51	0.51	0.51	0.51	0.51	0.51	0.51
$\Delta x_{\rm hole\ data}$ (mm)	0.1	N/A	N/A	0.1	0.1	0.1	0.1	0.1
additional $\Delta\phi_{tg}$ (mrad)	0.5[b]	0.5[b]	0.5[b]	0.5[b]			0.5[c]	0.5[c]
$\Delta\theta$ from angle calibration (mrad), Eq. (53)	0.682	0.676	0.676	0.682	0.464	0.464	0.676	0.676
Total $\Delta\theta$ (mrad)	0.960	4.515	4.515	1.124	0.907	0.816	1.134	0.976
Total $\Delta\theta/\theta$ (%)	0.426	1.848	1.725	0.322	0.403	0.363	0.325	0.434
$\Delta E'_0/E'_0$	5×10^{-4}							
Total $\Delta Q^2/Q^2$ (%)[d]	0.853	3.696	3.449	0.644	0.805	0.725	0.650	0.867

[a] For RES#I which was taken on the left HRS only, the Q_1 and the dipole magnets were set at 4.00 GeV/c, but its Q_2 and Q_3 were limited to 3.66 GeV/c due to a power supply malfunction;
[b] Due to using sieve calibration taken at Left RES#3;
[c] Due to using optics database from HAPPEx-III;
[d] Including uncertainties due to both scattering angle $\Delta\theta$ and momentum $\Delta E'$, but is dominated by the former.

Table 7: Uncertainty in Q^2 determination derived from optics calibration. For each HRS, the kinematics are shown from left to right in the chronological order.

a shift in the Q^2 value of the measurement and must be incorporated into HAMC. In HAMC, the hit position on the lead-glass detector was calculated from the focal plane coordinates, such that the PID efficiency measured from data can be applied to each simulated event. The efficiency could drift due to electronic module malfunction and drifts in the discriminator thresholds. For most of kinematics, such a drift was gradual and daily calibrations were sufficient to correct for its effect.

In general, the acceptance of the HRS is defined by combining the opening geometry of the intermediate apertures, whose nominal settings were documented in Ref. [53]. The real acceptance however can be different from the nominal settings. The HRS acceptance of the simulation was fine-tuned by matching these appertures to the cross-section-weighted event distributions obtained from data. This process is illustrated in Fig. 14.

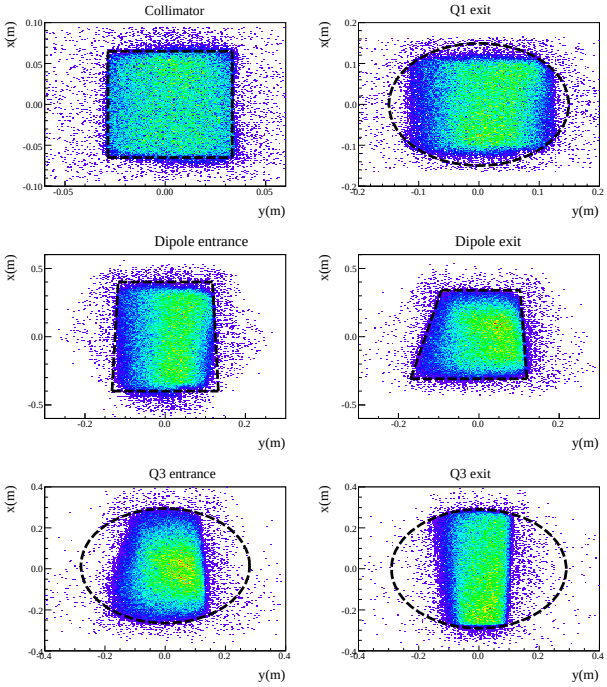

Figure 14: Fine-tuning of the HRS acceptance in HAMC. Event distributions from data are plotted at the collimator (entrance of the HRS Q_1), Q_1 exit, entrances and exits of the dipole, Q_2 and Q_3. From these distribution, the best estimate of the position and the size of the apertures were determined (black dashed lines and curves). These were then used as aperture or acceptance cuts in HAMC. The axes are oriented such that the distributions are as viewed along the particle trajectory, with y the horizontal and x the vertical (dispersive) directions, respectively.

Once all magnet apertures were optimized, the kinematics (Q^2, x) were calculated from HAMC using Eqs. (3,7), the beam energy E (minus 3 MeV as mentioned earlier), and the E' and the scattering angles of the simulated events. Similarly, we calculated the (Q^2, x) values from data using the vertex coordinates $(x_{tg}, y_{tg}, \theta_{tg}, \phi_{tg})$ reconstructed from the detected focal plane variables, based on HRS transport functions. The agreement between the HAMC (Q^2, x) and those reconstructed from the data thus provides a measure of how well we understand the HRS transport function, and should be consistent with the quality of the optics calibration (Table 7). Such agreement also provide an indication of how well the simulation works, which is important for the evaluation of electromagnetic radiative corrections and the effect of PID efficiency on the measurement.

Figure 15 shows comparisons between data and simulation for all target variables, Q^2 and x for Left HRS DIS #1 and Right HRS DIS #2. A summary of the comparison for all kinematics is given in Table 8. The observed differences in Q^2 are consistent with the uncertainties shown in Table 7 for most of the kinematics. For RES III, there is a two-standard-deviation disagreement in Q^2. However, since we interpret the asymmetry results at the measured Q^2, not the simulated value, this disagreement does not affect the final result or its uncertainty evaluation.

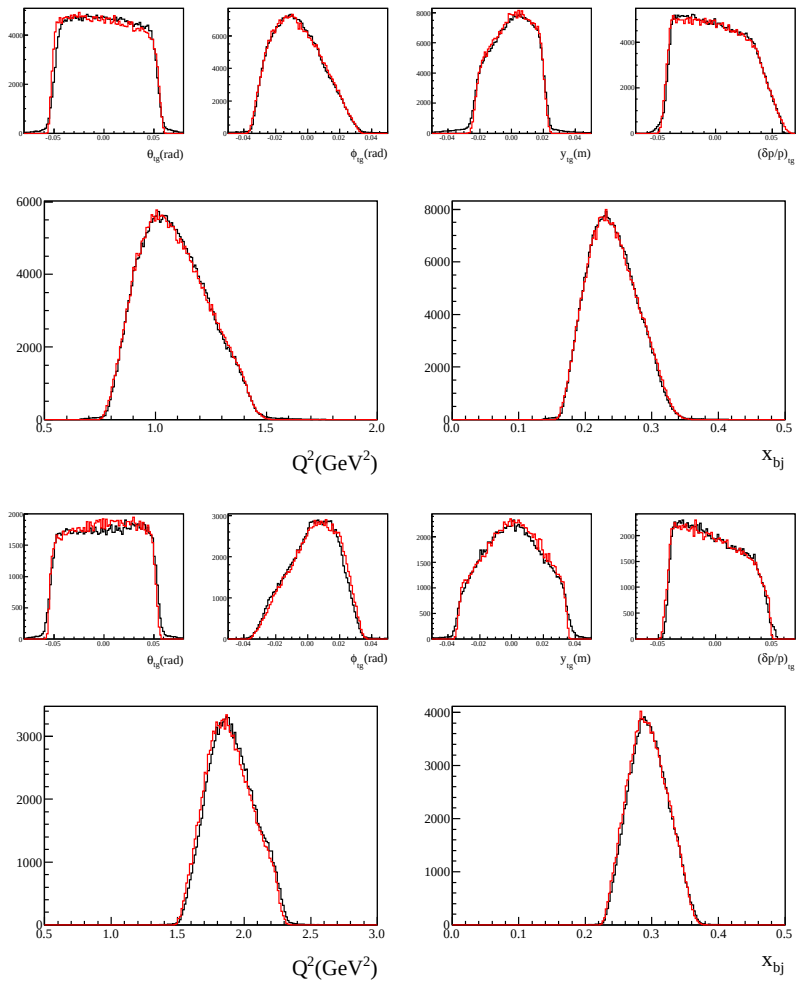

Figure 15: Comparison between HAMC (red) and data (black). From top to bottom: target variables – $\theta_{\rm tg}$, $\phi_{\rm tg}$, $y_{\rm tg}$ and $(\delta p/p)_{\rm tg}$ – for Left HRS DIS#1; Q^2 and x for Left HRS DIS#1; target variables for Right HRS DIS#2; Q^2 and x for Right HRS DIS#2.

Kinematics	HAMC			data			relative difference in Q^2
	$\langle Q^2\rangle$ (GeV/c)^2	$\langle x\rangle$	$\langle W^2\rangle$ GeV^2	$\langle Q^2\rangle$ (GeV/c)^2	$\langle x\rangle$	$\langle W^2\rangle$ GeV^2	
Left HRS DIS#1	1.084	0.241	4.294	1.085	0.241	4.297	$< 0.1\%$
Left+Right HRS DIS#2	1.892	0.294	5.424	1.901	0.295	5.430	0.5%
Left HRS RES I	0.956	0.571	1.600	0.950	0.571	1.595	0.6%
Left HRS RES II	0.832	0.336	2.528	0.831	0.335	2.530	0.1%
Right HRS RES III	0.745	0.225	3.443	0.757	0.228	3.450	1.6%
Left HRS RES IV	1.456	0.324	3.925	1.472	0.326	3.923	1.1%
Left HRS RES V	1.268	0.282	4.109	1.278	0.283	4.122	0.8%

Table 8: Comparison of Q^2, x, and W^2 between HAMC and data for all kinematics. The Left and the Right DIS#2 have been combined. The difference in Q^2 between HAMC and data is smaller than Table 7 for most of the kinematic settings.

3.7. Background Analysis

In this section we analyze all backgrounds that affect the extracted PV electron asymmetry. Assuming each background has an asymmetry A_i and affects the electron sample with a fraction f_i, the correction can be applied as

$$A^{\rm phys} = \frac{\left(\frac{A^{\rm bc,raw}}{P_b} - \sum_i A_i f_i\right)}{1 - \sum_i f_i}\,, \tag{56}$$

where $A^{\rm bc,raw}$ is the measured asymmetry with helicity-dependent beam corrections applied, and P_b is the beam longitudinal polarization presented in section 3.4. When all f_i are small with A_i comparable to or no larger than $A^{\rm bc,raw}$, one can define $\bar{f}_i = f_i(1 - \frac{A_i}{A^{\rm bc,raw}} P_b)$ and approximate

$$A^{\rm phys} \approx \frac{A^{\rm bc,raw}}{P_b} \Pi_i \left(1 + \bar{f}_i\right)\,, \tag{57}$$

i.e., all background corrections can be treated as multiplicative. As can be seen from Eq. (57), the order of the corrections is flexible and the corrections can be applied to the measured asymmetry $A^{\rm bc,raw}$ before normalizing to the beam polarization. The uncertainty of the correction $\bar{f}_i$ causes directly a relative uncertainty on the electron asymmetry

$$\frac{\Delta A_e}{A_e} = \Delta \bar{f}_i. \tag{58}$$

Some effects, such as charged pion and pair-production background, are very small such that corrections [Eq. (57)] are not necessary. For those cases only the uncertainty $\Delta \bar{f}_i$ or $\Delta A_e/A_e$ is presented. The prescription of Eq. (57) was also used for the treatment of the Q^2-uncertainty and radiative corrections (sections 3.6, 3.8 and 3.9).

3.7.1. Charged Pion Background

Charged pions are produced in decays of nucleon resonances created by electron scattering off nucleon or nuclear targets. Simulations have shown that for the pions to have the same momentum as DIS electrons, the parent nucleon resonance must have been produced at a lower Q^2 than DIS events, thus typically cause a smaller parity-violating asymmetry than DIS electrons. This has been confirmed by the asymmetry of the pion triggers measured during the experiment. The charged pion background thus reduces the magnitude of the measured asymmetry, and the effect is the largest if the charged pions did not carry asymmetry at all. Furthermore, the high particle identification performance of the DAQ limited the pion contamination in the electron trigger to the level of $f_{\pi/e} < 2 \times 10^{-4}$ and $< 4 \times 10^{-4}$ for the three DIS kinematics and the five resonance kinematics, respectively [54]. Due to the small contamination, no correction to the measured electron asymmetries was made. The total systematic uncertainty on the measured electron asymmetry due to pion contamination and pion asymmetry is:

$$\left(\frac{\Delta A_e}{A_e}\right)_{\pi^-} = \sqrt{\left(\Delta f_{\pi/e}\right)^2 + \left(f_{\pi/e}\frac{|A_\pi| + \Delta A_\pi}{A_e}\right)^2}\,, \tag{59}$$

where $f_{\pi/e}$ and $\Delta f_{\pi/e}$ are the event fraction of the electron trigger that is from actual pions and its uncertainty, A_π is the measured pion asymmetry with ΔA_π its uncertainty, and A_e is the measured electron asymmetry. The term $|A_\pi| + \Delta A_\pi$ corresponds to how much the pion asymmetry could differ from zero at the 68.3% confidence level. As inputs to the background correction, the extraction of pion asymmetries is described below.

pion asymmetry measurement

The PID performance of both electron and pion triggers of the DAQ was reported in Ref. [54]. To properly extract pion asymmetries from the trigger, one must account for the effect of electron contamination in the pion triggers, $f_{e/\pi}$. Because $f_{e/\pi}$ was relatively high and the electron asymmetries are larger than those of pions, corrections were applied to the asymmetries extracted from the pion triggers using

$$A_\pi^{\rm meas} = \frac{A_{\pi,\rm dit}^{\rm bc,raw} - f_{e/\pi} A_{e,\rm dit}^{\rm bc,raw}}{1 - f_{e/\pi}}\,, \tag{60}$$

where $A_{\pi,\mathrm{dit}}^{\mathrm{bc,raw}}$ and $A_{e,\mathrm{dit}}^{\mathrm{bc,raw}}$ are asymmetries extracted from pion and electron triggers, respectively, with beam corrections applied using the dithering method. Then the measured pion asymmetries are normalized with the beam polarization, giving physics asymmetry results for pion inclusive production:

$$A_\pi^{\mathrm{phys}} = \frac{A_\pi^{\mathrm{meas}}}{P_b} \,. \tag{61}$$

Results for pion asymmetries in the DIS and resonance kinematics are given in Tables 9 and 10. As described in Ref. [54], the narrow-path triggers of the DAQ had smaller counting deadtime than the wide-path triggers, but slightly lower PID performance. As a result the narrow pion triggers had more electron contamination than the wide triggers and requires a larger correction, which causes a larger uncertainty in the extracted pion asymmetry.

HRS, Kinematics	Left DIS#1	Left DIS#2	Right DIS#2
narrow path			
$A_{\pi,\mathrm{dit}}^{\mathrm{bc,raw}} \pm \Delta A_{\pi,\mathrm{dit}}^{\mathrm{bc,raw}}$(stat.) (ppm)	-57.3 ± 8.0	-26.0 ± 14.9	-21.5 ± 4.2
$f_{e/\pi} \pm \Delta f_{e/\pi}$(total)	0.2653 ± 0.0603	0.0331 ± 0.0034	0.0103 ± 0.0013
$A_\pi^{\mathrm{meas}} \pm \Delta A_\pi^{\mathrm{meas}}$ (total) (ppm)	-48.8 ± 14.0	-22.0 ± 21.4	-20.3 ± 6.0
$A_\pi^{\mathrm{phys}} \pm \Delta A_\pi^{\mathrm{phys}}$ (total) (ppm)	-55.3 ± 15.9	-24.6 ± 24.0	-22.9 ± 6.8
wide path			
$A_{\pi,\mathrm{dit}}^{\mathrm{bc,raw}} \pm \Delta A_{\pi,\mathrm{dit}}^{\mathrm{bc,raw}}$(stat.) (ppm)	-49.6 ± 7.7	-27.0 ± 14.9	-21.4 ± 4.2
$f_{e/\pi} \pm \Delta f_{e/\pi}$(total)	0.2176 ± 0.0573	0.0281 ± 0.0037	0.0091 ± 0.0013
$A_\pi^{\mathrm{meas}} \pm \Delta A_\pi^{\mathrm{meas}}$ (total) (ppm)	-41.3 ± 12.8	-23.7 ± 21.4	-20.3 ± 6.0
$A_\pi^{\mathrm{phys}} \pm \Delta A_\pi^{\mathrm{phys}}$ (total) (ppm)	-46.8 ± 14.6	-26.5 ± 24.0	-22.9 ± 6.8

Table 9: For DIS kinematics: beam-corrected pion asymmetries $A_{\pi,\mathrm{dit}}^{\mathrm{bc,raw}}$ with their statistical uncertainties, electron contamination in the pion triggers $f_{e/\pi}$, pion asymmetry results after being corrected for electron contamination A_π^{meas}, and physics asymmetry results for pion inclusive production A_π^{phys}. As described in Ref. [54], the narrow-path triggers had higher electron contamination, thus required a larger correction and had a larger uncertainty in the extracted pion asymmetry.

HRS	Left RES I	Left RES II	Right RES III	Left RES IV	Left RES V
narrow path					
$A_{\pi,\mathrm{dit}}^{\mathrm{bc,raw}} \pm \Delta A_{\pi,\mathrm{dit}}^{\mathrm{bc,raw}}$(stat.) (ppm)	-44.2 ± 40.1	-69.8 ± 26.5	-17.1 ± 8.5	21.8 ± 47.7	-46.7 ± 64.0
$f_{e/\pi} \pm \Delta f_{e/\pi}$(total)	0.4114 ± 0.0201	0.3155 ± 0.0163	0.0849 ± 0.0030	0.1852 ± 0.0073	0.1871 ± 0.0077
$A_\pi^{\mathrm{meas}} \pm \Delta A_\pi^{\mathrm{meas}}$ (total) (ppm)	-33.7 ± 88.6	-73.2 ± 48.8	-13.5 ± 12.7	52.2 ± 76.2	-41.5 ± 102.4
$A_\pi^{\mathrm{phys}} \pm \Delta A_\pi^{\mathrm{phys}}$ (total) (ppm)	-37.3 ± 98.0	-81.0 ± 54.0	-14.9 ± 14.0	58.2 ± 85.0	-46.3 ± 114.2
wide path					
$A_{\pi,\mathrm{dit}}^{\mathrm{bc,raw}} \pm \Delta A_{\pi,\mathrm{dit}}^{\mathrm{bc,raw}}$(stat.) (ppm)	-45.4 ± 39.4	-69.2 ± 26.1	-18.3 ± 8.5	30.9 ± 47.6	-51.0 ± 64.9
$f_{e/\pi} \pm \Delta f_{e/\pi}$(total)	0.3423 ± 0.0231	0.2409 ± 0.0200	0.0633 ± 0.0060	0.1661 ± 0.0080	0.1598 ± 0.0086
$A_\pi^{\mathrm{meas}} \pm \Delta A_\pi^{\mathrm{meas}}$ (total) (ppm)	-39.8 ± 74.9	-71.0 ± 43.7	-15.8 ± 12.4	58.8 ± 74.7	-47.7 ± 101.4
$A_\pi^{\mathrm{phys}} \pm \Delta A_\pi^{\mathrm{phys}}$ (total) (ppm)	-44.0 ± 82.9	-78.5 ± 48.4	-17.5 ± 13.7	65.6 ± 83.3	-53.2 ± 113.1

Table 10: For resonance kinematics: beam-corrected pion asymmetries $A_{\pi,\mathrm{dit}}^{\mathrm{bc,raw}}$ with their statistical uncertainty, electron contamination in the pion triggers $f_{e/\pi}$, pion asymmetry results after being corrected for electron contamination A_π^{meas}, and physics asymmetry results for pion inclusive production A_π^{phys}. As described in Ref. [54], the narrow-path triggers had higher electron contamination, thus required a larger correction and had a larger uncertainty in the extracted pion asymmetry.

electron asymmetry uncertainty due to pion contamination The measured pion and electron asymmetries are listed in Tables 11 and 12 for the two DIS and the five resonance kinematics, respectively, together with the total uncertainty due to pion contamination in the electron asymmetry as calculated with Eq. (59). The values listed for the pion contamination in the electron triggers $f_{\pi/e}$ and the electron contamination in pion triggers $f_{e/\pi}$ and their total uncertainties are from Ref. [54]. The narrow-path triggers have larger uncertainty due to charged pion background because of the

HRS, Kinematics	Left DIS#1	Left DIS#2	Right DIS#2
narrow path			
$A_\pi^{\rm meas} \pm \Delta A_\pi^{\rm meas}$ (total) (ppm)	-48.8 ± 14.0	-22.0 ± 21.4	-20.3 ± 6.0
$A_{e,\rm dit}^{\rm bc,raw} \pm A_{e,\rm dit}^{\rm bc,raw}$ (stat.) (ppm)	-78.5 ± 2.7	-140.3 ± 10.4	-139.8 ± 6.6
$f_{\pi/e} \pm \Delta f_{\pi/e}$ (total) ($\times 10^{-4}$)	(1.07 ± 0.24)	(1.97 ± 0.18)	(1.30 ± 0.10)
$\left(\frac{\Delta A_e}{A_e}\right)_{\pi^-,n}$	0.89×10^{-4}	0.63×10^{-4}	0.27×10^{-4}
wide path			
$A_\pi^{\rm meas} \pm \Delta A_\pi^{\rm meas}$ (total) (ppm)	-41.3 ± 12.8	-23.7 ± 21.4	-20.3 ± 6.0
$A_{e,\rm dit}^{\rm bc,raw} \pm \Delta A_{e,\rm dit}^{\rm bc,raw}$ (stat.) (ppm)	-78.3 ± 2.7	-140.2 ± 10.4	-140.9 ± 6.6
$f_{\pi/e} \pm \Delta f_{\pi/e}$ (total) ($\times 10^{-4}$)	(0.72 ± 0.22)	(1.64 ± 0.17)	(0.92 ± 0.13)
$\left(\frac{\Delta A_e}{A_e}\right)_{\pi^-,w}$	0.54×10^{-4}	0.55×10^{-4}	0.21×10^{-4}

Table 11: For DIS kinematics: pion asymmetry results $A_\pi^{\rm meas}$, beam-corrected electron raw asymmetry $A_e^{\rm bc,raw}$, pion contamination in electron triggers $f_{\pi/e}$, and total uncertainties on the electron asymmetry results due to pion background $(\Delta A_e/A_e)_{\pi^-,n}$ and $(\Delta A_e/A_e)_{\pi^-,w}$, all at the 10^{-4} level.

HRS	Left RES I	Left RES II	Right RES III	Left RES IV	Left RES V
narrow path					
$A_\pi^{\rm meas} \pm \Delta A_\pi^{\rm meas}$ (total) (ppm)	-33.7 ± 88.6	-73.2 ± 48.8	-13.5 ± 12.7	52.2 ± 76.2	-41.5 ± 102.4
$A_{e,\rm dit}^{\rm bc,raw} \pm \Delta A_{e,\rm dit}^{\rm bc,raw}$ (stat.)	-55.1 ± 6.8	-63.8 ± 5.9	-54.4 ± 4.5	-104.0 ± 15.3	-67.9 ± 21.3
$f_{\pi/e} \pm \Delta f_{\pi/e}$ (total) ($\times 10^{-4}$)	(0.79 ± 0.11)	(2.40 ± 0.20)	(3.82 ± 0.23)	(0.26 ± 0.03)	(0.45 ± 0.03)
$\left(\frac{\Delta A_e}{A_e}\right)_{\pi^-,n}$	1.75×10^{-4}	4.60×10^{-4}	1.85×10^{-4}	0.32×10^{-4}	0.96×10^{-4}
wide path					
$A_\pi^{\rm meas} \pm \Delta A_\pi^{\rm meas}$ (total) (ppm)	-39.8 ± 74.9	-71.0 ± 43.7	-15.8 ± 12.4	58.8 ± 74.7	-47.7 ± 101.4
$A_{e,\rm dit}^{\rm bc,raw} \pm \Delta A_{e,\rm dit}^{\rm bc,raw}$ (stat.) (ppm)	-54.6 ± 6.8	-63.9 ± 5.9	-54.0 ± 4.5	-104.6 ± 15.3	-67.9 ± 21.5
$f_{\pi/e} \pm \Delta f_{\pi/e}$ (total) ($\times 10^{-4}$)	(0.54 ± 0.15)	(1.50 ± 0.25)	(2.14 ± 0.48)	(0.22 ± 0.03)	(0.32 ± 0.04)
$\left(\frac{\Delta A_e}{A_e}\right)_{\pi^-,w}$	1.13×10^{-4}	2.71×10^{-4}	1.22×10^{-4}	0.28×10^{-4}	0.71×10^{-4}

Table 12: For resonance kinematics: pion asymmetry results $A_\pi^{\rm meas}$, beam-corrected electron raw asymmetry $A_e^{\rm bc,raw}$, pion contamination in electron triggers $f_{\pi/e}$, and total uncertainties on the electron asymmetry results due to pion background $(\Delta A_e/A_e)_{\pi^-,n}$ and $(\Delta A_e/A_e)_{\pi^-,w}$, all at the 10^{-4} level.

slightly lower pion rejection performance. However, overall the uncertainty due to charged pion background is very low, at the 10^{-4} level for all kinematics.

3.7.2. Pair Production Background

The pair production background results from nucleon resonance production when the resonance decays into neutral pions (π^0) that then decay into e^+e^- pairs. Pair production from bremsstrahlung photons is not significant in the kinematics of this experiment because pair production is highly forward-peaked. Therefore, one expect the effect from pair-production background to be similar to that of charged pions and the prescription of Eq. (59) can be used by replacing A_π with A_{e^+} and $f_{\pi/e}$ with the fractional contribution of pair production to the main electron trigger f_{e^+/e^-}. For the pair-production asymmetry, we expect it to be determined by the π^0 photo- and electroproduction and thus comparable to that of the charged pion asymmetry. The contamination factor f_{e^+/e^-} was determined for the two DIS kinematics by reversing the HRS polarity and measure the rate of positrons from the π^0 decay. Due to the low rate of positron events the HRS DAQ could be used for these studies with the VDC and a well-understood PID. However, the statistical uncertainties in the positron asymmetry were quite large due to the very low positron rate. Moreover, the π^+ contamination in the positron trigger was quite high, estimated to be 11% and 20% for the Left DIS#1 and Right DIS#2, respectively, assuming the PID performance of the detector does not depend on the sign of the particles' charge. The measured asymmetry of the pair-production background could not be corrected for the π^+ contamination due to the lack of knowledge on the π^+ asymmetry.

Asymmetries extracted from positive polarity runs are shown in Table 13 without corrections for the π^+ background or beam polarization.

HRS	Left DIS#1	Right DIS#2
$A^{\rm raw}_{e^+}$ (ppm), narrow	723.2 ± 1154.7(stat.)	1216.0 ± 1304.5(stat.)
$A^{\rm raw}_{e^+}$ (ppm), wide	742.4 ± 1151.5(stat.)	1199.0 ± 1304.5(stat.)

Table 13: Raw positron asymmetry results. No correction for the beam position, energy, and polarization, or the π^+ background was made.

Because the statistical uncertainties in the positron asymmetry are so large, we relied on the fact that π^0 must have similar asymmetries as π^-. We assume the π^0 asymmetry to be no larger than twice that of the π^- asymmetry and estimated the uncertainty in the electron asymmetry due to pair production to be:

$$\left(\frac{\Delta A_e}{A_e}\right)_{\rm pair} = \sqrt{\left(\Delta f_{e^+/e^-}\right)^2 + \left(f_{e^+/e^-}\frac{\Delta A_{e^+}}{A_e}\right)^2}, \tag{62}$$

where ΔA_{e^+} describes how much A_{e^+} differs from zero and the value $2(|A_{\pi^-}| + \Delta A_{\pi^-})$ was used. Results for f_{e^+/e^-} and their statistical uncertainties are shown in Table 14, and a 30% uncertainty was used for $\Delta f_{e^+/e^-}$ to account for possible systematic effects in positron identification due to the high π^+ background in the rate evaluation. Results for the electron asymmetry uncertainty due to pair production background are also shown in Table 14.

HRS	Left DIS#1	Left DIS#2	Right DIS#2
$f_{e^+/e^-} \pm \Delta f_{e^+/e^-}$ (stat.)	$(2.504 \pm 0.007) \times 10^{-4}$	$(5.154 \pm 0.001) \times 10^{-3}$	$(4.804 \pm 0.001) \times 10^{-3}$
$\left(\frac{\Delta A_e}{A_e}\right)_{\rm pair,narrow}$	4.1×10^{-4}	3.5×10^{-3}	2.3×10^{-3}
$\left(\frac{\Delta A_e}{A_e}\right)_{\rm pair,wide}$	3.5×10^{-4}	3.7×10^{-3}	2.3×10^{-3}

Table 14: Results for pair production (positron) contamination in the electron trigger f_{e^+/e^-} and its statistical uncertainty, and the total uncertainty on electron asymmetry due to pair production background, $\left(\frac{\Delta A_e}{A_e}\right)_{\rm pair}$. Only DIS kinematics are shown. The errors shown for f_{e^+/e^-} are statistical only, and a 30% systematic uncertainty on f_{e^+/e^-} was used in the evaluation of $\frac{\Delta A_e}{A_e}$.

There was no measurement for the pair production rate for any resonance kinematics. Based on the fact that the π^-/e rate ratios for resonance settings were similar to DIS #1 and are about one order of magnitude smaller than that of DIS#2 (see Table 3), a conservative estimate of 3×10^{-3} (the average of the uncertainty at DIS#2) was used as the relative uncertainty due to pair production for all resonance asymmetry results.

3.7.3. Target EndCap Corrections

Electrons scattered off the target aluminum endcaps cannot be separated from those scattered off the liquid deuterium. The parity-violating asymmetry from aluminum differs slightly from that of deuterium and a correction must

be made. Based on Eqs. (2-12), the value of parity-violating (PV) asymmetry from $e-$Al scattering was calculated as

$$A_{\rm Al} = \frac{13A_p\sigma_p + 14A_n\sigma_n}{13\sigma_p + 14\sigma_n}\,, \tag{63}$$

where $\sigma_{p(n)}$ is the cross section and $A_{p(n)}$ is the PV asymmetry for scattering off the proton (neutron). The cross sections $\sigma_{p(n)}$ were calculated using a fit to world resonance and DIS data [69]. The asymmetries $A_{p(n)}$ were calculated using Eq. (34):

$$A_p = \left(-\frac{3G_FQ^2}{2\sqrt{2}\pi\alpha}\right)\frac{Y_1\left[2C_{1u}(u^+ + c^+) - C_{1d}(d^+ + s^+)\right] + Y_3\left[2C_{2u}(u^-) - C_{2d}(d^-)\right]}{4(u^+ + c^+) + (d^+ + s^+)}\,, \tag{64}$$

$$A_n = \left(-\frac{3G_FQ^2}{2\sqrt{2}\pi\alpha}\right)\frac{Y_1\left[2C_{1u}(d^+ + c^+) - C_{1d}(u^+ + s^+)\right] + Y_3\left[2C_{2u}(u^-) - C_{2d}(d^-)\right]}{4(d^+ + c^+) + (u^+ + s^+)}\,, \tag{65}$$

with $u^\pm \equiv u \pm \bar{u}$, $d^\pm \equiv d \pm \bar{d}$, $s^+ \equiv s + \bar{s}$ and $c^+ \equiv c + \bar{c}$.

The actual aluminum asymmetries $A_{\rm Al}$ may differ from the values calculated using Eq. (63) due to effects such as resonance structure (for resonance kinematics), and nuclear effects similar to the EMC effect [70, 71] of the unpolarized, parity-conserving structure functions $F_{1,2}$.

For the two DIS kinematics ($x = 0.2 - 0.3$) the EMC effect for Al is approximately 3% [72]. A conservative relative uncertainty of 10% was used for $A_{\rm Al}$ in the DIS kinematics. For resonance kinematics, the EMC effect for Al is in the range $(3-14)\%$, and even larger for higher x values. In addition, the measured electron asymmetry at all five resonance kinematics were found to be in good agreement (at the 10-15% level) with the values calculated using PDFs [49]. We expect that the uncertainty in $A_{\rm Al}$ due to resonance structure cannot exceed this level. Adding the nuclear and the resonance effects in quadrature, a 20% relative uncertainty was used for $A_{\rm Al}$ in the resonance kinematics.

The fractional event rate from the aluminum endcaps, $\alpha_{\rm Al/D}$, was calculated as

$$\alpha_{\rm Al/D} = \eta_{\rm Al/D}R^{\rm EMC}_{\rm Al/D}\frac{(13\sigma_p + 14\sigma_n)/27}{(\sigma_p + \sigma_n)/2} = \eta_{\rm Al/D}R^{\rm EMC}_{\rm Al/D}\frac{26\sigma_p + 28\sigma_n}{27\sigma_p + 27\sigma_n}\,, \tag{66}$$

where $\eta_{\rm Al/D}$ is the ratio of the endcap to liquid deuterium thicknesses, and $R^{\rm EMC}_{\rm Al/D}$ is the Al to deuterium cross-sectional EMC ratio from Ref. [71, 72, 73, 74, 75]. The target used for this experiment had entrance and exit endcaps measured to be $0.126 \pm 0.011 \pm 0.003$ mm and $0.100 \pm 0.008 \pm 0.003$ mm thick, respectively (see Table 2), with the first error bar from the standard deviation of multiple measurements at different positions on the endcap, and the second error from calibration of the instrument. The ratio $\eta_{\rm Al/D}$ is $\eta_{\rm Al/D} = (0.126 + 0.100)$ mm$\times(2.7$ g/cm$^3)/(20$ cm$\times 0.167$ g/cm$^3) = 1.827\%$ with an uncertainty of $\Delta\eta_{\rm Al/D} = 0.115\%$.

The correction to the electron PVDIS asymmetry was applied as

$$A_e^{\rm Al-corrected} = A_e(1 + \bar{f}_{\rm Al}), \tag{67}$$

$$\text{with } \bar{f}_{\rm Al} = -(\alpha_{\rm Al/D})\frac{A_{\rm Al} - A_D}{A_D}. \tag{68}$$

The total uncertainty due to target endcaps is

$$\left(\frac{\Delta A_e}{A_e}\right)_{\rm Al} = \sqrt{\left(\Delta\alpha_{\rm Al/D}\frac{A_{Al} - A_D}{A_D}\right)^2 + \left[(\delta_{A_{\rm Al}})\alpha_{\rm Al/D}\right]^2} \tag{69}$$

where $\alpha_{\rm Al/D}$ is from Eq. (66), $\Delta\alpha_{\rm Al/D} = (\Delta\eta_{\rm Al/D}/\eta_{\rm Al/D})\alpha_{\rm Al/D} = 0.063\alpha_{\rm Al/D}$, $A_{\rm Al}$ from Eqs.(63-65), A_D from Eq. (32, and $\delta_{A_{\rm Al}}$ is the maximal relative difference in the Al vs. D_2 PV asymmetries caused by an EMC-like medium modification effect and resonance structures. As stated above, the values $\delta_{A_{\rm Al}} = 10\%$ for DIS and $= 20\%$ for resonance kinematics were used. Results for the endcap correction $\bar{f}_{\rm Al}$ and the uncertainty on the corrected electron asymmetry are listed in Table 15.

Events were also taken on a thick, "dummy" target consisting of two aluminum foils with their thickness approximately 10 times that of the liquid deuterium cell. The thickness was chosen such that the total radiation length of the dummy target matches that of the liquid D_2 target. However, due to limited beam time, the asymmetry uncertainty collected from the aluminum dummy target was not precise enough to reduce the systematic uncertainty due to target endcaps.

Kinematics	DIS#1	DIS#2	RES I	RES II	RES III	RES IV	RES V
$(A_{\rm Al} - A_D)/A_D$	0.567%	0.727%	1.335%	0.800	0.510	0.799	0.691
$\alpha_{\rm Al/D}$	2.02%	2.02%	2.01%	2.02%	2.02%	2.02%	2.02%
$\bar{f}_{\rm Al}$ $(\times 10^{-4})$	-1.146	-1.467	-2.687	-1.617	-1.033	-1.613	-1.395
$(\Delta A_e/A_e)_{\rm Al}$	0.239%	0.239%	0.422%	0.424%	0.424%	0.423%	0.424%

Table 15: Target endcap correction for all kinematics. Shown here are the relative differences between calculated Al and D_2 asymmetries, $(A_{\rm Al} - A_D)/A_D$, the fractional event rate from Al endcaps $\alpha_{\rm Al/D}$, corrections applied to measured electron asymmetries $\bar{f}_{\rm Al}$ using Eq. (68), and the relative uncertainty in the corrected electron asymmetry due to endcap corrections $(\Delta A_e/A_e)_{\rm Al}$ using Eq. (69).

3.7.4. Beam Transverse Asymmetry Correction

Transverse asymmetry background, also called the beam normal asymmetry background, describes the effect of the electron beam spin polarized in the direction normal to the scattering plane defined by the momentum vectors of the incident and the scattered electrons $\vec{k}_e$ and $\vec{k}'_e$ [76]. This beam normal asymmetry is parity-conserving and must be treated as a background of the measurement. Calculations at the pure partonic level show that this asymmetry is between 0.1-0.2 ppm at the kinematics of this experiment, but mechanisms beyond the parton level can enhance the asymmetry by 1-2 orders of magnitude [77]. The contribution from the beam normal asymmetry A_n to the measured asymmetry can be expressed as

$$\delta A = (A_n)\vec{S}\cdot\hat{k}_n \quad \text{with} \quad \vec{k}_n \equiv \hat{k}_e \times \hat{k}'_e \ \text{ and } \hat{k}_n = \vec{k}_n/|\vec{k}_n| \,, \tag{70}$$

where A_n is the beam-normal asymmetry and $\vec{S}$ is the beam polarization vector. Denoting θ_0 the central scattering angle of the spectrometer and θ_{tr} the vertical angle of the scattered electron w.r.t. the nominal setting of the spectrometer (see Fig. 16), one has $\hat{k}_e = (0,0,1)$ and $\hat{k}'_e = (\sin\theta_0\cos\theta_{tr}, \sin\theta_0\sin\theta_{tr}, \cos\theta_0)$, giving $\vec{k}_n = (-\sin\theta_0\sin\theta_{tr}, \sin\theta_0\cos\theta_{tr}, 0)$ and $\hat{k}_n = (-\sin\theta_{tr}, \cos\theta_{tr}, 0)$, thus

$$\delta A \;\; = \;\; A_n\left[-S_H\sin\theta_{tr} + S_V\cos\theta_{tr}\right] \,, \tag{71}$$

where $S_{V,H,L}$ are respectively the electron polarization components in the vertical (perpendicular to the nominal scattering plane defined by the electron beam and the central ray of the spectrometer), horizontal (within the nominal plane but transverse to the beam), and longitudinal directions. The value of S_L is thus the beam longitudinal polarization P_b. During the experiment the beam spin components were controlled to $|S_H/S_L| \leqslant 27.4\%$ and $|S_V/S_L| \leqslant 2.5\%$ and the average value of θ_{tr} was found from data to be less than 0.01 rad. Therefore the beam vertical spin dominates this background:

$$(\Delta A_e)_{A_n} \approx A_n S_V\cos\theta_{tr} \approx A_n S_V \leqslant (2.5\%)P_b A_n \,. \tag{72}$$

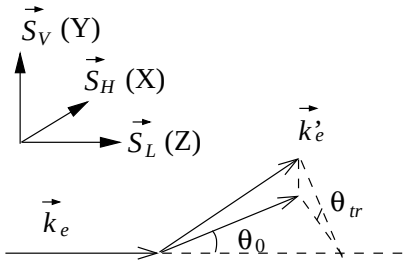

Figure 16: Kinematics of the beam normal asymmetry background. The incident and the scattered electrons' momenta are $\vec{k}_e$ and $\vec{k}'_e$, and $\vec{S}_{V,H,L}$ denote respectively the incident electron's spin polarization components in the vertical, horizontal, and longitudinal directions. The central scattering angle setting of the spectrometer is θ_0 and the scattered electron's momentum has an out-of-plane angle denoted by θ_{tr}.

During the experiment, the size of the beam normal asymmetry A_n was measured for DIS kinematics during dedicated "transverse runs" where the beam was fully polarized in the vertical direction, $S_H^T = S_L^T \approx 0$ and $S_V = P_{b0}^T$ where the superscript T stands for transverse asymmetry measurement and P_{b0}^T is the maximum beam polarization during such measurement. Asymmetries measured during these runs are thus $A_n^{\rm meas} = A_n P_{b0}^T$. Because

Since the maximum beam polarization is the same for production and transverse asymmetry running, one has $P_{b0}^T = S_0 \equiv \sqrt{S_L^2 + S_V^2 + S_H^2} = \sqrt{1 + (0.274)^2 + (0.025)^2} S_L = 1.037 S_L$ and the total uncertainty in the electron asymmetry can be calculated as

$$\left(\frac{\Delta A_e}{A_e}\right)_{A_n} = \frac{A_n S_V}{A_e^{\rm meas}} = \frac{(A_n^{\rm meas}/S_0) S_V}{A_e^{\rm meas}} = \frac{A_n^{\rm meas}}{A_e^{\rm meas}} \frac{S_V}{S_0} \leqslant 2.4\% \frac{A_n^{\rm meas}}{A_e^{\rm meas}} \, . \tag{73}$$

For DIS kinematics, we denote $\delta A_n^{\rm meas}$ as how much A_n could differ from zero to account for the uncertainty of the A_n measurement, and write

$$\left(\frac{\Delta A_e}{A_e}\right)_{A_n,{\rm DIS}} \leqslant 2.4\% \frac{\delta A_n^{\rm meas}}{A_e^{\rm meas}} \, . \tag{74}$$

If the measured A_n is consistent with zero, the statistical uncertainty of the measurement $\Delta A_n^{\rm meas}$(stat.) is taken as $\delta A_n^{\rm meas}$, otherwise the value of $(|A_n^{\rm meas}| + \Delta A_n^{\rm meas})$ is used as $\delta A_n^{\rm meas}$.

Results for the beam transverse asymmetry measurements are shown in Table 16 for the two DIS kinematics along with the resulting uncertainty on the electron PVDIS asymmetry due to beam transverse polarizations.

Kinematics	Left DIS#1	Right DIS#2
Q^2 (GeV/c)^2	1.085	1.907
$A_n^{\rm meas} \pm \Delta A_n^{\rm meas}$ (stat.) (ppm, narrow)	-24.15 ± 15.05	23.49 ± 44.91
$A_e^{\rm meas}$ (ppm, narrow)	78.45	-139.97
$\left(\frac{\Delta A_e}{A_e}\right)_{A_n,\ \rm narrow}$	1.18%	0.76%
$A_n^{\rm meas} \pm \Delta A_n^{\rm meas}$ (stat.) (ppm, wide)	-24.66 ± 15.01	24.60 ± 44.90
$A_e^{\rm meas}$ (ppm, wide)	78.27	-140.67
$\left(\frac{\Delta A_e}{A_e}\right)_{A_n,\ \rm wide}$	1.20%	0.76%

Table 16: The measured beam transverse asymmetry together with the resulting uncertainty on the electron asymmetry. The dithering-corrected values were used for both $A_e^{\rm meas}$ and $A_n^{\rm meas}$. For DIS#2, the electron asymmetry is the combined value from the Left and the Right HRS.

Beam transverse asymmetry measurements were not performed for the resonance kinematics. However, A_n measured in the DIS region has a similar Q^2 dependence and magnitude as that measured in previous elastic electron scattering from the proton and heavier nuclei [76]. This indicates the size of A_n to be determined predominantly by Q^2, and that the response of the target (elastic vs. DIS) only affects A_n at higher order. Based on this observation, we used Ref. [76] to calculate A_n for all resonance kinematics and found it between -38 and -80 ppm depending on the value of Q^2, and are always smaller than that of the electron asymmetry. The uncertainty due to A_n was estimated in resonance kinematics as

$$\left(\frac{\Delta A_e}{A_e}\right)_{A_n,{\rm RES}} \approx |\frac{A_n S_V}{A_e^{\rm meas}}| = |\frac{S_V A_n}{P_b A_e^{\rm phys}}| \leqslant |S_V/P_b| = |S_V/S_L| = 2.5\% \, . \tag{75}$$

3.7.5. Target Purity, Density Fluctuation and Other False Asymmetries

The liquid deuterium used contained [78] 1889 ppm HD, < 100 ppm H_2, 4.4 ppm N_2, 0.7 ppm O_2, 1.5 ppm CO, < 1 ppm methane and 0.9 ppm CO_2. The only non-negligible effect on the measured asymmetry comes from the proton in HD. Since the proton asymmetry as given by Eq. (64) differs from the asymmetry of the deuteron by no more than $\pm(15-30)\%$, the proton in HD contributes an uncertainty of less than $(\Delta A_e/A_e)_{\rm HD} < 0.06\%$ to the measured electron asymmetry.

3.7.6. Rescattering and Poletip Scattering Background

In this section, two kinds of backgrounds from rescattering inside the HRS spectrometers are considered. The first is due to electrons from outside the $\pm$4% momentum acceptance which rescatter into the detector and have a different asymmetry since $A \propto Q^2$. The second effect is called "poletip scattering", which refers to electrons which scattered from polarized electrons (Møller scattering) in the magnetized iron in the HRS dipoles. These backgrounds

are suppressed by a factor of 10 compared to the estimates given in Ref. [19], because of our trigger threshold for the lead-glass detector.

For both of these backgrounds, the correction to our asymmetry can be written as

$$A^{rs-corrected} = A^{meas}\left(1 - \frac{f\Delta A}{A_{meas}}\right) , \tag{76}$$

where $A^{rs-corrected}$ is the corrected asymmetry, A^{meas} is the measured asymmetry, f is the fraction of the rescattering background, $\Delta A = A^{bgr} - A^{meas}$ is the difference between the background's asymmetry and the measured asymmetry, and the approximation is valid if $f \ll 1$. The correction can be evaluated by integrating over the energy that contribute to this background:

$$f\Delta A = \frac{1}{\Delta E_{HRS}} \int_{outside} dE \frac{P_{rs}(E) P_{thr} \left(\frac{d\sigma}{d\Omega dE}\right)_{outside} (A^{bgr} - A^{meas})}{\left(\frac{d\sigma}{d\Omega dE}\right)_{inside}} \tag{77}$$

where ΔE_{HRS} is the HRS energy acceptance, P_{rs} is the rescattering probability that describes the relative contribution of rescattered events among all events that reach the detectors, P_{thr} is the probability for rescattered events that reach the detectors to pass the trigger threshold and cause an electron trigger, A^{bgr} is the asymmetry of the background, $\left(\frac{d\sigma}{d\Omega dE}\right)_{inside(outside)}$ is the scattering cross section inside (outside) the HRS acceptance. The integration is done from just outside the spectrometer acceptance (beyond $\pm 4\%$) to up to $\pm 20\%$ of the nominal setting E_0'. The upper limit of 20% is used because the function $P_{rs}(E)$ becomes negligible beyond this range.

The rescattering probability $P_{rs}(E)$ was measured by the HAPPEx experiment [19], and the results are shown in Fig. 17. The probability drops to below 10^{-3} just outside the HRS acceptance (4%) and quickly to 10^{-6} at 20%. Although only the positive detune ($\delta p/p > 0$) was measured, we assumed the distribution is symmetric around the nominal momentum of the spectrometer.

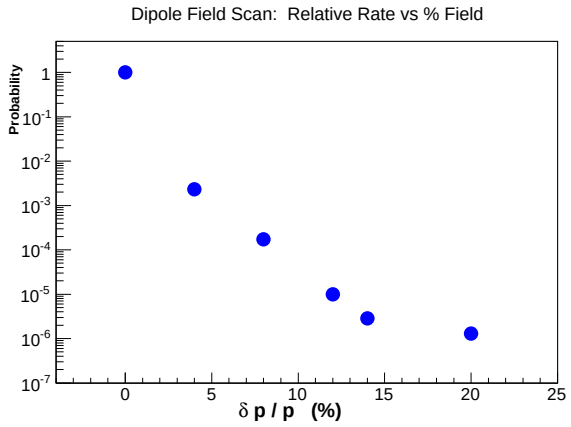

Figure 17: The function $P_{rs}(E)$ determined from HAPPEx data.

The trigger threshold factor $P_{thr} \approx 0.1$ is estimated from the location of the trigger threshold for our leadglass calorimater. The parity-violating asymmetry scales with Q^2 and we find that $\frac{(f\Delta A)_{rs}}{A^{meas}} \ll 2 \times 10^{-5}$.

In Ref. [19] an upper bound for the poletip scattering effect was found. Using that analysis, and without accounting for the further suppression by our trigger thresholds, we estimate that

$$\frac{(f\Delta A)_{pole-tip}}{A^{meas}} < \frac{0.3\, ppm}{A^{meas}} . \tag{78}$$

Because the effects from rescattering and pole-tip scattering are both small, no correction to the asymmetry was made and the these two effects were counted as additional systematic uncertainties.

3.8. Electromagnetic Radiative Correction

Electrons undergo radiative energy losses due to interactions such as internal and external bremsstrahlung and ionization loss, both before and after the scattering. This causes two effects on the measurement: 1) There is a small beam depolarization effect associated with the energy loss of incident electrons; 2) the energy loss of both incident and scattered electrons would cause a difference between the kinematics reconstructed from the detected signals and what really happened at the interaction point. We discuss these two effects separately.

3.8.1. Beam Depolarization Effect in Bremstralung

The depolarization of electron from bremstralung radiation was calculated based on Ref. [79] and the formalism is provided in Appendix A. We define a depolarization correction

$$f_{\rm depol} = \frac{\langle A_e D \rangle}{\langle A_e \rangle} \tag{79}$$

where D is the beam depolarization factor (with zero depolarization corresponding to $D = 100\%$) and the average of a quantity $\langle a \rangle$ ($a = A_e$ or $A_e D$) is taken over the spectrometer acceptance and the cross section σ:

$$\langle a \rangle \equiv \frac{\int a \cdot \sigma \cdot (\text{acceptance})}{\int \sigma \cdot (\text{acceptance})} \, . \tag{80}$$

The measured asymmetry should be corrected as

$$A^{\rm depol-corrected} = A_e^{\rm meas}(1 + \bar{f}_{\rm depol}) \, , \tag{81}$$

where $\bar{f}_{\rm depol} \equiv (1/f_{\rm depol}) - 1 \approx \langle A_e \rangle / \langle A_e D \rangle - 1$. An HAMC simulation was done to determine the value of $\bar{f}_{\rm depol}$ and the results are shown in Table 17.

Kinematics	DIS#1	DIS#2	RES I	RES II	RES III	RES IV	RES V
$f_{\rm depol}$	0.096%	0.209%	0.005%	0.028%	0.093%	0.061%	0.081%

Table 17: Beam depolarization correction $\bar{f}_{\rm depol}$ for all kinematics.

3.8.2. Corrections for Vertex versus Detected Kinematics

Due to energy losses of the electrons, the kinematics at the interaction vertex is not the same as those calculated from the initial beam energy and the electron's momentum detected by the spectrometer. This effect is illustrated in Fig. 18: since the shift between detected and vertex kinematics relies heavily on the experimental setup, it is desired to correct

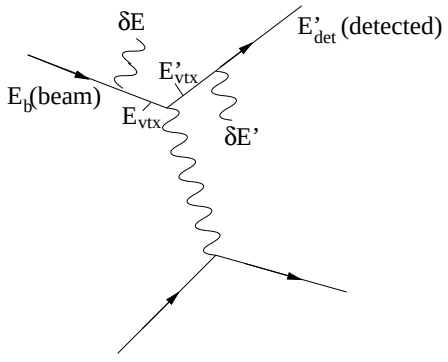

Figure 18: Kinematics used in HAMC to correct energy losses δE and $\delta E'$ for the incoming and outgoing electrons respectively. The kinematics reconstructed from the data corresponds to $E_{\rm beam}$ and $E'_{\rm det}$, while the vertex kinematics corresponds to $E_{\rm vtx}$ and $E'_{\rm vtx}$.

the measured asymmetry for this effect such that the corrected values can be compared to theoretical expectations in an unambiguous way. This correction factor is defined as:

$$1 + \bar{f}_{\rm rc} \quad = \quad \frac{A(\langle Q^2_{\rm det}\rangle, \langle x_{\rm det}\rangle)}{\langle A(Q^2_{\rm vtx}, x_{\rm vtx})\rangle} \ , \tag{82}$$

and is applied to the measured asymmetry as:

$$A_e^{\rm rad-corrected} = A_e^{\rm meas}(1 + \bar{f}_{rc}) \ . \tag{83}$$

Here $A(\langle Q^2_{\rm det}\rangle, \langle x_{\rm det}\rangle)$ is the asymmetry calculated at the cross-section- and acceptance-weighted values [see Eq. (80)] of $Q^2_{\rm det}$ and $x_{\rm det}$, evaluated from the initial beam energy and the detected electrons momentum, and $\langle A(Q^2_{\rm vtx}, x_{\rm vtx})\rangle$ is the asymmetry still averaged over all detected electrons following Eq. (80), but now calculated using the vertex kinematics $Q^2_{\rm vtx}$ and $x_{\rm vtx}$ of each event. Since the value $\langle A(Q^2_{\rm vtx}, x^2_{\rm vtx})\rangle$ is the expected value of what was actually measured in the experiment ($A_e^{\rm meas}$), the result $A_e^{\rm rad-corrected}$ can be treated as the value correponding to $\langle Q^2_{\rm det}\rangle$ and $\langle x_{\rm det}\rangle$. The value of $A_e^{\rm rad-corrected}$ can thus be compared with theoretical calculations evaluated at $\langle Q^2_{\rm det}\rangle$ and $\langle x_{\rm det}\rangle$ to extract physics results.

The radiative correction was evaluated using HAMC which calculates both the numerator and the denominator of Eq. (82). Therefore, we expect that any small imperfection in the understanding of the HRS acceptance or cross-section calculation, such as that indicated by the 2 standard-deviation disagreement in Q^2 between HAMC and data for RES III, would cancel out to the first order, and does not lead to a larger uncertainty in the radiative correction for this kinematics. The treatment of radiative effects was based on the prescription of Mo & Tsai [80]. The detailed procedure is described below.

For each simulated event, the scattering angle θ and the momentum of the scattered electron $E'_{\rm vtx}$ at the vertex were generated randomly. The energy loss of incoming and outgoing electrons δE and $\delta E'$ were then calculated using the formula given on page 5-7 of Ref. [81], which includes external bremstralung, internal bremstralung using the effective radiator formula, and ionization loss. Next, the incoming electron's energy at the vertex is calculated as $E_{\rm vtx} = E_b - \delta E$ where E_b is the (fixed) initial beam energy and the detected momentum of the scattered electron calculated as $E'_{\rm det} = E'_{\rm vtx} - \delta E'$. If θ and $E'_{\rm det}$ falled within the spectrometer acceptance, the cross section and the PV asymmetry were calculated using both the detected (E_b, E_{det}, θ) and the vertex kinematics $(E_{\rm vtx}, E'_{\rm vtx}, \theta)$ and were stored.

The vertex kinematics $(Q^2_{\rm vtx}, W_{\rm vtx})$ calculated using $(E_{\rm vtx}, \theta, E'_{\rm vtx})$ is shown in Fig. 19 for the two DIS kinematics. One can see that the vertex kinematics of an event could fall into one of the following categories: e-^{2}H elastic ($W < M$ with M the proton mass, quasi-elastic ($W \approx M$), nucleon resonances ($M \lesssim W < 2$ GeV), and DIS ($W > 2$ GeV). To evaluate the PV asymmetries for different vertex kinematics, the following prescription was used:

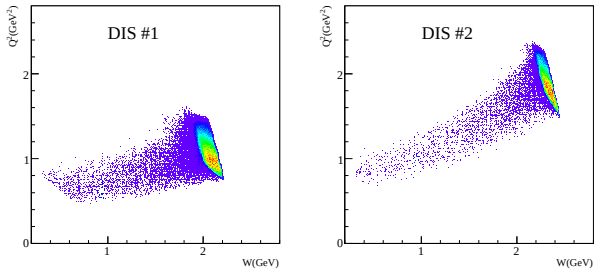

Figure 19: Simulated vertex kinematics of the two DIS kinematics #1 (left) and #2 (right).

1. For $e-^2$H elastic scattering, the method from the SAMPLE experiment [14] was used, where the cross section was based on Ref. [82] and the PV asymmetry was based on a simple model that compares well to the calculation of Ref. [83]. The strange magnetic form factor G_M^s in this method was taken to be zero.
2. For quasi-elastic scattering, the cross section and the asymmetry were calculated using the elastic scattering formula and elastic form factors for the neutron and the proton [see Section VII of Ref. [19]], then smeared for their Fermi motion following the algorithm of Ref. [69]. The quasi-elastic PV asymmetry was then calculated

as $A_d^{\rm qe} = (A_p\sigma_p + A_n\sigma_n)/(\sigma_p + \sigma_n)$ where $A_{p(n)}, \sigma_{p(n)}$ are the elastic asymmetries and cross sections for the proton (neutron), respectively.

3. For the nucleon resonance region ($1 \lesssim W < 2$ GeV), the cross section was based on Ref. [69], and the asymmetries were calculated from three models: one theoretical model on only the $\Delta(1232)$ [84], a second theoretical model that covers almost the whole resonance region [85], and one "cross-section-scaling model" where $A_{\rm res} = \frac{\sigma_{\rm res}}{\sigma_{\rm dis}} A_{\rm dis}$ was used. Here $A_{\rm dis}$ was calculated from Eq. (2) with MSTW2008 PDFs [52], $\sigma_{\rm dis}$ was calculated using the NMC fit of F_2 [86] structure functions and R from Ref. [69], and $\sigma_{\rm res}$ was from Ref. [69] which exhibits distinct resonance structures; The cross-section-scaling model was used only when the theoretical models do not cover the kinematics of a particular event.
4. For DIS ($W > 2$ GeV), the cross section was calculated using Bosted's fits [69] and the PV asymmetry was calculated using Eqs. (2-6), the MSTW2008 PDFs [52] and the quark-parton model formula Eqs. (12,15,16,17). For R in Eq. (15) again Ref. [69] was used.

The physics inputs to HAMC for $e-^2$H elastic, quasi-elastic, DIS, as well as the cross sections were all based on existing data and the uncertainties are small. The uncertainty of the correction was thus dominated by that from the resonance asymmetry models. The validity of these models were evaluated by comparing the measured asymmetries from the resonance kinematics, RES I through IV, with calculations from these models. The kinematic coverage of resonance measurements is shown in Fig. 20. These resonance asymmetries were reported in Ref. [49], and it was

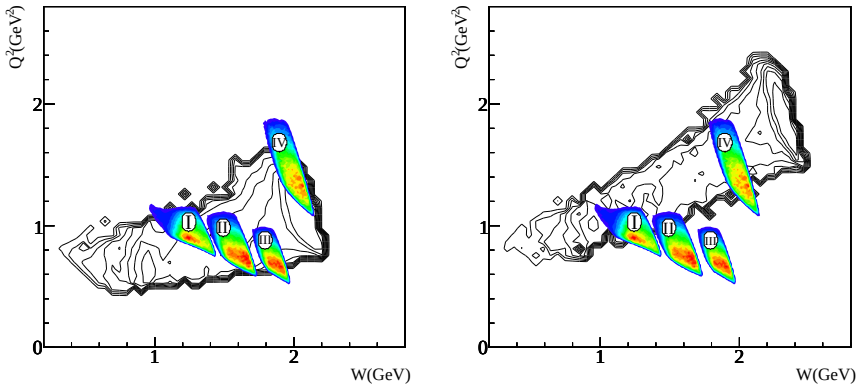

Figure 20: Kinematics coverage of the four resonance measurements (colored contours), together with the DIS kinematics (black contours).

found that the data agree well with both resonance models [84, 85] except RES I. Results at RES I agreed with the two models at the two standard deviation level. The uncertainty from the resonance models was taken to be either the observed difference between resonance data and model, or the statistical uncertainty of the resonance asymmetry measurement, whichever is larger. This gives different model uncertainties as follows:

- For $W^2 < 1.96$ (GeV)^2 or the $\Delta(1232)$ region: RES I locates primarily in this region. The observed 25% relative discrepancy between RES I data and the calculation was used as the model uncertainty in this region;
- For $1.96 < W^2 < 3.0$ (GeV)^2: RES II locates primarily in this region. Since the RES II asymmetry result agreed well with both models, the 10.0% relative statistical uncertainty of the RES II asymmetry was used as the model uncertainty in this region.
- For $3.0 < W^2 < 4.0$ (GeV)^2: Both RES III and IV locate in this region. Since the agreement with the calculations was well within the statistical uncertainties, the relative uncertainties for RES III and IV (8.9% and 15.4% respectively) were combined, and the resulting value of 7.7% was used as the model uncertainty in this region.

For radiative corrections at DIS kinematics, the resonance models affect the denominator, but not the numerator of Eq. (82). Therefore the above model uncertainty affects directly the DIS corrections. These uncertainties were combined with the fractional events whose vertices fell within the corresponding W region to estimate the uncertainty on $\langle A(Q^2_{\rm vtx}, x_{\rm vtx})\rangle$ and $\bar{f}_{\rm rc}$. For radiative corrections at resonance kinematics, the resonance models affect both the

denominator and the numcerator of Eq. (82). The uncertainty of the model itself therefore cancels out in principle in the correction factor $\bar{f}_{\rm rc}$. For resonance kinematics, a conservative 20% relative uncertainty was assigned to the value of $\bar{f}_{\rm rc}$.

The radiative correction factor $1+\bar{f}_{rc}$ obtained from the above procedure is shown in Table 18 for the two models separately. The average value of the two models were applied to the measured asymmetries of this experiment.

Kinematics	Resonance Models used	$A(\langle Q^2_{\rm det}\rangle, \langle x^2_{\rm det}\rangle)$ ppm	$\langle A(Q^2_{\rm vtx}, x^2_{\rm vtx})\rangle$ ppm	$1+f_{rc}$	$1+f_{rc}$ average
DIS #1	Ref. [84]	-88.6	-86.8	1.021 ± 0.020	1.015 ± 0.021
	Ref.[85]	-88.6	-87.8	1.009 ± 0.020	
DIS #2	Ref. [84]	-159.6	-156.6	1.019 ± 0.004	1.019 ± 0.0043
	Ref.[85]	-159.6	-156.7	1.019 ± 0.004	
RES I	Ref. [84]	-93.4	-82.2	1.137 ± 0.027	1.1095 ± 0.0352
	Ref.[85]	-89.0	-82.2	1.082 ± 0.016	
RES II	Ref. [84]	-65.5	-65.5	1.0002 ± 0.0000	1.0205 ± 0.0207
	Ref.[85]	-71.1	-68.3	1.0408 ± 0.0082	
RES III	Ref. [84]	-58.6	-59.1	0.9930 ± 0.0014	1.0005 ± 0.0076
	Ref.[85]	-62.5	-62.0	1.0079 ± 0.0016	
RES IV	Ref. [84]	-117.5	-116.7	1.0063 ± 0.0013	1.0170 ± 0.0112
	Ref.[85]	-123.7	-120.4	1.0276 ± 0.0055	
RES V	Ref. [84]	-103.9	-101.4	1.0241 ± 0.0048	1.0134 ± 0.0110
	Ref.[85]	-103.9	-103.6	1.0027 ± 0.0005	

Table 18: Radiative correction factors. For each kinematics, the simulated asymmetries using two resonance models are shown. In kinematic regions where the resonance models are not available, the cross-section-scaling model was used. These asymmetries were input to Eq. (82) to obtain the radiative correction factors. Results from the two models were averaged to provide the final correction $1+\bar{f}_{rc}$, and the difference between the two was combined with uncertainties of resonance models themselves to provide the total uncertainty on $\bar{f}_{rc}$.

3.9. Box Diagram Corrections

Box diagram corrections refer to effects that arise when the electron simultaneously exchanges two bosons ($\gamma\gamma$, γZ, or ZZ box) with the target, and are dominated by the $\gamma\gamma$ and the γZ box diagrams. For PVES asymmetries, the box diagram effects include those from the interference between Z-exchange and the $\gamma\gamma$ box, the interference between γ-exchange and the γZ box, and the effect of the $\gamma\gamma$ box on the electromagnetic cross sections. It is expected that there is at least partial cancellation among these three terms. The box-diagram corrections were applied as

$$A^{\rm box-corrected} \;=\; (1+\bar{f}_{\rm box})A_e^{\rm meas}\,. \tag{84}$$

Corrections for the $\gamma\gamma$ box effect to the measured electron asymmetry were estimated to be $\bar{f}_{\gamma\gamma{\rm box}} = -0.002$ and -0.003 for DIS #1 and #2, respectively. The effect of the γZ box for DIS kinematics was treated separately as part of the electroweak radiative corrections and will be described in Sec. 4.4.1 [Eqs. (85-88)]. For resonance kinematics, the combined corrections for $\gamma\gamma$ and γZ boxes (i.e. the full box correction) were estimated to be $\bar{f}_{\gamma\gamma,\gamma Z{\rm boxes}} = +0.005$. A relative 100% uncertainty was used for all box-diagram corrections.

4. Results

4.1. Asymmetry results for both DIS and resonance settings

Table 19 presents the measured asymmetries along with their kinematics, all corrections, and the final physics asymmetry results. The x and Q^2 values were obtained from the data and therefore were weighted by the scattering cross section. The dithering-corrected asymmetries were used as $A^{\rm bc,raw}$ and the difference between dithering and regression methods were used as the systematic uncertainty of $A^{\rm bc,raw}$ (see Table 5). In addition to the corrections and uncertainties presented in Sections 3.5 through 3.9, deadtime corrections from Ref. [54] were also applied to the asymmetries. We chose asymmetries measured by the narrow triggers of the DAQ as $A^{\rm bc,raw}$ because of the smaller counting deadtime and the associated uncertainty. All corrections were applied using Eq. (57). The largest corrections

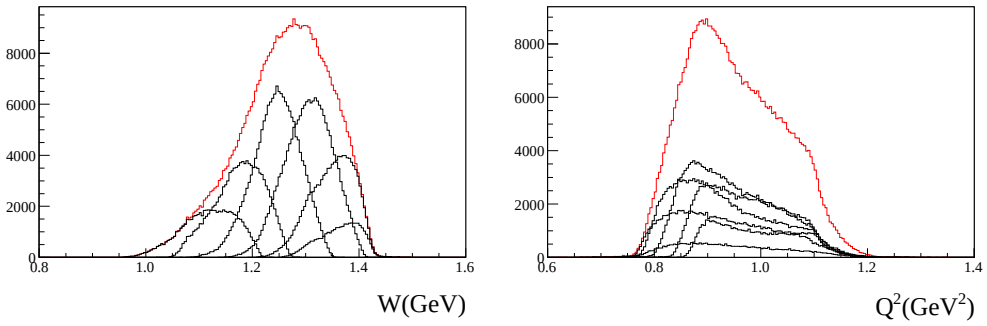

Figure 21: Event distributions in W (left) and Q^2 (right) for the six DAQ groups taken at setting RES I. The coverage in W increases monotonously from group 1 to 6. The red (the highest) histogram shows the global trigger events.

are due to beam polarization, DAQ deadtime, and electromagneic radiative corrections. The largest uncertainties come from the beam normal asymmetry and determination of the Q^2 values. We also note that the pair-production background, though very small for the present experiment, causes an uncertainty typically one order of magnitude larger than that from the charged pion background because one cannot reject pair-production background with PID detectors.

4.2. Group trigger asymmetry results for resonance kinematics

The asymmetry data taken in the resonance region were of particular value: first, they provided the first PVES asymmetries over the complete nucleon resonance region; secondly, they can be used to provide the first test of quark-hadron duality for electroweak observables. For nucleon resonance study, fine-binning in W is often desired, since it may provide detailed resonance structure.

As described in Ref. [54], in addition to the so-called global electron triggers that lead to the main results presented in the previous section, the detector package was divided into groups, for which group electron triggers were constructed, and data recorded in the same way as global triggers. Setting RES I, II and IV on the left HRS had six groups, while setting RES III on the right HRS had eight groups. The kinematics coverage varies between group triggers, providing different coverage in W. Figure 21 shows the Q^2 and the W coverage of all six groups for setting RES I. As one can see, the Q^2 coverage is similar but the W coverages of the six groups are different.

Although approximately (10-20)% events were recorded by two adjacent groups and the group trigger events were not completely uncorrelated, asymmetries extracted for individual groups allowed a study of the W-dependence of the asymmetry. Corrections to the raw asymmetry from group triggers were applied in the same manner presented in the previous section. Among all corrections, two corrections were expected to vary among groups to an observable level, and must be evaluated carefully for individual groups: deadtime (rate-dependent) and electromagnetic radiative corrections (kinematic-dependent). All other corrections either do not depend on groups, or their kinematic variation is expected to be well below the statistical uncertainty of the measurement.

Tables 20 and 21 show respectively for the left and the right HRS: the average kinematics $\langle W \rangle$ and $\langle Q^2 \rangle$, the raw measured asymmetries, the two group-dependent corrections for individual groups, and the physics asymmetry results. Corrections and uncertainties that do not depend on groups are the same as in Table 19. Similar to DIS results, we used the dithering-corrected asymmetries measured from the narrow path triggers of the DAQ as raw-asymmetry inputs to the analysis because the narrow path had smaller counting deadtime and associated uncertainties.

4.3. Test of quark-hadron duality using resonance PV asymmetries

Figure 22 shows the W-dependence of the group-trigger resonance asymmetry results $A_{PV}^{\rm phys}$ of Tables 20 and 21, scaled by $1/Q^2$. The data of adjacent bins in each kinematics typically have a 20-30% overlap and are thus correlated, while the lowest and the highest bins of each kinematics have larger overlaps with their adjacent bins. Figure 22 illustrates that all asymmetry data are consistent with the three resonance models and with the DIS estimation. No significant resonance structure is observed in the W-dependence of the asymmetries.

The agreement with DIS-based calculations indicates that quark-hadron duality [36] holds for PVES asymmetries on the deuteron at the $10-15\%$ level throughout the resonance region, for Q^2 values just below 1 (GeV/c)^2. These

Kinematics								
	DIS#1	Left DIS#2	Right DIS#2	RES I	RES II	RES III	RES IV	RES V
E_b (GeV)	6.067	6.067		4.867	4.867	4.867	6.067	6.067
θ_0	12.9°	20.0°		12.9°	12.9°	12.9°	15.0°	14.0°
E'_0 (GeV)	3.66	2.63		4.00	3.66	3.10	3.66	3.66
$\langle Q^2 \rangle_{\rm data}$ [(GeV/c)^2]	1.085	1.901		0.950	0.831	0.757	1.472	1.278
$\langle x \rangle_{\rm data}$	0.241	0.295		0.571	0.335	0.228	0.326	0.283
$\langle W \rangle_{\rm data}$ (GeV)	2.073	2.330		1.263	1.591	1.857	1.981	2.030
Y_3	0.434	0.661		0.340	0.353	0.411	0.467	0.451
R_V	0.808	0.876		–	–	–	–	–
$Y_3 R_V$	0.351	0.579		–	–	–	–	–
$A^{\rm bc,raw}$ (ppm)	-78.45	-140.30	-139.84	-55.11	-63.75	-54.38	-104.04	-67.87
(stat.)	± 2.68	± 10.43	± 6.58	± 6.77	± 5.91	± 4.47	± 15.26	± 21.25
(syst.)	± 0.07	± 0.16	± 0.46	± 0.10	± 0.15	± 0.24	± 0.26	± 0.72
Corrections with systematic uncertainties								
P_b	88.18%	89.29%	88.73%	90.40%	90.40%	90.40%	89.65%	89.65%
ΔP_b	$\pm 1.76\%$	$\pm 1.19\%$	$\pm 1.50\%$	$\pm 1.54\%$	$\pm 1.54\%$	$\pm 1.54\%$	$\pm 1.24\%$	$\pm 1.24\%$
$1 + f_{\rm depol}$	1.0010	1.0021		1.0005	1.0003	1.0009	1.0006	1.0008
(syst.)	$< 10^{-4}$	$< 10^{-4}$		$< 10^{-4}$	$< 10^{-4}$	$< 10^{-4}$	$< 10^{-4}$	
$1 + f_{\rm Al}$	0.9999	0.9999	0.9999	0.9997	0.9998	0.9999	0.9998	0.9999
(syst.)	± 0.0024	± 0.0024	± 0.0024	± 0.0042	± 0.0042	± 0.0042	± 0.0042	± 0.0042
$1 + f_{\rm dt}$	1.0147	1.0049	1.0093	1.0148	1.0247	1.0209	1.0076	1.0095
(syst.)	± 0.0009	± 0.0004	± 0.0013	± 0.0006	± 0.0023	± 0.0041	± 0.0004	0.0007
$1 + f_{\rm rc}$	1.015	1.019		1.1095	1.0205	1.0005	1.0170	1.0134
(syst.)	± 0.020	± 0.004		± 0.0352	± 0.0207	± 0.0076	± 0.0112	0.0110
$1 + f_{\gamma\gamma\rm box}$	0.998	0.997	–	–	–	–	–	–
$1 + \bar{f}_{\gamma\gamma,\gamma Z\rm boxes}$	–	–	1.005	1.005	1.005	1.005	1.005	1.005
(syst.)	± 0.002	± 0.003	± 0.005	± 0.005	± 0.005	± 0.005	± 0.005	± 0.005
Systematic uncertainties $\Delta A^{\rm phys}/A^{\rm phys}$ with no correction								
charged pion	$\pm 9 \times 10^{-5}$	$\pm 6 \times 10^{-5}$	$\pm 3 \times 10^{-5}$	$\pm 1.8 \times 10^{-4}$	$\pm 4.6 \times 10^{-4}$	$\pm 1.9 \times 10^{-4}$	$\pm 3 \times 10^{-5}$	$\pm 1.0 \times 10^{-4}$
pair production	± 0.0004	± 0.004	± 0.002	± 0.003	± 0.003	± 0.003	± 0.003	± 0.003
beam A_n	± 0.025	± 0.025	± 0.025	± 0.025	± 0.025	± 0.025	± 0.025	± 0.025
Q^2	± 0.0085	± 0.0064	± 0.0065	± 0.0081	± 0.0073	± 0.008	± 0.035	± 0.037
rescattering	$\ll 0.002$	$\ll 0.002$	$\ll 0.002$	$\ll 0.002$	$\ll 0.002$	$\ll 0.002$	$\ll 0.002$	$\ll 0.002$
target impurity	± 0.0006	± 0.0006	± 0.0006	± 0.0006	± 0.0006	± 0.0006	± 0.0006	± 0.0006
Asymmetry Results								
$A^{\rm phys}$ (ppm)	-91.10	-160.80		-68.62	-73.75	-61.49	-118.97	-77.50
(stat.)	± 3.11	± 6.39		± 8.43	± 6.84	± 5.05	± 17.45	± 24.27
(syst.)	± 2.97	± 3.12		± 3.26	± 2.78	± 2.06	± 5.54	± 3.84
(total)	± 4.30	± 7.12		± 9.04	± 7.38	± 5.46	± 18.31	± 24.57

Table 19: Asymmetry results on $\vec{e}-^2$H parity-violating scattering from the PVDIS experiment at JLab. The kinematics shown include the beam energy E_b, central angle and momentum settings of the spectrometer θ_0, E'_0, the actual kinematics averaged from the data (cross-section-weighted) $\langle Q^2 \rangle$ and $\langle x \rangle$, the kinematics factor Y_3 [calculated using $\langle Q^2 \rangle$, $\langle x \rangle$, E_b and Eq. (2)], the PDF valence quark distribution function ratio R_V calculated from MSTW2008 [52] Leading-Order parameterization and Eq. 31, and the product $Y_3 R_V$ that provides the lever arm for isolating the C_{2q} contribution to the asymmetry. The electron asymmetries obtained from the narrow trigger of the DAQ with beam dithering corrections, $A^{\rm bc,raw}$, were corrected for the effects from the beam polarization P_b and many systematic effects including: the beam depolarization effect $\bar{f}_{\rm depol}$, the target aluminum endcap $\bar{f}_{\rm Al}$, the DAQ deadtime $\bar{f}_{\rm dt}$ [54], the radiative correction $\bar{f}_{\rm rc}$ that includes effects from energy losses of incoming and scattered electrons as well as the spectrometer acceptance and detector efficiencies, and the box-diagram correction $\bar{f}_{\gamma\gamma\rm box}$ (for DIS) and $\bar{f}_{\gamma\gamma,\gamma Z\rm boxes}$ (for resonances). Systematic effects that do not require a correction to the asymmetry include: the charged pion and the pair production background , the beam normal asymmetry, the uncertainty in the determination of Q^2, the re-scattering background, and the target impurity. Final results on the physics asymmetries $A^{\rm phys}$ are shown with their statistical, systematic, and total uncertainties.

Group	1	2	3	4	5	6
RES I						
$\langle Q^2\rangle_{\rm data}[({\rm GeV/c})^2]$	0.992	0.966	0.948	0.940	0.931	0.940
$\langle W\rangle_{\rm data}({\rm GeV})$	1.119	1.175	1.245	1.305	1.350	1.364
$A_{\rm dit}^{\rm bc,raw}({\rm ppm})$	-30.84	-57.65	-54.01	-46.12	-60.24	-95.49
(stat.)	18.31	14.34	11.51	11.33	14.41	23.85
$1+f_{\rm dt}$	1.0077	1.0089	1.0105	1.0106	1.0088	1.0069
(syst.)	0.0004	0.0009	0.0004	0.0010	0.0008	0.0009
$1+f_{rc}$	1.359	1.150	1.045	1.024	1.011	1.010
(syst.)	0.155	0.031	0.014	0.005	0.004	0.004
$A^{\rm phys}$ (ppm)	-46.95	-74.35	-63.37	-53.05	-68.26	-107.89
(stat.)	±27.87	±18.49	±13.50	±13.03	±16.33	±26.95
(syst.)	±7.42	±3.36	±2.26	±1.77	±2.26	±3.58
(total)	±28.84	±18.80	±13.69	±13.15	±16.48	±27.18
RES II						
$\langle Q^2\rangle_{\rm data}[({\rm GeV/c})^2]$	0.856	0.849	0.834	0.820	0.808	0.819
$\langle W\rangle_{\rm data}({\rm GeV})$	1.503	1.533	1.583	1.629	1.662	1.672
$A_{\rm dit}^{\rm bc,raw}({\rm ppm})$	-60.67	-55.15	-77.16	-65.46	-65.92	-61.73
(stat.)	13.24	11.18	10.55	10.57	12.95	20.71
$1+f_{\rm dt}$	1.0134	1.0152	1.0160	1.0158	1.0135	1.0107
(syst.)	0.0008	0.0017	0.0006	0.0014	0.0012	0.0015
$1+f_{rc}$	1.032	1.017	1.012	1.000	0.995	0.995
(syst.)	0.006	0.003	0.002	<0.001	0.001	0.001
$A^{\rm phys}$ (ppm)	-70.56	-63.31	-88.21	-73.94	-73.91	-69.02
(stat.)	±15.40	±12.83	±12.06	±11.94	±14.52	±23.16
(syst.)	±2.35	±2.09	±2.89	±2.42	±2.42	±2.26
(total)	±15.58	±13.00	±12.40	±12.18	±14.72	±23.27
RES IV						
$\langle Q^2\rangle_{\rm data}[({\rm GeV/c})^2]$	1.531	1.533	1.473	1.442	1.427	1.378
$\langle W\rangle_{\rm data}({\rm GeV})$	1.901	1.922	1.978	2.020	2.049	2.071
$A_{\rm dit}^{\rm bc,raw}({\rm ppm})$	-103.29	-91.13	-82.82	-117.19	-142.95	87.30
(stat.)	32.87	32.21	27.24	27.00	37.52	96.85
$1+f_{\rm dt}$	1.0057	1.0057	1.0061	1.0061	1.0055	1.0049
(syst.)	0.0003	0.0004	0.0003	0.0004	0.0004	0.0003
$1+f_{rc}$	1.013	1.013	1.020	1.027	1.031	1.032
(syst.)	0.003	0.003	0.004	0.005	0.006	0.006
$A^{\rm phys}$ (ppm)	-118.02	-104.13	-95.32	-135.81	-166.21	101.54
(stat.)	±37.56	±36.80	±31.35	±31.29	±43.62	±112.65
(syst.)	±5.43	±4.79	±4.39	±6.28	±7.70	±4.71
(total)	±37.95	±37.11	±31.66	±31.91	±44.30	±112.75

Table 20: From left HRS group triggers: $\langle W\rangle$ and $\langle Q^2\rangle$ from data (cross-section weighted), beam-(dithering-)corrected raw asymmetries from narrow triggers, and group-dependent corrections. Corrections and uncertainties that do not depend on groups are the same as in Table 19 and are not shown here. After all corrections are applied, the final asymmetries are shown in the last row for each setting. We did not perform a group analysis for setting RES V.

Group	1	2	3	4	5	6	7	8
				RES III				
$\langle Q^2\rangle_{\rm data}[({\rm GeV/c})^2]$	0.731	0.719	0.730	0.744	0.761	0.777	0.796	0.799
$\langle W\rangle_{\rm data}({\rm GeV})$	1.928	1.923	1.905	1.880	1.851	1.820	1.790	1.771
$A_{\rm dit}^{\rm bc,raw}({\rm ppm})$	-58.62	-38.74	-56.02	-56.74	-56.67	-57.15	-52.57	-35.99
(stat.)	26.82	13.05	9.95	9.57	9.58	9.97	11.13	24.24
$1+f_{\rm dt}$	1.0127	1.0148	1.0169	1.0174	1.0173	1.0170	1.0161	1.0127
(syst.)	0.0011	0.0010	0.0011	0.0010	0.0010	0.0010	0.0011	0.0012
$1+f_{rc}$	1.022	1.021	1.024	1.026	1.025	1.024	1.020	1.010
(syst.)	0.004	0.004	0.005	0.005	0.005	0.005	0.004	0.002
$A^{\rm phys}$ (ppm)	-67.50	-44.66	-64.90	-65.90	-65.75	-66.22	-60.62	-40.96
(stat.)	±30.88	±15.05	±11.53	±11.12	±11.12	±11.55	±12.83	±27.59
(syst.)	±2.25	±1.49	±2.17	±2.21	±2.20	±2.21	±2.02	±1.36
(total)	±30.97	±15.12	±11.73	±11.33	±11.33	±11.76	±12.99	±27.62

Table 21: From right HRS group triggers: $\langle W\rangle$ and $\langle Q^2\rangle$ from data (cross-section-weighted), beam-(dithering-)corrected raw asymmetries from narrow triggers, and group-dependent corrections. Corrections and uncertainties that do not depend on groups are the same as in Table 19 and are not shown here. After all corrections are applied, the final asymmetries are shown in the last row for each setting. We did not perform a group analysis for setting RES V.

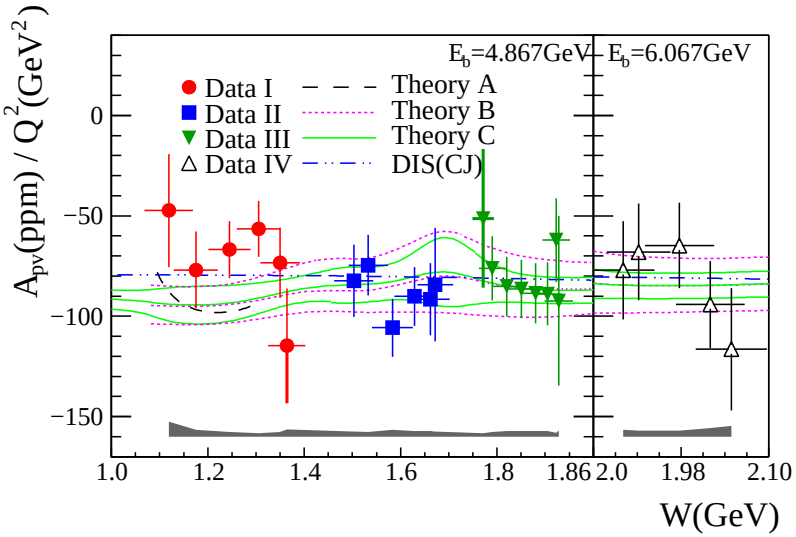

Figure 22: (*Color online*) From Ref. [49]: W-dependence of the parity-violating asymmetries in $\vec{e}-^2$H scattering in the nucleon resonance region. The physics asymmetry results $A_{PV}^{\rm phys}$ for the four kinematics RES I, II, III and IV (solid circles, solid squares, solid triangles, and open triangles, respectively), in parts per million (ppm), are scaled by $1/Q^2$ and compared with calculations from Ref. [84] (Theory A, dashed), Ref. [85] (Theory B, dotted), Ref. [87] (Theory C, solid) and the DIS estimation (dash-double-dotted) using Eq. (32) with the extrapolated CJ PDF [88]. The vertical error bars for the data are statistical uncertainties, while the horizontal error bars indicate the root-mean-square values of the W coverage of each bin. The experimental systematic uncertainties are shown as the shaded bands at the bottom. For each of the four kinematics, calculations were performed at the fixed E_b and Q^2 values of each of the RES I, II, III and IV settings and with a variation in W to match the coverage of the data. Theories B and C each have three curves showing the central values and the upper and the lower bounds of the calculation. Uncertainties of the DIS calculation were below 1 ppm and are not visible.

results are comparable to the unpolarized electromagnetic structure functions data which verified duality at the $5-10\%$ level for the proton and 15-20% for the neutron at similar Q^2 values, although the unpolarized measurements provided better resolution in W and covered a broader kinematic range [40, 41, 45].

4.4. Extraction of electron-quark effective coupling C_{2q} from DIS asymmetries

4.4.1. Calculation of PVDIS asymmetry sensitivity to C_{2q}

In order to extract the electron-quark VA couplings C_{2q}, one must first study the sensitivity of the measured PVDIS asymmetry to C_{2q}. Equation 2 was used for this purpose. In this section, inputs to Eq. 2 will be explained in detail, including all physical constants and couplings and the structure function evaluation. Uncertainties due to higher twist effects will be discussed at the end.

Electroweak radiative corrections were applied to all couplings used in the calculation of the asymmetry. The electromagnetic fine structure constant α was evolved to the measured Q^2-values from $\alpha_{EM}|_{Q^2=0} = 1/137.036$ [51]. The evaluation takes into account purely electromagnetic vacuum polarization. The Fermi constant is $G_F = 1.1663787(6)\times 10^{-5}$ GeV^{-2} [51]. The $C_{1q,2q}$ were evaluated using Table 7 and Eq. (114-115) of Ref. [89] at our measured Q^2-values in the modified minimal subtraction ($\overline{\rm MS}$) scheme using a fixed Higgs mass $M_H = 125.5$ GeV:

$$
\begin{aligned}
C_{1u}^{\rm SM} &= -0.1887 - 0.0011 \times \frac{2}{3}\ln(\langle Q^2\rangle/0.14{\rm GeV}^2) && (85)\\
C_{1d}^{\rm SM} &= 0.3419 - 0.0011 \times \frac{-1}{3}\ln(\langle Q^2\rangle/0.14{\rm GeV}^2) && (86)\\
C_{2u}^{\rm SM} &= -0.0351 - 0.0009\ln(\langle Q^2\rangle/0.078\ {\rm GeV}^2) && (87)\\
C_{2d}^{\rm SM} &= 0.0248 + 0.0007\ln(\langle Q^2\rangle/0.021\ {\rm GeV}^2) && (88)
\end{aligned}
$$

and it is expected that the uncertainty is negligible. Equations (85-88) include the "charge radius effect" and an estimate of the interference between γ-exchange and the γZ box, but not the effect from the $\gamma\gamma$ box. The effect from the $\gamma\gamma$ box was applied as a correction to the measured asymmetry as described in previous sections.

To express the measured asymmetries in terms of $2C_{1u} - C_{1d}$ and $2C_{2u} - C_{2d}$, we calculated all $F_{1,3}^{\gamma,\gamma Z}$ structure functions in Eqs. (2, 8, 9) and the resulting $a_{1,3}$ contribution to the asymmetry, see Table 22. Here the approximation $Y_1 = 1$ was used, which is valid if $R^\gamma = R^{\gamma Z}$. Also shown in Table 22 are values of $2C_{1u} - C_{1d}$ and $2C_{2u} - C_{2d}$ evaluated at the Q^2-values of the measurement. Three different parton distribution functions (PDFs) were used: the CTEQ/JLab ("CJ") fit [88] which provides structure functions at the next-to-leading order (NLO), the CT10 [90] (NLO only), and the leading-order (LO) MSTW2008 [52] fits. The CT10 and the MSTW2008 fits provide only PDF values but not the structure functions. For these two fits the quark-parton model (QPM) [Eqs. (10-12)] was used to calculate structure functions from PDFs. The paramaterization most suitable for our kinematics is the CJ fit, and it provides three different sets: the medium (mid), minimum, and maximum. However the CJ fit is not applicable for Q^2-values below 1.7 (GeV/c)^2. From the $Q^2 = 1.901$ (GeV/c)^2 comparison we found that the result of the LO MSTW2008 fit is closest to CJ, therefore it was used to interpret the $Q^2 = 1.085$ (GeV/c)^2 result. Results in Table 22 were also used for uncertainty estimation: the variation between various fits (three fits for $Q^2 = 1.901$ (GeV/c)^2 and two fits for $Q^2 = 1.085$ (GeV/c)^2) are at the level of relative 0.5% for the a_1 term and relative 5% for the a_3 term of the asymmetry.

As can be seen from Eq. (27, 28), the $a_{1,3}$ terms of the asymmetry are proportional to the $C_{1,2}$ couplings, respectively. This proportionality, i.e. the coefficient for $2C_{1u} - C_{1d}$ or $2C_{2u} - C_{2d}$ in the asymmetry, describes quantitatively the sensitivity to these couplings. To interpret the asymmetry results for both Q^2 values consistently, we used the MSTW2008 LO values in Table 22 as the nominal values and found for DIS setting #1, $A_{\rm SM} = -87.7 \pm 0.7$ ppm where the uncertainty is dominated by that from the PDFs. The sensitivity to the effective couplings is

$$
\begin{aligned}
A_{\rm SM} &= (115.63\ {\rm ppm})(2C_{1u} - C_{1d}) + (40.26\ {\rm ppm})(2C_{2u} - C_{2d}) && (89)\\
&= (1.156\times 10^{-4})\left[(2C_{1u} - C_{1d}) + 0.348(2C_{2u} - C_{2d})\right] && (90)
\end{aligned}
$$

For DIS setting #2, $A_{\rm SM} = (-158.9 \pm 1.0)$ ppm and

$$
\begin{aligned}
A_{\rm SM} &= (202.22\ {\rm ppm})(2C_{1u} - C_{1d}) + (120.08\ {\rm ppm})(2C_{2u} - C_{2d}) && (91)\\
&= (2.022\times 10^{-4})\left[(2C_{1u} - C_{1d}) + 0.594(2C_{2u} - C_{2d})\right]. && (92)
\end{aligned}
$$

The uncertainties in the sensitivity to $2C_{1u} - C_{1d}$ and $2C_{2u} - C_{2d}$ are 0.5% and 5%, respectively, as described in the previous paragraph. The resulting uncertainty is the $2C_{2u}-C_{2d}$ extraction due to the PDF fits is $\Delta(2C_{2u}-C_{2d})\pm 0.011$.

	$\langle Q^2\rangle = 1.085$, $\langle x\rangle = 0.241$	$\langle Q^2\rangle = 1.901$, $\langle x\rangle = 0.295$
Physical couplings used in the Calculation		
$\alpha_{EM}(Q^2)$	$1/134.45$	$1/134.20$
$C_{1u}^{\rm SM}$	-0.1902	-0.1906
$C_{1d}^{\rm SM}$	0.3427	0.3429
$2C_{1u}^{\rm SM} - C_{1d}^{\rm SM}$	-0.7231	-0.7241
$C_{2u}^{\rm SM}$	-0.0375	-0.0380
$C_{2d}^{\rm SM}$	0.0276	0.0280
$2C_{2u}^{\rm SM} - C_{2d}^{\rm SM}$	-0.1025	-0.1039
a_1, a_3 terms in $A_{\rm SM}$, in ppm		
CTEQ/JLab (CJ) full fit, mid	NA	$-147.37, -12.12$
min	NA	$-147.41, -12.99$
max	NA	$-147.40, -13.07$
"PDF+QPM" MSTW2008 LO	$-83.61, -4.13$	$-146.43, -12.48$
"PDF+QPM" CT10 (NLO)	$-84.06, -4.35$	$-146.64, -12.89$
coefficients for $2C_{1u} - C_{1d}$, $2C_{2u} - C_{2d}$ in $A_{\rm SM}$, in ppm		
CTEQ/JLab (CJ) full fit, mid	NA	$203.52, 116.68$
min	NA	$203.58, 125.01$
max	NA	$203.56, 125.78$
"PDF+QPM" MSTW2008 LO	$115.63, 40.26$	$202.22, 120.08$
"PDF+QPM" CT10 (NLO)	$116.25, 42.41$	$202.51, 124.08$

Table 22: Comparison of Standard-Model (SM) prediction for the asymmetry, $A_{\rm SM}$, using different structure functions: LO MSTW2008 [52], (NLO) CT10 [90], and the CTEQ/JLab (CJ) [88] fits. The CJ fits include 3 sets – middle, minimal, and maximal – to provide the nominal value of the PDF and the uncertainties. Values for $\alpha_{EM}(Q^2)$ were calculated using $\alpha_{EM}(Q^2 = 0) = 1/137.036$. The weak couplings at the measured Q^2-values, $C_{1,2}^{\rm SM}(Q^2)$, were based on Table 7 and Eq. (114-115) of Ref. [89].

The above calculation used the approximation that $Y_1 = 1$ which is valid if $R^\gamma = R^{\gamma Z}$. The effect of possible differences between $R^{\gamma Z}$ and R^γ was studied in Ref. [91]: to account for a shift of 1 ppm in the asymmetry, 7.7% and 4.5% differences between $R^{\gamma Z}$ and R^γ are needed, for DIS settings #1 and #2, respectively. Such large differences were considered highly unlikely and the uncertainty in the asymmetry due to the possible difference between $R^{\gamma Z}$ and R^γ was considered to be negligible compared to the statistical uncertainties of the measurement.

The higher-twist (HT) effects refer to the interaction between quarks inside the nucleon at low Q^2, where renormalization of the QCD coupling breaks down. At a relatively low Q^2, but not low enough for the effective QCD coupling to diverge, the HT effects introduce a $1/Q^2$-dependence to the structure functions in addition to the $\ln Q^2$ perturbative QCD evolution. The HT effects modify the PVDIS asymmetry through a change in the absorption cross-section ratio R^γ in Eqs. (5,6), or through changes in the structure function ratios a_1 and a_3 of Eq. (9). The effect on R^γ was estimated in Ref. [92] and was found to be negligible. Studies of the HT effects on the PVDIS asymmetry through changes in the structure functions dates back to the SLAC E122 experiment [93, 94], where it was argued that the HT effects on the a_1 term of the asymmetry are very small. The most recent discussions on HT effects of the PVDIS asymmetry, represented by work in Refs. [95, 96, 97], indicated that the HT contribution to the a_1 term is at or below the order of $0.5\%/Q^2$ for the x range of this experiment, where Q^2 is in units of (GeV/c)^2.

There is no theoretical estimation of the HT effects on the a_3 term of the asymmetry. However, this term is bounded by data on the neutrino structure function H_3^ν [92], which has the same quark content as $F_3^{\gamma Z}$. If applying the observed H_3^ν higher-twist Q^2-dependence to $F_3^{\gamma Z}$ alone, one expects the asymmetry to shift by $+0.7$ ppm and $+1.2$ ppm for the lower- and the higher-Q^2 results. We used these values as the uncertainty in the a_3 term due to HT effects.

Overall, a combination of theoretical and experimental bounds on the HT effects indicate that they do not exceed 1% of our measured asymmetry. The uncertainties in the a_1 and the a_3 terms due to HT were evaluated separately, and the corresponding uncertainty in $2C_{2u} - C_{2d}$ is 0.012, and is quite small compared to the experimental uncertainties.

4.4.2. Global fit to effective couplings C_{1q} and C_{2q}

Including the two DIS points obtained by our experiment, there is enough data to perform a simultaneous fit to the three linear combinations of effective couplings, $C_{1n} \equiv C_{1u} + 2\,C_{1d}$, $2\,C_{1u} - C_{1d}$, and $2\,C_{2u} - C_{2d}$. To do this, we used the constraint extracted from atomic parity violation in Cs [32] as quoted in Ref. [89],

$$188\,C_{1u} + 211\,C_{1d} = 36.35 \pm 0.21\,, \tag{93}$$

where we relied on the most recent atomic structure calculation in Ref. [35]. We also employed the latest C_{1q} result from Ref. [31]:

$$2\,C_{1u} + C_{1d} - 0.0004 = -0.032 \pm 0.006\,, \tag{94}$$

where the small adjustment on the left-hand side is from the electron charge radius [89]. Finally, we included the 11 data points of the SLAC–E122 experiment [9] listed in Table I. For these, we employed Eq. (29) with $\alpha = \alpha(Q^2)$ and $R_C = 0$, while the values of R_S and R_V are shown in Table 1. To account for the different Q^2 of these measurements, we adjusted the effective couplings using Eq. (85-88). Note that these corrections were applied to our DIS points as well, see Table 22.

There are various E122 point-to-point errors which we added in quadrature (following the original publication [9]), and then we added the result again quadratically to the statistical errors (rather than linearly as in Ref. [9]). In addition, a component of the polarization uncertainty was common to all data points. This resulted in a 5% correlated uncertainty in the scale of the asymmetries. We constructed the corresponding covariance matrix and included it in our fits.

As for the two DIS points of the present experiment, we erred on the conservative side and approximated their systematic (see Table 19) and theory uncertainties as fully correlated. The latter are composed of PDF uncertainties of 0.76% and errors originating from higher twist (quark-quark correlation) effects. The higher twist uncertainties enter separately and uncorrelated for the a_1 and the a_3 terms. As explained in the previous section, the HT uncertainty on a_1 term was taken to be $0.5\%/Q^2$ with Q^2 in GeV, or 0.39 ppm averaged over DIS#1 and #2, and that for the a_3 term was estimated from H_3^ν data to be 0.7 ppm and 1.2 ppm, repectively, for DIS#1 and DIS#2.

We then obtain the best fit result and correlation matrix,

$$\begin{array}{rc|ccc} C_{1u} + 2\,C_{1d} = & 0.489 \pm 0.005 & 1.00 & -0.94 & 0.42 \\ 2\,C_{1u} - C_{1d} = & -0.708 \pm 0.016 & -0.94 & 1.00 & -0.45 \\ 2\,C_{2u} - C_{2d} = & -0.145 \pm 0.068 & 0.42 & -0.45 & 1.00 \end{array} \tag{95}$$

where the χ^2 per degree of freedom is 17.3/12, corresponding to a 14% probability. These results are shown in Fig. 23. Figure 23 shows our results have greatly improved the uncertainty on the effective coupling $C_{2u,2d}$ and are in good

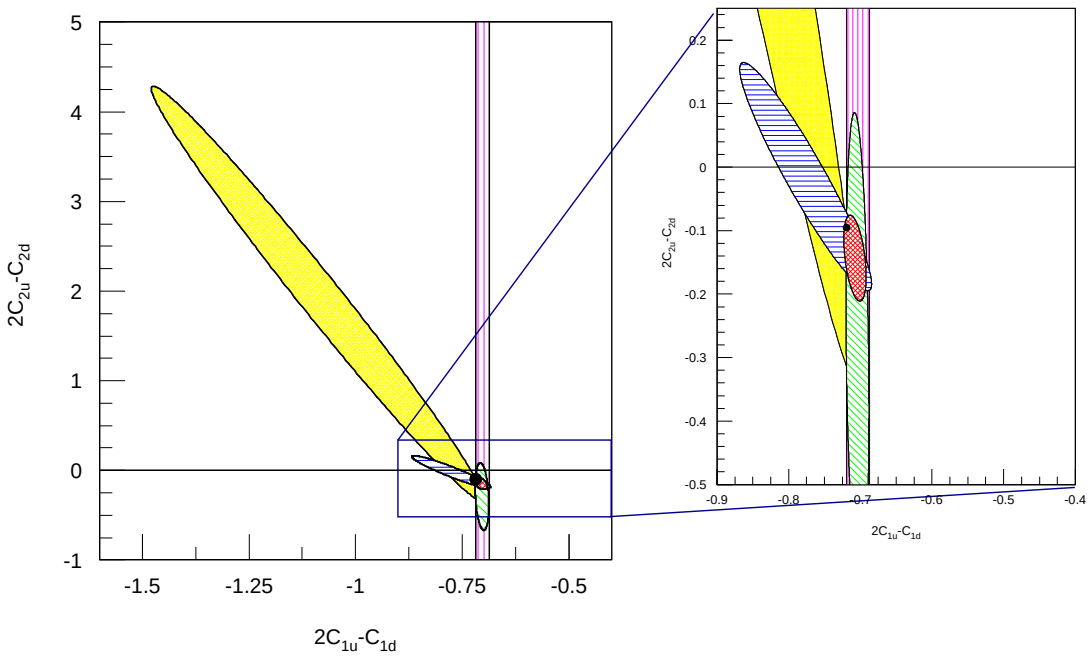

Figure 23: From Ref. [48]: results on $(2C_{1u}-C_{1d})|_{Q^2=0}$ and $(2C_{2u}-C_{2d})|_{Q^2=0}$ from the present experiment. The right panel shows an enlarged view with the vertical and the horizontal axis at the same scale. The new results (blue horizontal-line-hatched ellipse) are compared with SLAC E122 (yellow ellipse) [8, 9]. The latest data on C_{1q} [31] (from PVES and Atomic Cs [32, 33, 34, 35]) are shown as the magenta vertical-line-hatched band. The green slanted-line-hatched ellipse shows the combined result of SLAC E122 an d the latest C_{1q}, while the red line-cross-hatched ellipse shows the combined result of SLAC E122, the present experiment, and the latest C_{1q}. The Standard Model value $2C_{2u}-C_{2d}|_{Q^2=0} = -0.0950\pm0.0004$ is shown as the black dot, where the size of the dot is for visibility.

agreement with the Standard Model prediction. The result on C_{2q} alone is [48]

$$(2C_{2u} - C_{2d})\,|_{Q^2=0} = -0.145 \pm 0.066\ (\text{exp.}) \pm 0.011\ (\text{PDF}) \pm 0.012\ (\text{HT}) \quad (96)$$
$$= -0.145 \pm 0.068\ (\text{total}). \quad (97)$$

We note that this is the first time we observe the combination $(2C_{2u}-C_{2d})$ to be non-zero at the two standard deviation level. Because the C_{2q} is axial-vector in nature at the quark vertex, the result of Eq. (97) can be interpreted as the first direct evidence that quarks do exhibit a chirality preference when interacting with electrons through the neutral weak force [98].

4.4.3. Extracting mass limits

A comparison of the present result on $C_{1q,2q}$ with the Standard Model prediction can be used to set mass limits Λ below which new interactions are unlikely to occur. For the cases of electron and quark compositeness, we used the conventions from [99] and the procedure followed by the LEP 2 Collaborations, as described in Ref. [100].

The new physics effective Lagrangian for eq interactions is given by [99]

$$\mathcal{L}_{eq} = \frac{g^2}{\Lambda^2} \sum_{i,j=L,R} \eta_{ij}\, \bar{e}_i \gamma_\mu e_i\, \bar{q}_j \gamma^\mu q_j\ , \quad (98)$$

where Λ is defined [99] for strong coupling, *i.e.* relative to $g^2 = 4\pi$. For $\eta_{LL} = \eta_{RL} = -\eta_{LR} = -\eta_{RR} = 1$, and adding the SM contribution, one then obtains

$$\mathcal{L}_{eq} = \left[\frac{G_F}{\sqrt{2}} C_{2q}(\text{SM}) + \frac{g^2}{\Lambda^2}\right] \bar{e}\gamma_\mu e\, \bar{q}\gamma^\mu\gamma^5 q \quad (99)$$

$$\equiv \frac{C_{2q}(\mathrm{SM}) + \delta C_{2q}(\mathrm{new})}{2v^2}\,\bar{e}\gamma_\mu e\bar{q}\,\gamma^\mu\gamma^5 q \equiv \frac{C_{2q}}{2v^2}\,\bar{e}\gamma_\mu e\,\bar{q}\gamma^\mu\gamma^5 q\,,$$

where $\delta C_{2q}\mathrm{SM}$ is the deviation in C_{2q} from the SM value that may be related to beyond-the-SM physics, $v = (\sqrt{2}\,G_F)^{-1/2} = 246.22$ GeV is the Higgs vacuum expectation value which sets the electroweak scale.

If a measurement of the effective coupling, C_{2q}, or a fit to some data set, finds a central value $\bar{C}_{2q}$, then the best estimate of the new physics contribution would be given by

$$\frac{g^2}{\Lambda^2} = \frac{4\pi}{\Lambda^2} = \frac{\bar{C}_{2q} - C_{2q}(\mathrm{SM})}{2v^2}\,. \tag{100}$$

For the expected (projected) limits, one assume $\bar{C}_{2q} = C_{2q}(\mathrm{SM})$, in which case the 90% CL central range for C_{2q} is given by

$$-\,1.645\,\Delta C_{2q} < \delta C_{2q}(\mathrm{new}) < 1.645\,\Delta C_{2q}\,, \tag{101}$$

where ΔC_{2q} is the total (statistical + systematic + theoretical) 1 σ uncertainty from the extraction. The endpoints of this range can be interpreted as the 95% CL upper and lower limits of C_{2q}. However, it is conventional to consider the two possible sign choices of g^2/Λ^2 as two different "models", quoting two separate limits, $\Lambda_\pm$. Half of the probability distribution is then excluded by construction and one has to renormalize the remaining part. This amounts to the 95% CL:

$$|\delta C_{2q}(\mathrm{new})| < 1.96\,\Delta C_{2q}\,. \tag{102}$$

In the general case, $\bar{C}_{2q} \neq C_{2q}(\mathrm{SM})$, we find instead the 95% CL limits,

$$|C_{2q}|^\pm = \pm\left[\bar{C}_{2q} - C_{2q}(\mathrm{SM})\right] + \sqrt{2}\,\Delta C_{2q}\,\mathrm{erf}^{-1}\left[0.95 \mp 0.05\,\mathrm{erf}\left(\frac{\bar{C}_{2q} - C_{2q}(\mathrm{SM})}{\sqrt{2}\,\Delta C_{2q}}\right)\right]\,,$$

where

$$\mathrm{erf}(x) \equiv \frac{2}{\sqrt{\pi}}\int_0^x dt\,e^{-t^2} \tag{103}$$

is the Gauss error function and $\mathrm{erf}^{-1}(x)$ is its inverse.

A complication arises if a given observable or data set (such as the case at hand) is not sensitive to a specific flavor operator. In the case where u and d quarks are involved, we can rewrite,

$$\mathcal{L}_{eu} + \mathcal{L}_{ed} = \frac{\bar{e}\gamma_\mu e}{2v^2}\left[C_{2u}\,\bar{u}\gamma^\mu\gamma^5 u + C_{2d}\,\bar{d}\gamma^\mu\gamma^5 d\right]\,, \tag{104}$$

in terms of two rotated operators,

$$\begin{aligned}\mathcal{L}_{eu} + \mathcal{L}_{ed} \;=\; & \frac{\bar{e}\gamma_\mu e}{2v^2}\left(\cos\xi\,C_{2u} + \sin\xi\,C_{2d}\right)\left(\cos\xi\,\bar{u}\gamma^\mu\gamma^5 u + \sin\xi\,\bar{d}\gamma^\mu\gamma^5 d\right) \\ & + \frac{\bar{e}\gamma_\mu e}{2v^2}\left(-\sin\xi\,C_{2u} + \cos\xi\,C_{2d}\right)\left(-\sin\xi\,\bar{u}\gamma^\mu\gamma^5 u + \cos\xi\,\bar{d}\gamma^\mu\gamma^5 d\right)\,.\end{aligned} \tag{105}$$

For example, in the operator basis in which

$$\tan\xi = -\frac{1}{2}\,,$$

Eq. (105) becomes

$$\begin{aligned}\mathcal{L}_{eu} + \mathcal{L}_{ed} \;=\; & \frac{\bar{e}\gamma_\mu e}{2v^2}\frac{\left(2C_{2u} + C_{2d}\right)}{\sqrt{5}}\frac{\left(2\bar{u}\gamma^\mu\gamma^5 u + \bar{d}\gamma^\mu\gamma^5 d\right)}{\sqrt{5}} \\ & + \frac{\bar{e}\gamma_\mu e}{2v^2}\frac{\left(-C_{2u} + 2C_{2d}\right)}{\sqrt{5}}\frac{\left(-\bar{u}\gamma^\mu\gamma^5 u + 2\bar{d}\gamma^\mu\gamma^5 d\right)}{\sqrt{5}}.\end{aligned} \tag{106}$$

Experiments in PVDIS on isoscalar targets are only sensitive to the operator in the first line of Eq. (106). The same applies to the analogously defined rotation angle between the couplings C_{1u} and C_{1d}. In this case, the second line turns

out to be proportional to the weak charge of the neutron. In other words, the weak charge of the neutron (but not that of the proton) contains exactly orthogonal information to that provided by our experiment.

We determined the combination, $2\,\bar{C}_{2u} - \bar{C}_{2d}$, in the last line of the fit result in (95). Currently, the SM prediction is $[2\,C_{2u} - C_{2d}](\mathrm{SM}) = -0.0949$, and so the new physics scale corresponding to this operator is bounded (at the 95% CL) by,

$$\Lambda_+ \;>\; v\sqrt{\frac{\sqrt{5}\,8\pi}{|2C_{2u} - C_{2d}|^+}} = v\sqrt{\frac{\sqrt{5}\,8\pi}{0.104}} = 5.7\ \mathrm{TeV}, \tag{107}$$

$$\Lambda_- \;>\; v\sqrt{\frac{\sqrt{5}\,8\pi}{|2C_{2u} - C_{2d}|^-}} = v\sqrt{\frac{\sqrt{5}\,8\pi}{0.170}} = 4.5\ \mathrm{TeV}. \tag{108}$$

Results on the new mass limits are shown in Fig. 24. The improvement on the C_{2q} mass limit is approximately a factor of $\sqrt{5}$. We note that while collider experiments have set higher limits on new compositeness that are vector-electron and axial-vector-quark in nature, their observables are sensitive to a combination of different chiral structures, and such limits can only be derived by assuming all other chiral terms are zero. Such assumption is not necessary for the present experiment since we measured C_{2q} directly. Equations (107-108) provide model-independent mass limits on the electron-quark VA contact interactions and should be satisfied by any model of new physics.

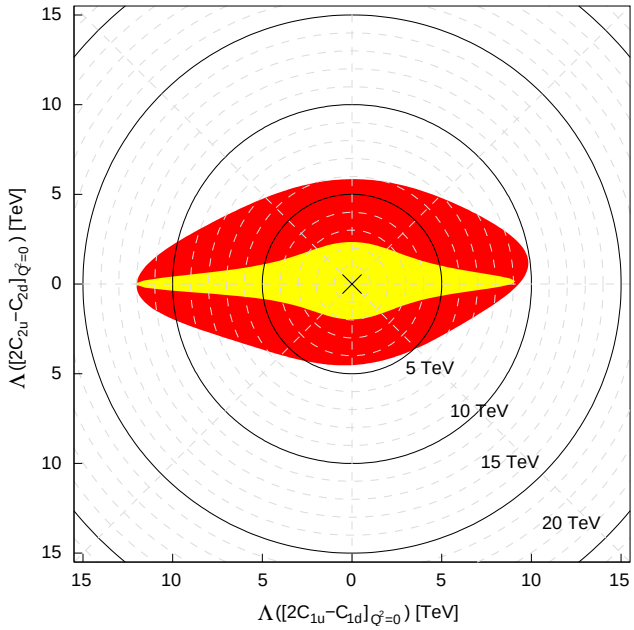

Figure 24: From Ref. [48]: Mass exclusion limits on the electron and quark compositeness and contact interactions obtained from the zero-Q^2 values of $2C_{1u} - C_{1d}$ and $2C_{2u} - C_{2d}$ at the 95% confidence level. The yellow contour shows the limit obtained from SLAC E122 asymmetry results [8, 9] combined with the best C_{1q} values [31]. The red contour shows the limit with our new results added.

5. Summary

In this paper we document the PVDIS experiment taken at Jefferson Lab using the 6 GeV longitudinally-polarized electron beam. We archive the experimental setup, the data analysis procedure, all corrections applied to the asymmetry, and all asymmetry results. Asymmetry results from DIS settings (Table 19) were used to extract the electron-quark effective couplings $C_{1q,2q}$ and the associate mass limits on new contact interactions. These DIS results have been published in Ref.[48]. Our results on C_{2q} improved over existing data by a factor of five and agreed well with the Standard Model prediction. They also showed for the first time that $2C_{2u} - C_{2d}$ is non-zero at the two standard-deviation level, indicating that the parity-violating asymmetry measured in electron deep inelastic scattering does

receive a contribution from the quarks' chiral preference in neutral weak intearction. Mass limits on new electron-quark VA contact interactions were extracted from our $2C_{2u} - C_{2d}$ result, and have improved over existing limits from PVES by a factor $\sqrt{5}$. Our mass limits are valid for all new electron-quark contact interactions that have the VA chiral structure, and are complementary to limits obtained from collider experiments.

Asymmetries in the nuclear resonance region are reported in Table 19 and their W-dependence in Tables 20 and 21. These results were published previously in Ref. [49]. Our resonance asymmetry results are in good agreement with theoretical predictions. They also agree well with DIS calculations extended to our kinematics, and do not show distinct resonance structure. This indicates that quark-hadron duality works for PVES asymmetries at the 10-15% level.

We also report on parity-violating asymmetries of inclusive pion production (Tables 9 and 10), pair production (Table 13), and beam-normal asymmetries (Table 16). The results are useful for background evaluation for other PVES experiments, including those planned for the JLab 12 GeV program.

Appendix A. Formalism for beam depolarization calculation

The beam depolarization was calculated using Eq.(9.11) of Ref. [79]:

$$D(\vec{p}_1, \vec{\zeta}_1) = \frac{k^2\left[\psi_1 - \zeta_{1z}^2(\psi_1 - \frac{2}{3}\psi_2)\right]}{(\epsilon_1^2 + \epsilon_2^2)\psi_1 - \frac{2}{3}\epsilon_1\epsilon_2\psi_2} \tag{A.1}$$

where $\epsilon_{1,2}$ are the energy of the electron before and after bremstralung in unit of the electron mass $m_e c^2$, k is the bremstralung photon energy in unit of $m_e c^2$, $\vec{\zeta}$ is the polarization vector of the electron with $\zeta_{1z} = 1$ for longitudinally polarized electrons, and $\psi_{1,2}$ are given in the "complete screening" limit by

$$\psi_1 = 4\ln(111Z^{-1/3}) + 2 - 4f(Z) = 4[\ln(183Z^{-1/3}) - f(Z)], \tag{A.2}$$

$$\psi_2 = 4[\ln(183Z^{-1/3}) - f(Z)] - \frac{2}{3}. \tag{A.3}$$

The function $f(Z)$ is

$$f(Z) = a^2\sum_{n=1}^{\infty}\frac{1}{n(n^2+a^2)}\,, \tag{A.4}$$

with $a = (Ze^2/\hbar/c)$.

The "complete screening" limit is defined as $\beta_i\xi/\delta \gg 1$ where $\beta_i = (Z^{1/3}/121)b_i$ with $b_1 = 6$, $b_2 = 1.2$ and $b_3 = 0.3$; $\xi \equiv 1/(1+u^2)$ with $u = p_1\theta_1$; and $\delta \equiv k/(2\epsilon_1\epsilon_2)$. Here $\vec{p}_1, \vec{p}_2$ are momentum of the electron before and after bremstralung in unit of $m_e c$, and θ_1, θ_2 are the angles between $\vec{p}_1, \vec{p}_2$ and the photon $\vec{k}$, respectively. Because for high energy electrons θ_1 is very small, $u \approx 0$ and $\xi \approx 1$. Putting all notations together, the complete screening limit is

$$\frac{\beta_i\xi}{\delta} = \frac{\frac{Z^{1/3}}{121}b_i}{(1+\epsilon_1^2\theta_1^2)\frac{k}{2\epsilon_1\epsilon_2}} \approx \frac{\frac{Z^{1/3}}{121}b_i}{\frac{k}{2\epsilon_1\epsilon_2} + \frac{1}{2}k\theta_1^2} \gg 1 \tag{A.5}$$

where the approximation is valid if $k \ll \epsilon_1$ (which implies $\epsilon_1 \approx \epsilon_2$ and $k \ll \epsilon_2$) and the complete screening condition is satisfied if $\epsilon_{1,2} \gg 1$. For the 6-GeV beam used in this experiment, $\epsilon_1 \approx 12000$ and $k \ll \epsilon_1$, therefore the complete screening limit can be used.

[1] T.D. Lee and C.-N. Yang, Phys. Rev. **104**, 254 (1956).

[2] C.S. Wu *et al.*, Phys. Rev. **105**, 1413 (1957).

[3] S. L. Glashow, Nucl. Phys. **22**, 579 (1961).

[4] S. Weinberg, Phys. Rev. Lett. **19**, 1264 (1967).

[5] A. Salam, Conf. Proc. C **680519**, 367 (1968).

[6] F. J. Hasert *et al.*, Phys. Lett. B **46**, 121 (1973).

[7] F. J. Hasert *et al.* [Gargamelle Neutrino Collaboration], Nucl. Phys. B **73**, 1 (1974).

[8] C. Y. Prescott *et al.*, Phys. Lett. B **77**, 347 (1978).

[9] C. Y. Prescott *et al.*, Phys. Lett. B **84**, 524 (1979).

[10] R. D. Mckeown, Phys. Lett. B **219**, 140 (1989).

[11] R. Hasty *et al.* [SAMPLE Collaboration], Science **290**, 2117 (2000).

[12] D. T. Spayde *et al.* [SAMPLE Collaboration], Phys. Lett. B **583**, 79 (2004).

[13] T. M. Ito *et al.* [SAMPLE Collaboration], Phys. Rev. Lett. **92**, 102003 (2004).

[14] E. J. Beise, M. L. Pitt and D. T. Spayde, Prog. Part. Nucl. Phys. **54**, 289 (2005).

[15] F. E. Maas *et al.* [A4 Collaboration], Phys. Rev. Lett. **93**, 022002 (2004).

[16] F. E. Maas *et al.*, Phys. Rev. Lett. **94**, 152001 (2005).

[17] S. Baunack *et al.*, Phys. Rev. Lett. **102**, 151803 (2009).

[18] K. A. Aniol *et al.* [HAPPEx Collaboration], Phys. Lett. B **509**, 211 (2001).

[19] K. A. Aniol *et al.* [HAPPEx Collaboration], Phys. Rev. C **69**, 065501 (2004).

[20] K. A. Aniol *et al.* [HAPPEx Collaboration], Phys. Rev. Lett. **96**, 022003 (2006).

[21] K. A. Aniol *et al.* [HAPPEx Collaboration], Phys. Lett. B **635**, 275 (2006).

[22] A. Acha *et al.* [HAPPEx Collaboration], Phys. Rev. Lett. **98**, 032301 (2007).

[23] Z. Ahmed *et al.* [HAPPEx Collaboration], Phys. Rev. Lett. **108**, 102001 (2012).

[24] D. H. Beck, Phys. Rev. D **39**, 3248 (1989).

[25] D. S. Armstrong *et al.* [G0 Collaboration], Phys. Rev. Lett. **95**, 092001 (2005).

[26] D. Androic *et al.* [G0 Collaboration], Phys. Rev. Lett. **104**, 012001 (2010).

[27] S. Abrahamyan *et al.*, Phys. Rev. Lett. **108**, 112502 (2012).

[28] C. J. Horowitz *et al.*, Phys. Rev. C **85**, 032501 (2012).

[29] P.L. Anthony *et al.*, [SLAC E158 Collaboration], Phys. Rev. Lett. **95**, 081601 (2005).

[30] A. Czarnecki and W.J. Marciano, Nature **435**, 437-438 (2005).

[31] D. Androic *et al.* [Qweak Collaboration], Phys. Rev. Lett. **111**, 141803 (2013).

[32] C.S. Wood *et al.*, Science **275**, 1759 (1997).

[33] S.C. Bennett and C.E. Wieman, Phys. Rev. Lett. **82**, 2484 (1999) [Erratum-ibid. **83**, 889 (1999)].

[34] J.S.M. Ginges and V.V. Flambaum, Phys. Rept. **397**, 63 (2004).

[35] V.A. Dzuba, J.C. Berengut, V.V. Flambaum and B. Roberts, Phys. Rev. Lett. **109**, 203003 (2012).

[36] E. D. Bloom and F. J. Gilman, Phys. Rev. Lett. **25**, 1140 (1970).

[37] I. Niculescu *et al.*, Phys. Rev. Lett. **85**, 1186 (2000).

[38] Y. Liang *et al.*, nucl-ex/0410027.

[39] A. Psaker, W. Melnitchouk, M. E. Christy, and C. Keppel, Phys. Rev. C **78**, 025206 (2008).

[40] S. P. Malace, Y. Kahn, W. Melnitchouk and C. E. Keppel, Phys. Rev. Lett. **104**, 102001 (2010).

[41] S. P. Malace *et al.*, Phys. Rev. C **80**, 035207 (2009).

[42] A. Airapetian *et al.* (HERMES Collaboration), Phys. Rev. Lett. **90**, 092002 (2003).

[43] P. E. Bosted *et al.*, Phys. Rev. C **75**, 035203 (2007).

[44] P. Solvignon *et al.*, Phys. Rev. Lett. **101**, 182502 (2008).

[45] S. P. Malace, W. Melnitchouk, and A. Psaker, Phys. Rev. C **83**, 035203 (2011).

[46] T. Navasardyan *et al.*, Phys. Rev. Lett. **98**, 022001 (2007).

[47] C. E. Carlson and N. C. Mukhopadhyay, Phys. Rev. D **47**, 1737 (1993).

[48] D. Wang *et al.* [PVDIS Collaboration], Nature **506**, no. 7486, 67 (2014).

[49] D. Wang *et al.* [Jefferson Lab Hall A Collaboration], Phys. Rev. Lett. **111**, 082501 (2013).

[50] R. N. Cahn and F. J. Gilman, Phys. Rev. D **17**, 1313 (1978).

[51] J. Beringer *et al.* (Particle Data Group), Phys. Rev. D**86**, 010001 (2012).

[52] A. D. Martin, W. J. Stirling, R. S. Thorne and G. Watt, Eur. Phys. J. C **63**, 189 (2009).

[53] J. Alcorn *et al.*, Nucl. Instrum. Meth. A **522**, 294 (2004).

[54] R. Subedi *et al.*, Nucl. Instrum. Meth. A **724**, 90 (2013).

[55] C. K. Sinclair *et al.* Phys. Rev. ST Accel. Beams 10, 023501 (2007); J. Hansknecht *et al.* Phys. Rev. ST Accel. Beams 13, 010101 (2010).

[56] K. D. Paschke, Eur. Phys. J. A **32**, 549 (2007).

[57] J. Grames *et al.*, Accelerator Conference, New York, New York (2011).

[58] W. Barry, Nucl. Instrum. Meth. A301 (1991) 407; T. Powers, L. Doolittle, R. Ursic, and J. Wagner, Proc. 7th Workshop on Beam Instrumentation, AIP Conf.Proc. **390**, Ed. A. Lumpkin and C.E. Eyberger (1997); JLAB-TN-96-021.

[59] J. S. Price *et al.*, In Protvino 1998, High energy spin physics 554-556

[60] J. S. Price *et al.*, In Urbana 1997, Polarized gas targets and polarized beams 446.

[61] J. S. Price *et al.*, prepared for Conference: C96-09-10, p.727 Proceedings.

[62] M. Steigerwald, http://www.jlab.org/accel/inj_group/mott/mott.pdf

[63] M. Baylac *et al.*, Phys. Lett. B **539**, 8 (2002).

[64] D. Neyret *et al.*, Nucl. Instrum. Meth. A **443**, 231 (2000).

[65] M. Friend *et al.*, Nucl. Instrum. Meth. A **676**, 96 (2012).

[66] J. P. Jorda *et al.*, Nucl. Instrum. Meth. A **412**, 1 (1998).

[67] N. Falletto *et al.* [HAPPEx Collaboration], Nucl. Instrum. Meth. A **459**, 412 (2001).

[68] N. Liyanage, Optics Calibration of the Hall A High Resolution Spectrometers using the C Optimizer, JLab-TN-02-012, 2002.

[69] P. E. Bosted and M. E. Christy, Phys. Rev. C **77**, 065206 (2008).

[70] J. J. Aubert *et al.* [European Muon Collaboration], Phys. Lett. B **123**, 275 (1983).

[71] P. R. Norton, Rept. Prog. Phys. **66**, 1253 (2003).

[72] I. Sick and D. Day, Phys. Lett. B **274**, 16 (1992).

[73] J. Gomez *et al.*, Phys. Rev. D **49**, 4348 (1994).

[74] S. Stein *et al.*, Phys. Rev. D **12**, 1884 (1975).

[75] S. Rock and P. E. Bosted, Phys. Lett. B **518**, 34 (2001).

[76] S. Abrahamyan *et al.* [HAPPEx and PREX Collaborations], Phys. Rev. Lett. **109**, 192501 (2012).

[77] A. Afanasev, priv. communication.

[78] M. Seely, *Gas Chromatograph Analysis for Deuterium Sample*, July 26, 2002.

[79] H. Olsen and L. C. Maximon, Phys. Rev. **114**, 887 (1959).

[80] L. W. Mo and Y. -S. Tsai, Rev. Mod. Phys. **41**, 205 (1969).

[81] R. Michaels, Formulas for Hall A Monte Carlo (2008), URL: http://hallaweb.jlab.org/parity/prex/hamc/hamc_formulas.pdf

[82] D. Abbott *et al.* [JLAB t20 Collaboration], Eur. Phys. J. A **7**, 421 (2000).

[83] S. J. Pollock, Phys. Rev. D **42**, 3010 (1990) [Erratum-ibid. D **43**, 2447 (1991)].

[84] K. Matsui, T. Sato and T. -S. H. Lee, Phys. Rev. C **72**, 025204 (2005).

[85] M. Gorchtein, C. J. Horowitz and M. J. Ramsey-Musolf, Phys. Rev. C **84**, 015502 (2011).

[86] M. Arneodo *et al.* [New Muon Collaboration], Phys. Lett. B **364**, 107 (1995).

[87] N. L. Hall *et al.*, Phys. Rev. D **88**, 013011 (2013).

[88] J. F. Owens, A. Accardi and W. Melnitchouk, Phys. Rev. D **87**, 094012 (2013).

[89] J. Erler and S. Su, Prog. Part. Nucl. Phys. **71**, 119 (2013).

[90] H. -L. Lai *et al.*, Phys. Rev. D **82**, 074024 (2010).

[91] T. Hobbs and W. Melnitchouk, Phys. Rev. D **77**, 114023 (2008).

[92] S. Alekhin, S. A. Kulagin and R. Petti, AIP Conf. Proc. **967**, 215 (2007).

[93] J. D. Bjorken, Phys. Rev. D **18**, 3239 (1978).

[94] L. Wolfenstein, Nucl. Phys. B **146**, 477 (1978).

[95] S. Mantry, M. J. Ramsey-Musolf and G. F. Sacco, Phys. Rev. C **82**, 065205 (2010).

[96] A. V. Belitsky, A. Manashov and A. Schafer, Phys. Rev. D **84**, 014010 (2011).

[97] C. -Y. Seng and M. J. Ramsey-Musolf, Phys. Rev. C **88**, no. 1, 015202 (2013).

[98] W. J. Marciano, Nature **506**, 43 (2014).

[99] E. Eichten, K. D. Lane and M. E. Peskin, Phys. Rev. Lett. **50**, 811 (1983).

[100] S. Schael *et al.* [ALEPH and DELPHI and L3 and OPAL and LEP Electroweak Collaborations], Phys. Rept. **532**, 119 (2013).